Master's Thesis

Evaluation of the T2K Beam and Secondary Beamline using the Muon Monitor (T2K実験におけるミューオンモニターを用いたビームと２次ビームラインの評価)

Ian Benjamin Heitkamp

Department of Physics

Graduate School of Science

Tohoku University

2024

Abstract

The T2K Experiment is a long baseline neutrino oscillation experiment in Japan. A beam consisting mostly of muon neutrinos or antineutrinos is created at the Japan Proton Accelerator Research Complex (J-PARC) in Tokai, Ibaraki and is detected by the Super-Kamiokande detector 295 km away, 2.5 degrees off of the beam axis. The current goal of the T2K experiment is to search for CP-violation in neutrino oscillations and make more precise measurements of oscillation parameters θ_{23}, Δm^2_{32}, and Δm^2_{31}

Since the expected neutrino energy distribution at the far detector depends on the angle relative to the beam axis, and in order to safely operate the beam continuously at high intensity, it is necessary to measure the flux in a spill by spill measurement. The muon monitor located 118 m downstream of the target indirectly measures the neutrino beam using the muons generated alongside the muon neutrinos from pion decay. The muon monitor consists of two main sets of sensors, a 7×7 silicon PIN photodiode array (SI) and a 7×7 ionization chamber array (IC).

It is important to understand the muon flux at the muon monitor in order to properly reconstruct the muon profile. It was found from detailed simulations that the muon flux generally follows a double gaussian shape rather than the expected single gaussian shape. This was checked using data from Run 13 (11/2023-7/2024), and the structure was successfully reconstructed in the case where the pion focusing horns are turned off.

The muon monitor is used during beam tuning in order to ensure that the proton beam is properly centered on the target. Proton beam position and angle scans are carried out to determine the center of the target. However, due to the many components in the secondary beamline, the alignment of these components may affect the muon monitor's measurement. Simulations using possible misalignments of the baffle (beam collimator) and the target in the secondary beamline were carried out in order to determine the effects of these misalignments. These are checked against the position scan data from Run 12 (4/2023) and Run 13 (11/2023).

As the beam intensity is increased at J-PARC in order to obtain higher statistics, the radiation damage sustained by the SI array will require increasingly frequent replacement of the SI sensors. As such, a more radiation tolerant sensor, the electron multiplier tube (EMT) is being installed. Currently a row of 7 EMTs are installed along the vertical center of the muon monitor behind the SI array. Since more EMTs are planned to be installed, several configurations were tested in fitting simulations using data from Run 13 to ascertain the best configuration for the 2D fitting of the muon profile.

Contents

List of Figures

List of Tables

Chapter 1

Introduction

1.1 Neutrinos and Neutrino Oscillation

Neutrinos are a fermion in the lepton sector that interacts only via the weak interaction and gravity. They were first proposed by Wolfgang Pauli in 1930 to explain the radioactive beta decay electron's continuous energy spectrum via a 3-body decay involving an invisible massless neutral particle, a "neutrino". Since weak interaction cross sections are heavily suppressed by the mass of the mediating Z and W bosons, the detection and confirmation of the existence of the neutrino was not done until the Cowan-Reines experiment in 1956 [3]. The subsequent discovery of the muon neutrino in 1962[4], and the tau neutrino in 2000 by the DONUT collaboration[5], confirmed the existence of the three flavors of neutrinos corresponding to the flavors of the charged leptons, the electron, muon, and tau particles.

The first indication of neutrino oscillation was the Homestake experiment [6] in 1968 which measured the solar electron neutrino flux, which found it to be much less than the predictions of the fusion processes in the sun. This remained a mystery until the confirmation of electron neutrino disappearance and muon neutrino appearance in the Super-Kamiokande experiment in 1998 [7].

The lepton sector's flavors are named based on the 3 charged leptons, the electron, the muon, and the tau particle. These leptons have a corresponding neutrino flavor eigenstate, ν_e, ν_μ, ν_τ. Neutrino flavor oscillation is possible since neutrinos interact via their weak flavor eigenstates, and propagate under their mass eigenstates, generally called simply ν_1, ν_2, and ν_3. Since the flavor eigenstates and mass eigenstates are not identical, the superposition of the neutrino's flavor eigenstate changes over time between interactions. The mixing of the flavor and mass eigenstates is described by the Pontecorvo–Maki–Nakagawa–Sakata matrix (PMNS matrix), which in the standard framework is a unitary matrix analogous to the CKM matrix for quark flavor mixing. This matrix relates the flavor eigenstates to the mass eigenstates. This can be written as shown below.

$$|\nu_\alpha\rangle = \sum_i U_{\alpha i} |\nu_i\rangle \qquad \left\{ \begin{array}{c} \alpha = e, \mu, \tau \\ i = 1, 2, 3 \end{array} \right\} \tag{1.1}$$

where $U_{\alpha i}$ is the element of the PMNS matrix U corresponding to flavor α and mass eigenstate i. In the event that the flavor eigenstates were equivalent to the mass eigenstates, this matrix would be perfectly diagonal. While ordinarily this matrix would have nine independent

parameters, in this case, the PMNS matrix can be parameterized using just four parameters. Thus the matrix U can be written as:

$$U = \begin{pmatrix} 1 & 0 & 0 \\ 0 & c_{23} & s_{23} \\ 0 & -s_{23} & c_{23} \end{pmatrix} \begin{pmatrix} c_{13} & 0 & e^{i\delta_{CP}} s_{13} \\ 0 & 1 & 0 \\ -e^{i\delta_{CP}} s_{13} & 0 & c_{13} \end{pmatrix} \begin{pmatrix} c_{12} & s_{12} & 0 \\ -s_{12} & c_{12} & 0 \\ 0 & 0 & 1 \end{pmatrix} \tag{1.2}$$

If this matrix is fully multiplied out, it becomes:

$$U = \begin{pmatrix} c_{12}c_{13} & s_{12}c_{13} & s_{13}e^{i\delta_{CP}} \\ -s_{12}c_{23} - c_{12}s_{23}s_{13}e^{i\delta_{CP}} & c_{12}c_{23} - s_{12}s_{23}s_{13}e^{i\delta_{CP}} & s_{23}c_{13} \\ s_{12}c_{23} - c_{12}s_{23}s_{13}e^{i\delta_{CP}} & -c_{12}c_{23} - s_{12}s_{23}s_{13}e^{i\delta_{CP}} & c_{23}c_{13} \end{pmatrix} \tag{1.3}$$

where s_{ij} and c_{ij} represent $\sin\theta_{ij}$ and $\cos\theta_{ij}$ respectively, where θ_{ij} represents the mixing angle of mass eigenstates ν_i and ν_j leaving us with three mixing angles, θ_{12}, θ_{13}, and θ_{23}. δ_{CP} represents a charge-parity violating phase representing the magnitude of CP-violation. In all, the PMNS matrix is described by these 4 parameters.

To find the probability that a neutrino oscillation has occurred over a given time, we need to consider the time evolution of the flavor state superposition. To simplify things for this example, a two neutrino system can be used, which can be parameterized by a single mixing angle θ. We can rewrite equation 2.1 as:

$$\begin{pmatrix} |\nu_\alpha\rangle \\ |\nu_\beta\rangle \end{pmatrix} = \begin{pmatrix} \cos\theta & \sin\theta \\ -\sin\theta & \cos\theta \end{pmatrix} \begin{pmatrix} |\nu_1\rangle \\ |\nu_2\rangle \end{pmatrix} \tag{1.4}$$

where flavors ν_α and ν_β are written as a superposition of mass eigenstates ν_1 and ν_2. If we use the Schrodinger equation for time evolution of the quantum state, we get:

$$i\frac{d}{dt}|\nu_i(t)\rangle = \hat{H}\,|\nu_i(0)\rangle \tag{1.5}$$

$$|\nu_i(t)\rangle = e^{iE_i t}\,|\nu_i(0)\rangle \tag{1.6}$$

For this equation, E_i describes the energy of the mass eigenstate. For simplicity, c=$\hbar$=1 is used. Using Equation 1.4 and 1.6, the time evolution of the different flavor eigenstates can be found to be

$$\begin{pmatrix} |\nu_\alpha\rangle \\ |\nu_\beta\rangle \end{pmatrix} = \begin{pmatrix} \cos\theta & \sin\theta \\ -\sin\theta & \cos\theta \end{pmatrix} \begin{pmatrix} e^{iE_1 t}\,|\nu_1\rangle \\ e^{iE_2 t}\,|\nu_2\rangle \end{pmatrix} \tag{1.7}$$

By multiplying this matrix out and finding the states $|\nu_1>$ and $|\nu_2>$ in terms of $|\nu_\alpha>$ and $|\nu_\beta>$, the superposition of flavor eigenstates can be found for a chosen initial flavor state, in this case we will consider ν_α

$$|\nu_\alpha(t)\rangle \;=\; (\cos^2\theta e^{-iE_1 t} + \sin^2\theta e^{-iE_2 t})\,|\nu_\alpha\rangle + \sin\theta\cos\theta(e^{-iE_2 t} - e^{-iE_1 t})\,|\nu_\beta\rangle \tag{1.8}$$

The probability of an oscillation to ν_β from a ν_α initial state is given by:

$$\begin{aligned} |\langle\nu_\beta|\nu_\alpha(t)\rangle|^2 &= \left|\sin\theta\cos\theta(e^{-iE_2t} - e^{-iE_1t})\right|^2 \\ &= \left|\frac{1}{2}\sin 2\theta(e^{-i(E_2-E_1)t} - 1)\right|^2 \\ &= \frac{1}{4}\sin^2(2\theta)\sin^2\left(\frac{E_2 - E_1}{2}t\right) \end{aligned} \tag{1.9}$$

Since E just corresponds to the energy of the given mass eigenstate, we can use the equation

$$E_i = \sqrt{p^2 + m_i^2} \tag{1.10}$$

which, since neutrino momentum is generally much larger than its rest mass energy, it can be expressed by the approximation

$$E_i \approx p + \frac{m_i^2}{2p} \tag{1.11}$$

So for the case $E_2 - E_1$, we get

$$\begin{aligned} E_2 - E_1 &= \sqrt{p^2 + m_2^2} - \sqrt{p^2 + m_1^2} \\ &\approx p + \frac{m_2^2}{2p} - p + \frac{m_1^2}{2p} \\ &\approx \frac{m_2^2 - m_1^2}{2E} = \frac{\Delta m_{21}^2}{2E} \end{aligned} \tag{1.12}$$

where E is the neutrino energy and Δm_{21}^2 is the difference in the squared masses $m_2^2 - m_1^2$. Plugging this back into the oscillation probability (eq. 1.9) and using the approximation of time t = length L in the ultra-relativistic limit

$$\begin{aligned} P(\nu_\alpha \to \nu_\beta) &\approx \frac{1}{4}\sin^2(2\theta)\sin^2\left(\frac{\Delta m_{21}^2}{4E}L\right) \\ &\approx \frac{1}{4}\sin^2(2\theta)\sin^2\left(\frac{1.27\Delta m_{21}^2[\text{eV}]}{E[\text{GeV}]}L[\text{km}]\right) \end{aligned} \tag{1.13}$$

where the second equation is converting to km, eV, GeV units from c=$\hbar$=1. In the case of three neutrino flavors, the whole PMNS matrix with all 3 mixing angles must be considered, rather than the single mixing angle θ from the two flavor case. Since the general process of finding the oscillation probability is the same, the matrix calculations will be skipped. The general form of the oscillation probability for the 3 state PMNS matrix U in natural units is:

$$P(\nu_\alpha \to \nu_\beta) = |\langle\nu_\beta|\nu_\alpha(t)\rangle|^2 = \left|\sum_j U_{\alpha j}^* U_{\beta j} e^{\left(-i\frac{m_j^2 L}{2E}\right)}\right|^2 \tag{1.14}$$

$$\begin{aligned} P(\nu_\alpha \to \nu_\beta) &= \delta_{\alpha\beta} - 4\sum_{i<j} Re(U_{\alpha i}U_{\beta i}^* U_{\alpha j}^* U_{\beta j})\sin^2\left(\frac{\Delta m_{ij}^2}{4E}L\right) \\ &\quad + 2\sum_{i<j} Im(U_{\alpha i}U_{\beta i}^* U_{\alpha j}^* U_{\beta j})\sin^2\left(\frac{\Delta m_{ij}^2}{2E}L\right) \end{aligned} \tag{1.15}$$

It is useful for experiments to find the oscillation peaks for a given $\frac{L}{E}$ where L is the baseline to the detector, while E is the neutrino energy, and these two parameters can be tuned to maximize the oscillation probability. The equation below is the oscillation maximums for the two flavor case derived in Eq. 1.13

$$\frac{1.27\Delta m^2[\text{eV}]L[\text{km}]}{E[\text{GeV}]} = \frac{(2n-1)\pi}{2} \tag{1.16}$$

An accelerator experiment, such as T2K, can position their detector to be near an oscillation maximum, greatly increasing the probability of seeing disappearance of one flavor in the neutrino flux, while seeing an appearance of another flavor.

Neutrinos can be detected when they interact with nuclei or electrons following either charged current interactions involving the $W^{\pm}$ boson or neutral current interactions involving the Z boson. These cross sections are heavily suppressed by the mediating boson's mass leading to neutrino interactions being very rare, and most are able to pass straight through the Earth without interacting.

The main methods of neutrino matter interactions are shown below:

$$\begin{aligned} &\nu_l + n \rightarrow l^- + p \\ &\nu_l + e^- \rightarrow \nu_l + e^- \\ &\overline{\nu}_l + p \rightarrow l^+ + n \end{aligned} \tag{1.17}$$

Where l represents the lepton flavor. As well as some more complicated methods of interaction caused by inelastic scattering within a nucleus. 1 & 3 of 1.17 are charged current (CC) interactions involving the charged W boson, while 2 is a neutral current interaction (NC) involving the Z boson.

1.1.1 Measurements of the Neutrino Oscillation Parameters

Since the discovery of neutrino oscillation, a wide variety of experiments have tasked themselves with finding the values of the observable oscillation parameters: the three mixing angles, δ_{CP}, and the mass differences between ν_1, ν_2, and ν_3. The best measurements of the neutrino oscillation parameters were taken to be those reported in Particle Data Group(PDG) 2024 release [8]. The three general experiment types used to measure neutrino oscillation parameters are reactor neutrino experiments which use nuclear reactor neutrinos to obtain measurements with a short baseline. Solar neutrinos have a wealth of data for the ν_e related oscillation parameters, and atmospheric neutrinos provide a variety of oscillation data as well. Accelerator experiments are particularly good at ν_μ related measurements and measurements of δ_{CP}.

The best measurement on $\sin^2(\theta_{12})$ of $0.307^{+0.013}_{-0.012}$ is from the KamLAND experiment analysis Abe et al. using 3 neutrino flavors and a constraint on $\sin^2(\theta_{13})$ of 0.0219±0.0014 from reactor neutrino experiments as well as all solar data and KamLAND data.

The best result for Δm^2_{21} is 7.53±0.18 10^{-5}eV^2 from GANDO 13 using a 3 neutrino model using KamLAND, global solar neutrino, short baseline reactor, and accelerator data

For $\sin^2(\theta_{23})$, PDG has done their own fit using results from IceCube, T2K, NOνA, MINOS, and SuperKamiokande atmospheric data. The result is $0.553^{+0.016}_{-0.024}$ for inverted mass ordering and $0.558^{+0.015}_{0.021}$ for normal ordering.

Similarly, Δm^2_{32} has a PDG fit using data from IceCube, T2K, the Daya-Bay experiment, NOνA, MINOS, SK atmospheric, and RENO. The sign on Δm^2_{32} is not yet known, and depends on the choice of mass ordering. The result is -2.529$\pm$0.029 10^{-3}eV^2 for inverted ordering or 2.455$\pm$0.028 10^{-3}eV^2 for normal ordering.

$\sin^2(\theta_{13})$ can be determined directly from reactor neutrino experiments, or indirectly from analysis of solar neutrino or accelerator oscillation. PDG averages these methods, including data from T2K with normal ordering only, Daya-bay, Ling Ao/AoII reactors, Double Chooz reactors, and Yongwang reactors. the result is $\sin^2(\theta_{13}) = (2.19\pm0.07)\times10^{-2}$

$\delta_{\rm CP}$ PDG uses values from (0,2π), while T2K usually uses ($-\pi$,π). These two notations are equivalent, so the PDG result will be quoted. PDG uses an average with data from T2K, NOνA, and SK atmospheric data. PDG uses an assumption of normal mass ordering for a quoted value of 1.19$\pm$0.22.

Chapter 2

T2K Experiment

The Tokai to Kamioka (T2K) Experiment is an off axis long-baseline neutrino experiment located in Japan that utilizes the Japan Proton Accelerator Research Complex (J-PARC) in Tokai, Ibaraki to create a high intensity muon neutrino beam that is detected by the near detectors (ND) and the far detector (FD), the Super Kamiokande detector, 295km away. The current aim of the T2K experiment is to make precise measurements of the PMNS Matrix neutrino oscillation parameters θ_{23}, Δm^2_{32}, Δm^2_{31} and search for CP violation from the parameter δ_{CP}.

2.1 Overview of the experiment and methods

The T2K experiment began taking data in 2009. The creation and detection of the neutrino beam are as follows: The 30GeV proton beam produced by the main ring of the Japan Proton Accelerator Complex (J-PARC) is focused onto a graphite target, producing a beam of mostly pions resulting from the hadron interactions in the target. These pions are focused by the focusing horns, which can focus either positively charged pions, or negatively charged pions depending on the direction of the horn current. These pions will decay the vast majority of the time into the corresponding charged muon and a muon neutrino or antineutrino depending on the charge of the pion. One of the Near Detectors (ND) is an on axis detector (INGRID) which measures the neutrino beam profile using a grid of scintillation detectors. In addition, a 2.5 degree off axis near detector positioned 280m downstream of the target, known as ND280, contains a variety of detectors enclosed within a magnet. The magnet allows for discrimination of particle charge and momentum. 295km away, the beam reaches the 2.5 degree off axis Super Kamiokande (SK) Far Detector (FD). The path of the neutrino beam from J-PARC to SK is shown in fig. 2.2. The goal of the ND detectors is to measure the beam before oscillation and constrain neutrino-matter interactions, while SK is positioned at a peak of electron neutrino appearance in the muon neutrino beam.

Pions decay primarily decay in a two body decay into

$$\pi^+ \rightarrow \mu^+ + \nu_\mu \tag{2.1}$$

or

$$\pi^- \rightarrow \mu^- + \overline{\nu}_\mu \tag{2.2}$$

since the center of mass of the daughter particles are boosted according to the pion's reference frame, the energy distribution of the neutrino flux has an angular dependence. Since the probability of oscillation depends on $\frac{L}{E}$, a narrow peak of neutrino energy tuned to the correct

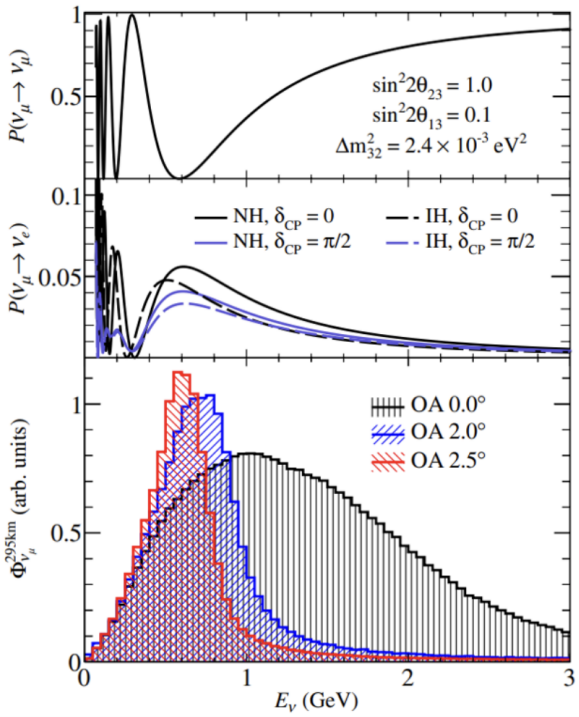

Figure 2.1: Muon neutrino survival probability(top), electron neutrino appearance probability(middle), and off axis flux for 0,2.0, and 2.5 degrees(bottom) as a function of neutrino energy E_ν

energy is desired in order to observe an oscillation maximum of $\nu_\mu \to \nu_e$. Fig. 2.1 shows the oscillation probabilities and off axis neutrino energy flux dependence on off-axis angle. The energy width of the neutrino flux is heavily restricted for an off axis angle of 2.5 degrees with a peak of ∼0.6 GeV near the desired oscillation maximum at 295 km for SK.

2.1.1 Goals of the T2K experiment

T2K is the successor experiment to the original K2K experiment which ran from 1999-2004 using a 12GeV proton beam at the KEK campus in Tsukuba and ascertained a 4.3σ confidence of muon neutrino disappearance [9]. The original goal of T2K was to continue this work and observe muon neutrino disappearance coinciding with electron neutrino appearance within the beam. By 2014, a 7.3σ [10] confidence in oscillation of $\nu_\mu \to \nu_e$ was observed. The current goal of the T2K experiment is to search for CP-violation in neutrino oscillations and make more precise measurements of oscillation parameters θ_{23}, Δm^2_{32}, and Δm^2_{31}

The latest result[11] by the T2K collaboration, published in 2023, used data obtained from 3.6×10^{21} protons on target. T2K data, in conjunction with reactor constraints, has a little over a 2σ significance for a nonzero value for δ_{CP}, indicating possible CP violation, with a preference for $\delta_{CP} = -\frac{\pi}{2}$, which would correspond to a maximally CP violating neutrino sector. T2K is still a significantly statistics limited experiment. Following the long shutdown in 2020, the beam was restarted in 2023 with Runs 12 and 13. The proton beam has recently exceeded its original design beam power of 750kW proton beam power, and is in the process of an upgrade towards an eventual goal of 1.3MW.

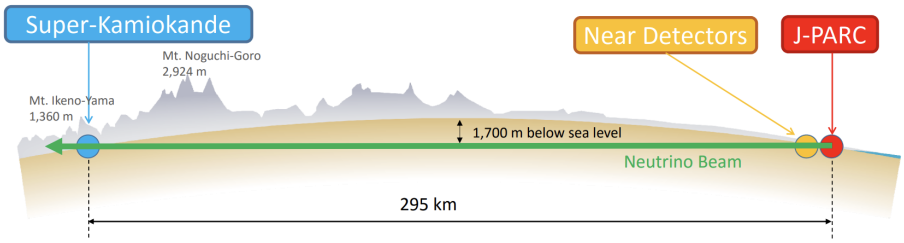

Figure 2.2: Path of the neutrino beam from J-PARC to Super Kamiokande

2.2 Accelerator and Proton Beamline

2.2.1 J-PARC Accelerators

The muon neutrino beam is generated at the accelerator facilities in J-PARC, located in Tokai, Ibaraki Prefecture. First, H^- ions from an ion source are accelerated in the Linear accelerator (LINAC) up to an energy of 400 MeV. Charge stripping foils convert the H^- ions into protons and these are injected into the Rapidly Cycling Synchroton (RCS), which accelerates the proton beam to an energy of 3 GeV. The proton beam is then injected into the Main Ring Synchrotron (MR), where it is finally accelerated to 30 GeV. The beam structure in MR is divided into 8 bunches for normal Running conditions, and has a repetition rate of 2.48 s before 2021, and after the long maintenance period ending in 2023, it is now 1.36 s. The total of all 8 bunches is called a spill. The beam is extracted to the neutrino beamline using a kicker magnet, and the beam is bent using a combination of normal conducting and superconducting magnets to the direction of the far detector. The beam then enters the final focusing (FF) section, where it is focused and directed onto the neutrino production target[2]. The final focusing section consists of 4 focusing quadrapole magnets, 2 horizontal bending magnets, 2 vertical bending magnets, along with an additional 2 vertical dipole magnets to bend the beam to the angle of -3.637 degrees towards SK. A drawing of the final focusing section is seen in fig. 2.3 Along the neutrino beamline, a variety of beam monitors and sensors measure the beam's position, direction, size, and intensity along the beamline to ensure its correct incidence on the target.

The neutrino production target is 91.4 cm in length, and is installed within the first of 3 magnetic focusing horns (from here called horn 1, 2, and 3). These horns are used to focus/defocus the charged pions resulting from the beam collision on the target. They have been operated at $\pm$250 kA until Run 13 in 2023/2024, where they have been upgraded to use the design current of $\pm$320 kA for the first time in normal Running. The polarity of these horns determines whether they select for positively or negatively charged particles, which corresponds to a muon neutrino and muon antineutrino beam respectively. The T2K experiment has alternated between using neutrino and antineutrino modes since 2014. Contaminations to the muon (anti)neutrino beam are mainly from kaon and muon decays into ν_e and wrong sign ν_μ.

2.2.2 Beam Monitors of the Neutrino Beamline

To properly understand the neutrino beam, detailed measurements, focusing, and tuning of the proton beam before it hits the target must be carried out. The beam is sampled by a variety of types of beam monitor to determine the properties of the proton beam when it is incident on the target. The location of the beam monitors are shown in fig. 2.4 and photographs of the

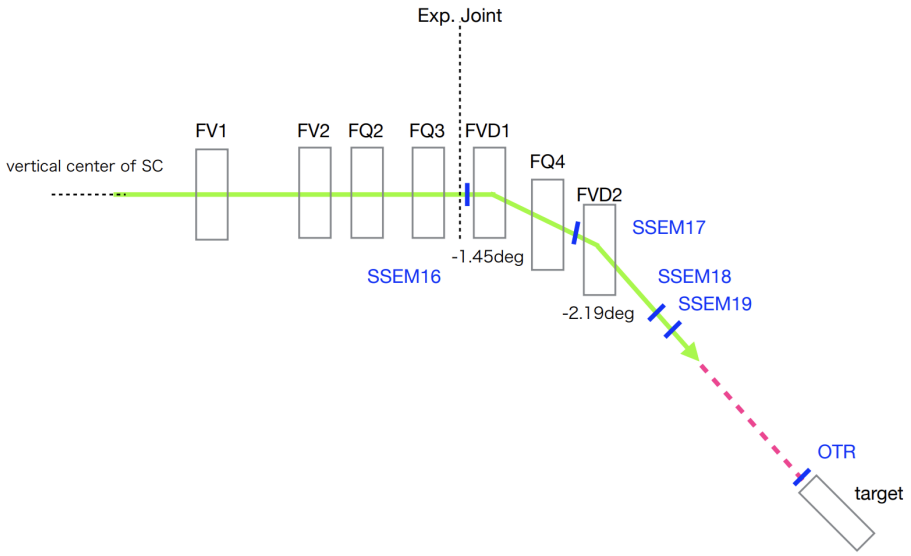

Figure 2.3: Drawing of the design orbit in the final focusing section Y-Z plane. The beam from the superconducting section (SC) enters the final focusing from the left and is bent by the vertical dipole magnets FVD1 and FVD2 into the direction of SK. The horizontal bending magnets are not pictured here.

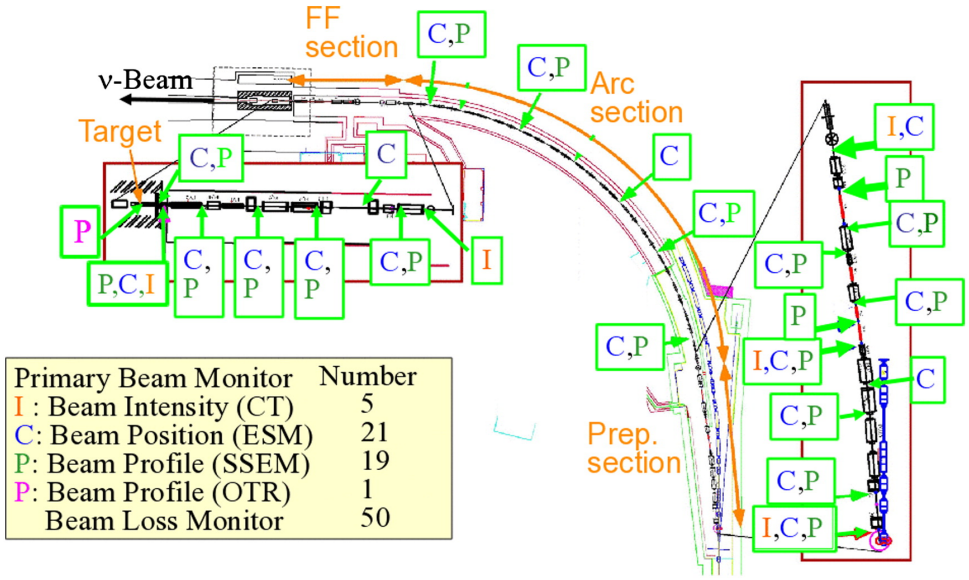

Figure 2.4: Location of beam monitors in the primary beamline.

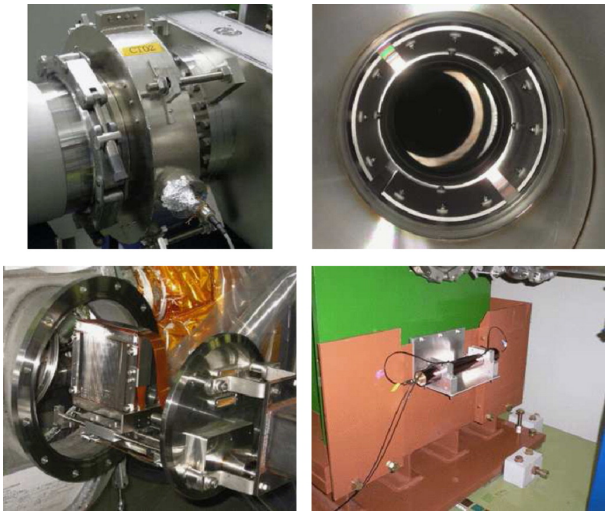

Figure 2.5: Photos of the proton beam monitors. Upper left: CT, upper right: ESM, lower left: SSEM, lower right: BLM

proton beam monitors are shown in fig. 2.5

CT:
CT is a current transformer that consists of a 50 turn toroidal coil around a cylindrical ferromagnetic ring core. When the beam passes through the inside of the ring, a current is induced in the coil via the magnetic field from the core. This allows for a measurement of the intensity of the proton beam.

ESM:
The ESMs are Electros-Static Beam Position Monitors (ESMs) which monitor the mean position of the proton beam. Each ESM has four segmented cylindrical electrodes surrounding the proton beam orbit. It monitors the center of the proton beam by measuring the assymetry of the induced current in the top/bottom and left/right electrodes. This allows for the measurement of the beam without any direct interaction. There are a total of 21 ESMs installed in the beamline.

SSEM
Each SSEM or Segmented Secondary Emission Monitor has two titanium foils separated into strips either horizontally or vertically with a positive HV foil in between. When the beam hits a strip, secondary electrons are emitted in proportion to the number of protons in the beam. The electrons drift in the electric field, and the compensating charge of each strip is read out as a pulse with positive polarity. From the resulting charge distribution on the strips, the beam profile can be reconstructed. Each SSEM causes 0.005% proton beam loss while in the beam path. Because of this, only the most downstream SSEM, SSEM19, is used during physics Runs, and the other 18 SSEMs are only used for beam studies and beam tuning.

BLM
The Beam Loss Monitor or BLM is a wire proportional counter filled with an Ar-CO_2 mixture. This is used to measure the beam loss. If the beam loss in a spill is too high, a beam abort interlock is triggered. 50 BLMs are installed to monitor beam loss along the primary beam line.

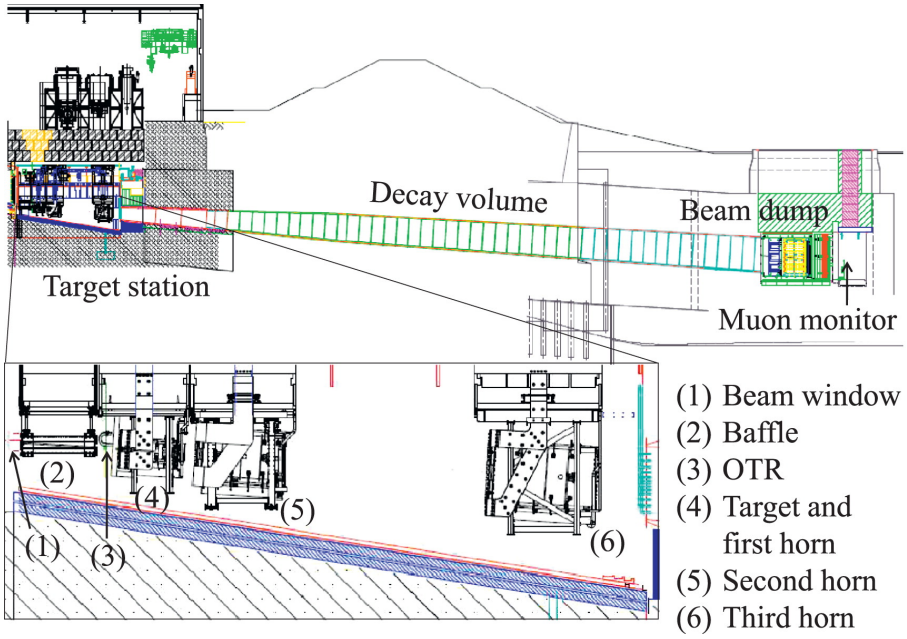

Figure 2.6: The secondary beamline

2.3 Overview of the secondary beamline

The secondary beamline is enclosed and separated from the primary beamline by the target station walls. It includes the target station, decay volume, beam dump, and the muon monitor. A schematic of the secondary beamline is shown in fig. 2.6, with more details of the target station shown in fig. 2.8. Protons pass through a beam window separating the helium filled target station from the vacuum of the primary beamline. The helium vessel refers to the helium filled vessel containing the target station, decay volume, up until the concrete wall at the end of the beam dump that is separated and kept filled with helium. The helium vessel is functions as a solid object separate from the rest of the J-PARC beamline. The final sensor before the target is the Optical Transition Radition Monitor (OTR). The proton beam then strikes the neutrino production target, creating primarily pions as a result. The three focusing horns focus either the positive or negative pions depending on if Running in ν mode or $\overline{\nu}$ mode respectively and defocus the other charge, in order to purify the neutrino/antineutrino beam in the direction of Super Kamiokande. The pions decay primarily along these channels:

$$\pi^+ \rightarrow \mu^+ + \nu_\mu \tag{2.3}$$

or

$$\pi^- \rightarrow \mu^- + \overline{\nu}_\mu \tag{2.4}$$

with a small fraction of the pions decaying into electrons and electron neutrinos. The majority of the pion decays occur in the 96m decay volume following the three focusing horns. At the end of the decay volume is the beam dump, which serves to stop the remaining protons, the remaining hadrons that have not decayed, and low energy muons. Located just after the beam dump is the muon monitor, which serves to sample the remaining high energy muons and monitor the neutrino beam indirectly through the muon profile, providing spill by spill information on the beam direction. Below is a more detailed explanation of each component.

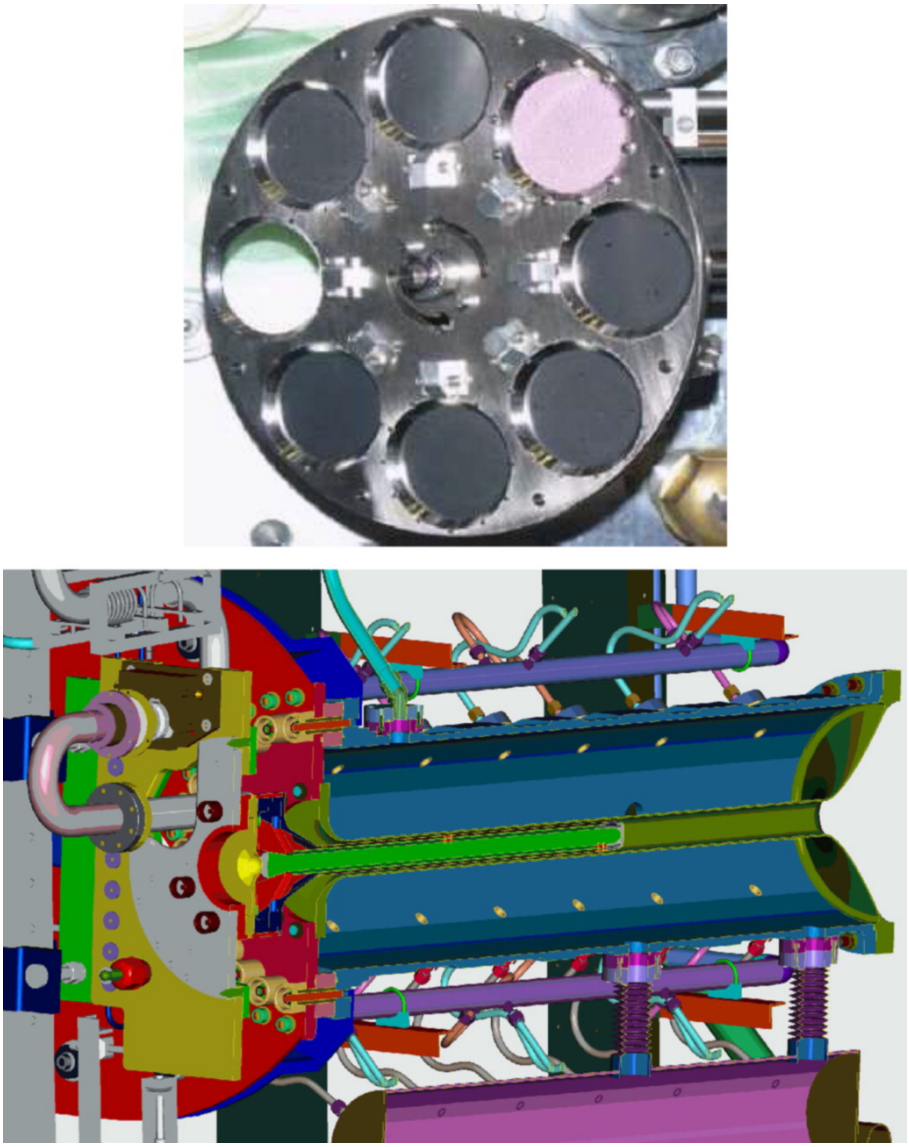

Figure 2.7: OTR monitor's foil rotation wheel (top) and the CAD model cut view for horn 1 with the target inserted inside (bottom).

Baffle
The baffle is located between the beam window and OTR in the target station. It is 1.7 m long, 0.3 m wide, and 0.4 m high graphite block, with a hole of 30 mm in diameter. The proton beam goes through this hole. The baffle is cooled via water pipes.

Target:
The neutrino production target is 91.4 cm in length with a diameter of 2.6 cm, and is installed within the first of 3 magnetic focusing horns (horn 1). The target is cooled by He gas.

OTR:
The OTR monitor uses optical transition radiation emitted from a thin metallic foil when the charged beam passes through it to monitor the beam position and width just before the target. Using a series of mirrors, the light is then sampled by a camera in a lower radiation environment.

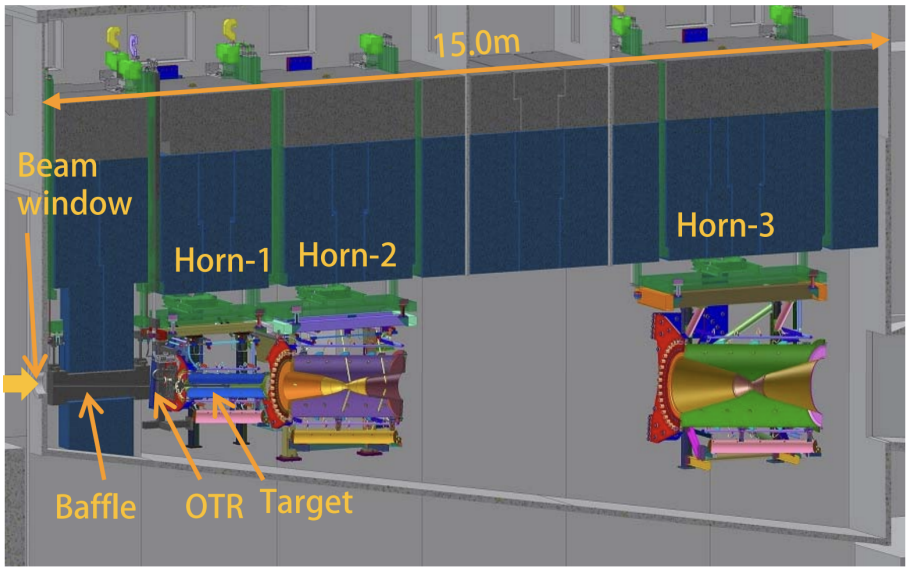

Figure 2.8: Target Station CAD drawing with horns labelled

Magnetic Horns:
The three magnetic horns serve to focus and select the desired charge of pions while defocusing the wrong sign pions. They function as coaxial conductors, using a pulsed current to generate a toroidal magnetic field in the space between inner and outer conductor. The strength of the magnetic field varies by $\frac{1}{r}$, where r is the distance from the horn axis. The selection between neutrino and antineutrino beam allows for the measurment of CP-Violation, since the value of δ_{CP} changes the oscillation probabilities for ν_μ and $\overline{\nu}_\mu$. The maximum design current of the horns is 320 kA, but the T2K experiment used 250 kA until Run 13, where 320 kA was used for physics runs for the first time. When run at 320 kA, the peak magnetic field is 2.1 T and the neutrino flux at SK increases by a factor of ∼16 at the spectrum's peak energy (0.6GeV) compared with the 0 kA horn current case. The placement of the horns in the target station is shown in fig. 2.8.

The decay volume, beam dump, and muon monitors are installed downstream of the target station.

Decay Volume:
The decay volume is a 96 m long tunnel filled with He gas. The length of the decay volume is such that most pions will decay (lifetime of $\sim$ .026 μs) along its length while most muons (lifetime of $\sim$ 2.2 μs) do not.

Beam dump:
The beam dump mostly consists of graphite blocks and iron plates and sits at the end of the decay volume. Its purpose is to absorb the remaining hadrons and low energy muons. Muons with energy of >5GeV generally pass through the beam dump. The structure of the beam dump is shown in fig. 2.9. The beam dump is located inside the helium vessel and is separated from the muon monitor by a concrete wall. Its core is made of 75 ton graphite (1.7 g/cm3), and is 3.174 m long, 1.94 m wide and 4.69 m tall. The total iron thickness is 2.40 m.

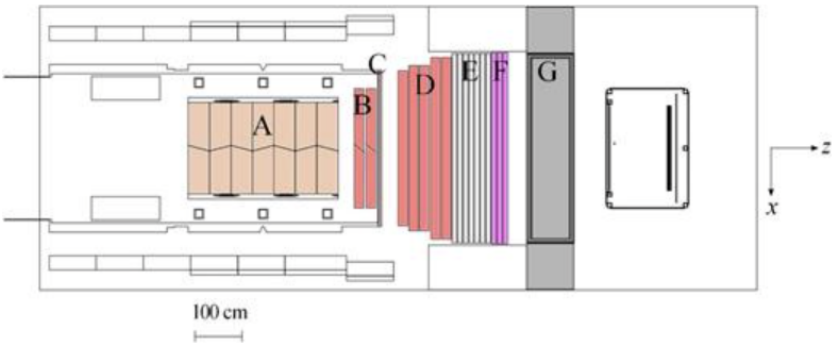

Figure 2.9: Top view of the beam dump. A is the graphite core, B-F are the iron plates, and G is the concrete wall. The beam travels along the Z-axis. The muon monitor is drawn just downstream of the concrete wall.

Muon monitor
The muon monitor is located just downstream of the beam dump. It consists of two arrays of sensors, the Ionization Chamber (IC) and silicon sensors (SI), and serves as a spill by spill indirect measurement of the neutrino beam intensity and direction by reconstructing the muon flux. The muon monitor will be discussed in more detail in section 3.

2.4 Near Detectors

The near detectors are installed 280 m downstream of the target in order to measure the neutrino beam direction and flux before oscillation and study neutrino-nucleus interactions. The primary near detector is the magnetized off axis detector called ND280. The magnetized off axis detector consists of a suite of particle detectors inside of a recycled magnet from the UA1 experiment at CERN. The original configuration of the near detectors are as follows. ND280 has since been upgraded, and this is detailed in section 2.4.1. At the most upstream part of the detector is a pi-zero detector(P0D) consisting of tracking planes of scintillating bars, alternating whether it is a water target or brass/lead foil. Downstream of the P0D is three time projection chanmbers (TPC), and two fine grain detectors (FGD) consisting of layers of finely segmented scintillator bars designed to measure charged current interactions in the FGDs. The P0D, TPCs, and FGDs are surrounded by an electromagnetic calorimeter (Ecal) for detecting gamma rays that do not convert while inside the inner detectors. The return yoke of the magnet contains scintillators to measure the ranges of muons that exit the sides of the off axis detector.

INGRID is an on axis detector designed to directly measure the neutrino profile. INGRID modules are comprised of iron plates and scintillator tracking planes. The intent of INGRID is to obtain a day by day measurement of the on axis neutrino flux by utilizing neutrino interactions with iron. The INGRID detector is comprised of 14 detectors arranged in a cross with one set of vertical and one set of horizontal detectors. The configuration is shown in fig. 2.10. The center of the INGRID cross is aligned with 0 degrees of the proton beam axis, corresponding to the design center of the neutrino beam. All 14 modules are installed in the near detector pit with a positioning accuracy of 2 mm perpendicular to the neutrino beam axis.

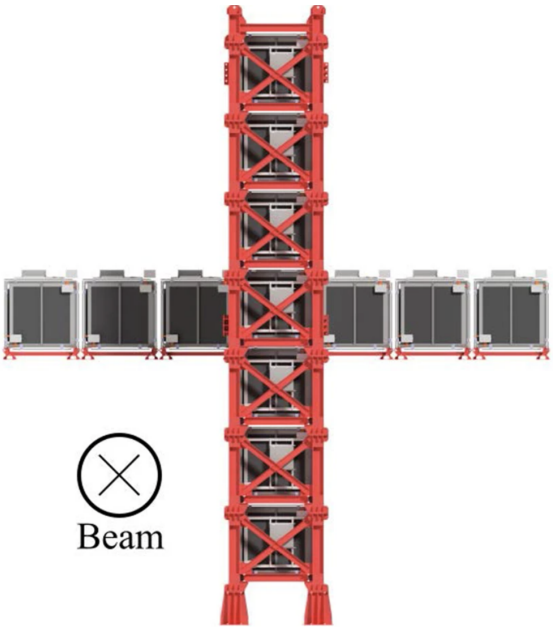

Figure 2.10: INGRID detector shape. Beam direction is into the page.

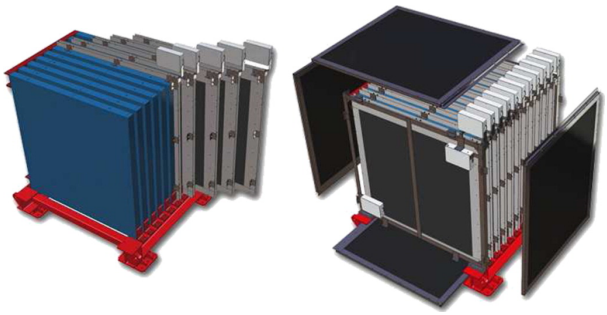

Figure 2.11: Inside of an INGRID module. The left image shows the tracking planes (blue) and iron plates. The right image shows veto planes (black).

2.4.1 ND280 Upgrade

As of 2024, the upstream ND280 modules besides the P0D have been replaced by a variety of new detectors[12]. The goal of the near detector upgrade is to bring systematic uncertainties down to the 4% level for the T2K-II phase, with the goal of a 3σ exclusion of CP-conservation if the mass ordering is known.

The improvements to ND280 are to achieve polar angle coverage of muons produced in charged current events, improve the tracking efficiency of pions and protons stopping inside the scintillation detector, and improve the separation of electrons from converted gamma-rays required for electron neutrino studies. The downstream part of ND280 was not changed in this upgrade, and will continue to take data and provide comparison to pre-upgrade data for the ND280 detector.

The new detector consists of a highly granular scintillator detector, the Super-FGD, sandwiched between two High-Angle TPCs(time projection chamber). These detectors are surrounded by six large TOF(time of flight) planes to determine track direction and improve particle identification.

The Super-FGD detector consists of many 1 cm^3 plastic scintillator cubes read out by three WSL optical fibers in orthogonal directions. Tests have shown that a minimum ionizing particle crossing a single cube produces more than 30 photoelectrons per WSL fiber. The timing resolution of the Super-FGD is better than $\sim$1 ns. This precision allows for tracking over 4π solid angle of pions and protons stopping in this detector. Additionally, the high granularity allows the distinguishing of electrons produced by electron neutrino interactions from converted photons.

The TPCs will measure charge, momentum, track angles, and $\frac{dE}{dx}$ with good efficiency and low systematics. Preliminary measurement in the test beam show that the space point resolution is at the 300 µm level, to be compared to 600 µm for the existing TPC.

The TOFs, consisting of cast plastic scintillator readout by MPPC, will reach a time resolution of 150 ps.

2.5 Super Kamiokande

The far detector used in the T2K experiment is Super Kamiokande(SK), a large water cherenkov detector located within Mt. Ikenoyama in Hida, Gifu, about 295 km west of J-PARC. A schematic of the SK detector is shown in fig. 2.12 The purpose of the far detector is to search for electron neutrino appearance and muon neutrino disappeance as the result of neutrino oscillation. Although $\nu_\mu -> \nu_\tau$ also can occur, most of the energy of the neutrino beam is below the τ rest mass of 1.777 GeV[8], so interactions producing τ are forbidden. The SK detector is located 1 km beneath the surface of Ikenoyama to reduce the background from cosmic ray particles, with the muon rate being reduced to about 2 Hz. The SK detector is a large cylindrical cavern filled with 50 kton of pure water surrounded by about 13,000 photomultiplier tubes(PMTs) to image the cherenkov radiation from the neutrino interactions. The Super Kamiokande detector has been running since 1996, and has the leading limits on the measurement of proton decay, as well as measurements of atmospheric, solar, and astrophysical neutrino interactions.

Cherenkov radiation is used to detect particles within SK using PMTs. Cherenkov photons are emitted by charged particles moving through a dielectric medium faster than the phase

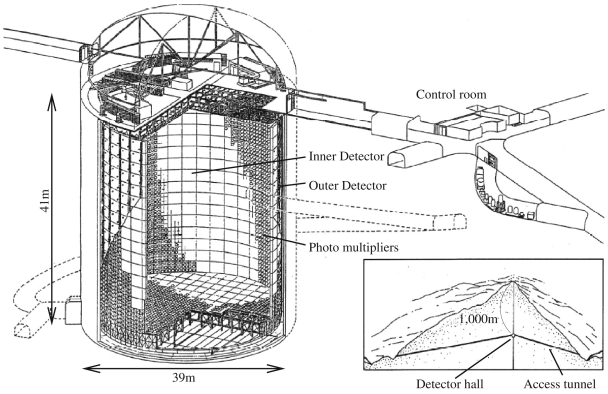

Figure 2.12: Schematic of the Super Kamiokande Detector.

velocity of light in that medium (75% the speed of light in a vacuum for water). This light travels out in a cone in the direction of the charged particle with an angle of

$$\cos\theta = \frac{1}{n\beta} \tag{2.5}$$

Where n (n=1.33 for water) is the refractive index of the dielectric medium, and $\beta = \frac{v}{c}$ is the ratio of the particle's velocity to the speed of light. When neutrinos interact with the nuclei of the water molecules, there are a few different methods of interaction (see eqn. 1.17).

The T2K experiment primarily selects charged current quasi-elastic (CCQE) interactions, which are namely characterized by eq. 1 & 3 of eq. 1.17 that have a final state lepton corresponding to the flavor of the interacting neutrino. Since the direction of the neutrino is well known from the accelerator flux, the interaction can be reconstructed from the Cherenkov rings. It is possible to discriminate between e and μ events via observation of the ring. Rings from electron events appear "fuzzier" compared to muons due to electromagnetic showers.

The sensors used in Super Kamiokande are photomultiplier tubes (PMTs). Photomultiplier tubes amplify the signal of a photon incident on the detector to a signal that can be used in electronic readout. First, the photon kicks off an electron from the photocathode via the photoelectric effect. The induced electrons are focused by a focusing electrode onto the first dynode. High voltage differences between the dynodes accelerate the electrons, which emit more secondary electrons upon collision in a cascade until the multiplied electrons are collected on the anode.

2.6 Beam Direction Effects and Systematic Uncertainties

The T2K experiment has a wide variety of neutrino energy dependent systematic uncertainties on the neutrino flux prediction related to the experiment that have been slowly reduced over the years. The largest of these is uncertainty on hadron interactions, which arise due to the modelling of the target in the flux prediction simulations. This has been reduced using a replica target with the NA61/SHINE experiment at CERN. Additional uncertainties in T2K are interaction modelling due to hadron-neutrino cross sections and removal energies of the nucleon from nucleus in SK. These have been reduced with experimental measurements of neutrino-nucleus cross sections in ND, as well as better modeling of nucleon structure within Monte Carlo simulations using spectral functions instead of a fermi gas model.

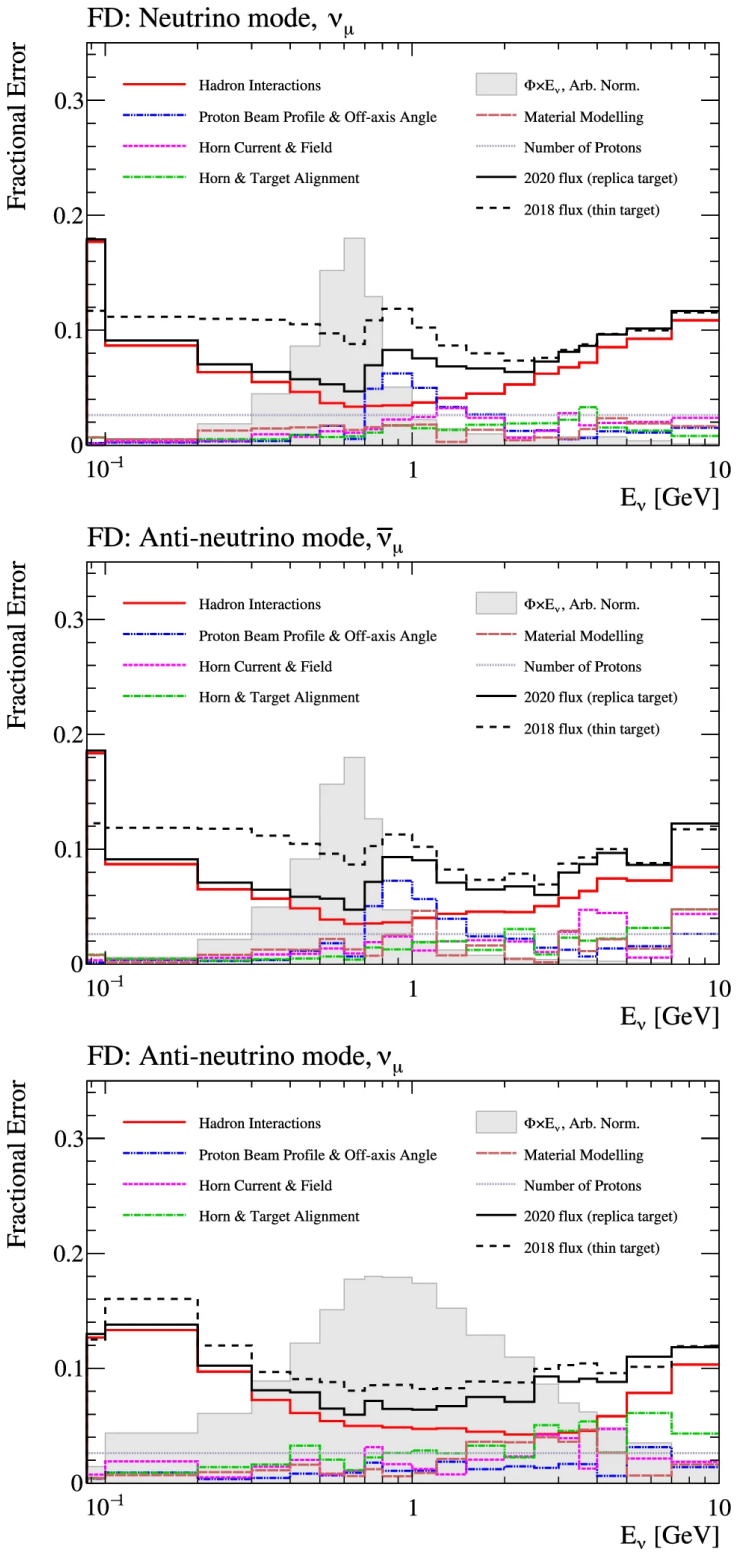

Figure 2.13: Neutrino flux prediction systematic uncertainties included in the T2K 2023 oscillation analysis.

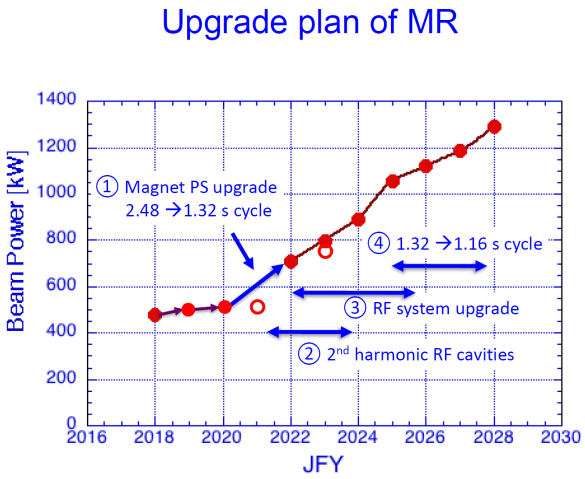

Figure 2.14: MR upgrade timeline. The open circles represent the actual peak beam power during that year.

A large contribution of error in the high energy neutrino flux is uncertainties on the proton beam profile and neutrino beam off-axis angle, which significantly contribute to the uncertainty on the high-energy edge of the flux peak, demonstrated in the first image of fig. 2.13. This arises due to the fact that the width of the neutrino energy spectrum is directly affected by shifts in the off-axis angle. Hadron interaction errors are planned to be further reduced in the next analysis by modeling Kaon decays using the NA61/SHINE data in the next oscillation analysis, which will reduce the overall uncertainty at higher energies to $\sim 5\%$.

2.7 Future of the T2K Experiment

At its core, the T2K experiment is still a very statistics limited experiment, so in order to reach the goal of constraining the neutrino CP-violation, a greater volume of statistics is required. T2K is currently in the process of upgrading the beam power to a goal of 1.3 MW. Additionally, as of Run 13 in 2023/2024, the focusing horns were able to be ran at their design horn current of 320 kA, providing a stronger focusing effect and increasing the effective neutrino flux.

Beam power is directly related to the neutrino flux at the far detector, so increasing the intensity and repetition rate of the accelerator increases the available statistics per beam Run. In Run 13 in 2024, the main ring was successfully Run at the original design beam power of 750kW. Over the course of the next few years, various upgrades to J-PARC facilities as well as the neutrino beamline will take place to facilitate beam power up to 1.3MW. The timeline of the expected beam power is shown in fig. 2.14.

Hyper Kamiokande is the next generation detector of Super Kamiokande, and is the successor experiment to T2K. Similar to SK, Hyper Kamiokande is a water Cerenkov detector that is sampled using a coverage of PMTs. It is about 5 times larger in volume, and the inner detector will be covered by about 20,000 PMTs and 800 multi-PMTs. As well as about 3,600 PMTs instrumenting the outer detector which will serve as a method to detect particles entering the inner detector, such as cosmic muons. The dome of the structure was successfully excavated in October, 2023. Data taking expected to begin in 2027.

Chapter 3

Muon Monitor

A spill by spill measurement of the neutrino beam intensity and direction is vital to observe the stable operation of the neutrino beam. To accomplish this, the muon monitor was created to measure the muons produced alongside muon neutrinos from pion decays, generally along the channel below:

$$\pi^{\pm} \rightarrow \nu_{\mu} + \mu^{\pm} \tag{3.1}$$

This two body decay implies that the kinematics of the observable muon are strongly correlated to that of the invisible neutrino. Thus, measuring the muon profile provides an indirect measurement of the neutrino beam direction with the advantage of a spill by spill measurement possible with charged particles. The Muon Monitor sensors are located about 118m downstream of the target. Higher energy muons are able to pass through the beam dump where they deposit energy in the mumon sensors, which are read out and the accumulated charge is integrated to obtain the muon profile.

3.1 Overview

The Muon Monitor[13] was designed with a few key requirements for measuring the beam operation:

1. Monitor the neutrino beam intensity with a precision of better than 3%.

2. To measure the neutrino beam direction with a precision of better than 0.25mrad, which corresponds to a 3cm precision of muon profile center.

3. To measure the beam intensity and direction on a bunch by bunch basis.

4. To measure the intense muon beam of $10^5 - 10^7 \text{muons/cm}^2\text{/bunch}$

5. To be tolerant to radiation and resistant to activation.

6. To run stably to minimize downtime and repair.

The beam dump is constructed such that only muons with energy of >5GeV can pass through the beam dump and reach the muon monitor. The beam dump must eliminate the remaining hadron flux, while allowing enough of the muon flux through to properly sample the neutrino

Figure 3.1: The inside of the mumon enclosure. The two sensor sets can be seen, left: IC, right: SI

beam. The resulting muon flux follows a gaussian distribution with a width of approximately 100 cm depending on the horn current.

In order to reconstruct the muon profile, two sets of 49 sensors are placed covering a 150 cm×150 cm plane instrumented with two sets of sensors for the purpose of redundancy. These sensors are located in an aluminum enclosure in the mumon pit, which sits underground just behind the beam dump. A photo of the mumon enclosure is shown in fig. 3.1 and a schematic of mumon is shown in fig. 3.2.The first sensor set is comprised of an array of silicon PIN photodiodes abbreviated as SI. Each SI sensor is spaced at a distance of 25 cm from each other and is mounted on the upstream end of the muon monitor enclosure. The second sensor is an array of ionization chambers consisting of 7 chambers split into 7 segments for a total of 49 sensors. A 2D gaussian fit is performed using the integrated charge read out using a flash ADC readout from each array of sensors. The parameters of this fit are used to characterize the muon profile.

While the beam is running, the mumon pit is subject to an absorbed dose of 100 kGy over 100 days with the beam running at 750 kW of beam power. As such, the sensors and equipment used in the muon monitor must be radiation tolerant and resistant to activation. Currently, SI sensors are less resistant to radiation and must be swapped out alternating in a checkerboard pattern once their dark current exceeds a certain threshold. In the future of the T2K beam, namely as the beam power continues to increase past the original design consideration of 750 kW, the SI sensor must be retired in favor of a more radiation tolerant sensor. The current candidate sensor to accomplish this is the Electron Multiplier Tube (EMT). As of Run 13, 7 of these EMTs are arranged along the horizontal axis mounted behind the SI sensors.

The sensors are calibrated at the beginning of each period of beam Running. The SI array and the 7 EMTs are calibrated using a reference SI sensor that has been used since the muon monitor began taking data. During continuous beam running, the reference SI sensor is moved into position a few centimeters downstream of the sensor being calibrated. The ratio of the integrated ADC count between the reference SI sensor and the test sensor are recorded and all of the sensor's outputs are normalized by these ratios to reduce biases from individual sensors or readout gain variations from affecting the fit.

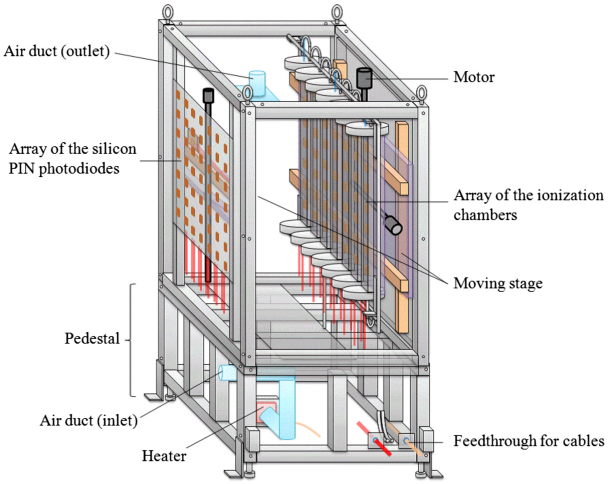

Figure 3.2: A schematic of the muon monitor. The muon beam travels from left to right.

The IC sensor is calibrated by moving the entire sensor array by 25cm in each direction using a moving stage, for a total of 8 offset positions. The sensor differences are checked and similarly ratios between each sensor can be found such that all of the sensors can be normalized. Since the calibration must be carried out while the beam is operating, the moving stages for both IC and the SI reference sensor are controlled remotely from the MUMON hut, located just above the mumon pit, and also where the readout electronics and data acquisition computers are located.

3.2 Silicon Sensor (SI)

The Silicon array is constructed using 49 silicon PIN photodiodes (HAMAMATSU S3590-08) laid out in a 7x7 grid with 25 cm of spacing between each photodiode. Each photodiode has an active area of 10 mm×10 mm with a depletion layer thickness of 300 μm. The silicon layer is mounted on a ceramic base and an 80 V bias voltage is applied to fully deplete the depletion layer.

The silicon PIN photodiode is not tolerant of the radiation present in the mumon pit during the beam operation. Studies of the silicon PIN photodiodes have been carried out[14] to study the radiation effects on the sensor. As a 647 MeV proton fluence increases, the depletion voltage of the tested 200 μm thick PIN detectors decreases. The depletion falls about 50% at about 0.7×10^{13} protons/cm^2 and reaches a minimum at 1.25×10^{13} protons/cm^2 for a detector at 27°C before reaching a type inversion point where the semiconductor switches from n-type to p-type. In the case for T2K, although the beam dump stops the proton flux nearly completely, there is a significant fluence of 1-MeV neutrons estimated at $\sim 10^7$ 1-MeV neutrons/cm^2/spill at 750 kW beam operation. 1 MeV neutrons deliver similar levels of radiation damage to the silicon detectors[15], therefore, for 750 kW beam operation, the depletion voltage is expected to fall about 50% after 0.7×10^6 spills, or equivalently a month of beam operation. The actual degradation due to radiation damage was shown to be lower than this theoretical calculation [16], however, Si sensors still need to be replaced more frequently as beam power increases. The dark current of the silicon PIN detectors is measured during maintenance, and if the value is too large, the sensors are replaced in a checkerboard pattern such that half of the old sensors remain. The reference SI sensor has never been replaced, so it has sustained significant radiation

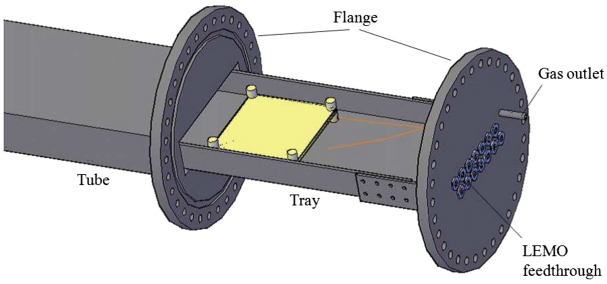

Figure 3.3: Drawing of the inside of one of the ionization chambers removed from the tube.

damage despite being stored ∼110 cm off the beam axis (-75 cm, -80 cm). Since the reference SI sensor is only used to find the ratios between the main 49 SI sensors, this is expected to induce little error on the calibration. However, as the T2K beam is pushed towards higher beam power, specifically once the beam reaches 1.3MW, SI sensors would need to be replaced every month during beam operation, which is unfeasible for normal beam operation and radiation exposure to the workers. As such, soon the SI array will be replaced by a new, more radiation tolerant candidate sensor: the Electron Multiplier Tube (EMT) discussed in section 3.4.

3.3 Ion Chamber (IC)

The ion chamber array consists of seven ion chambers containing seven sensors for a total of 49 sensors spaced similarly to the SI array. The sensors sit in a 1929 mm long aluminum tray at an interval of 250mm. The trays are inserted into a 150×50×1956 mm^3 aluminum tube. At each end of the tube, aluminum flanges 235mm in diameter are welded. Other aluminum flanges are attached to them and seal the tube with O-rings. Gas flows through 1/4 inch tubes welded to the flanges. On the bottom flange, 14 feedthrough connectors (LEMO SWH.0S) for both signal and HV cables are mounted. The LEMO feedthrough is sealed with an O-ring. In three of the chambers, a Pt100 resistance thermometer(PRT) is installed to measure the temperature inside the tubes. The inside of an IC tube is shown in fig. 3.3.

Each sensor of the ionization chamber consists of two parallel alumina-ceramic plates spanning 100×100×1 mm^3 separated by 3 mm using ceramic spacers with a tolerance of 100 μm. The signal electrode is surrouded by a grounded electrode to ensure a constant electric field. Ionization pairs created by charged particles in the 75×75×3 mm^3 volume contribute to the signal. Conductive parts except for the electrodes are isolated from the gas in order to prevent stray ionization from collecting on the conductors. A schematic of an IC sensor is shown in fig. 3.4.

The ionization chamber is filled with two mixtures of gas that can be switched depending on beam intensity. Ar + 2% N_2 for a low intensity beam, and He + 1% N_2 for a high intensity beam. The relative signal for the He to the Ar is 1 order of magnitude of difference. This is due to the ion yields for particles with the least energy loss, minimum ionizing particle (MIP), at STP are 95.6cm^{-1} for Ar and 7.80cm^{-1} for He. During Run 12 and 13, the beam was ran at high intensity, so the gas used during beam operation was the He mixture. N_2 is added as a quencher, which also increases response time. N_2 also serves to saturate the Jesse effect, which is the large increase in ionization due to impurities in the gas, subsequently removing these dependencies on the impurities in the gas. A diagram of the gas system is shown in fig. 3.5.

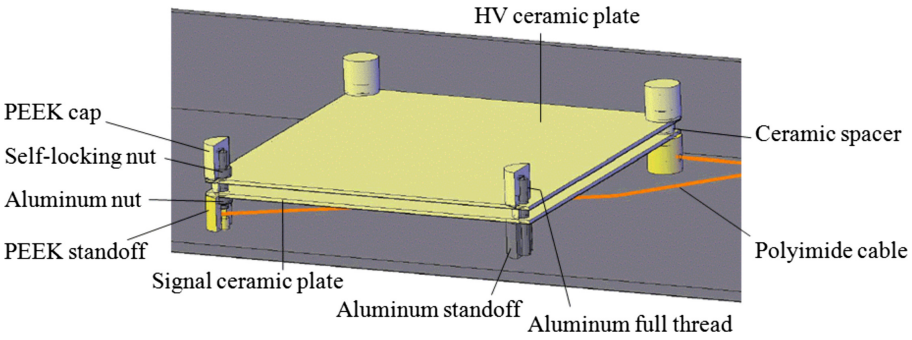

Figure 3.4: Drawing of an ionization chamber sensor.

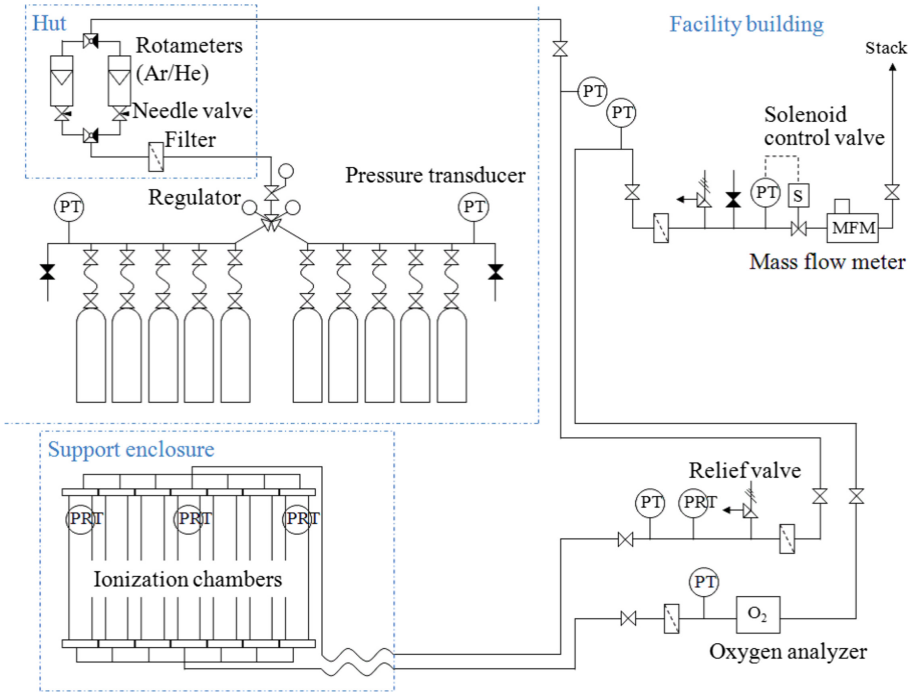

Figure 3.5: A diagram of the IC gas system. PT stands for pressure transducer, and PRT is the Pt100 resistance thermometer.

The gas system is fed by two sets of 5 7-m^3 gas cylinders located above ground next to the Mumon hut. These two sides can be selected between using a 3 way valve and the pressure on each side is measured using a pressure transducer. At the junction of the two sets, a regulator compresses the gas to 0.2 MPa. Downstream of the regulator, the flow rate is set to 100 cc/min. Two rotameters for He and Ar gas are built into the line and are exchangeable with ball valves at their inlet and outlets.

3.4 Electron Multiplier Tube (EMT)

As discussed in the SI sensor section, the silicon photodiodes are not very radiation resistant, and their yield decreases as they are irradiated from the particle beam. As the T2K beam enters an era of higher than 750kW beam power with the horns Running at 320kA, the rate at which SI sensors would need to be replaced to facilitate the stable Running of the muon monitor is too frequent to justify the cost. To continue operating in the high beam power era of T2K, a

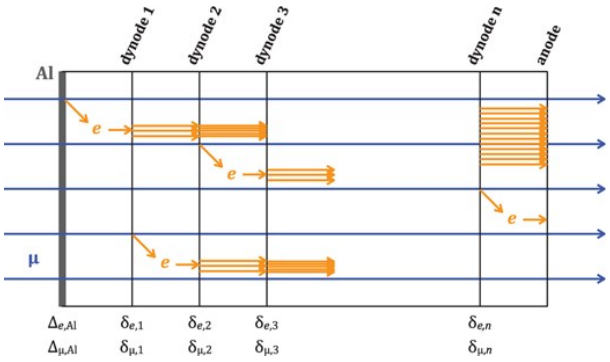

Figure 3.6: A diagram of the signal amplification of the EMT with a muon flux. [1]

new sensor must be employed in the absence of the SI array. After testing several sensor types, the current best candidate is the Electron Multiplier Tube, or EMT.

For use as a sensor in the muon monitor for the T2K beam, a sensor must have a fast signal response in order for bunch-by-bunch monitoring of the muon beam. Additionally, the sensor must have a signal yield large enough to observe the muon beam without further electronic amplification. Photomultipler Tubes (PMTs) use secondary emission of electrons to multiply the electrons from the emitted from PMT's photocathode. In the case of muon detection, a muon passing through the PMT will knock off secondary emission electrons from the dynodes, which are then amplified by the PMT. Since this does not require the photoelectric effect, the photocathode can be removed, thus called an Electron Multiplier Tube (EMT). This photocathodeless PMT is currently being considered as the replacement sensor for the SI array [1].

When a muon passes through an EMT, secondary electrons are produced at the aluminum cathode or at the dynodes. These secondary electrons are accelerated by the electric field in the EMT, and create more secondary electrons when impacting the downstream dynodes. Fig. 3.6 shows a diagram of the signal amplification within the EMT. Δ represents the secondary emission efficiency of the aluminum cathode, and δ represents each dynode. μ and e represent muons and electrons respectively. The main difference with muon detection in EMTs compared to normal PMT operation is not all initial signal electrons originate at the cathode, instead, the muon can also kick electrons off the dynodes, so the signal gain for each secondary electron is different depending which dynode layer they originate from. The secondary emission efficiency δ depends on particle energy, so in principle $\delta_{\mathrm{e,i}}$ and $\delta_{\mathrm{e,j}}$ are not the same. For a normal PMT, the gain is determined by multiplying the secondary emission efficiencies of each dynode.

$$G = \delta_{e,1} \times \delta_{e,2} \times ... \times \delta_{e,n} = \prod_{i=1}^{n} \delta_{e,i} \tag{3.2}$$

For the muon monitor, the signal is primarily generated by muons and δ-ray electrons knocked out by muons. The energy distribution of these particles in simulations is discussed in detail in sec. 4.2, but a significant fraction of high energy electrons can reach 10s-100s of MeV. Muons and high energy δ-rays can penetrate the EMT, while most secondary emission electrons are stopped by the dynodes. Therefore production of additional secondary electrons from the primary incident particle must be considered at each dynode interface. The output of the EMT signal is therefore

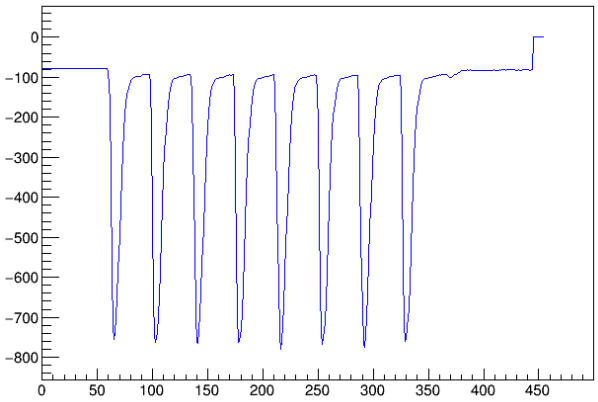

Figure 3.7: Mumon SI sensor waveform shape for 8 bunch high intensity beam.

$$Q = Q_\mu + Q_e, \tag{3.3}$$

$$Q_\mu = e \times \phi_\mu \times \left\{ A_{\text{sur}} \cdot \Delta_{\mu,\text{Al}} \cdot \prod_{i=1}^{n} \delta_{e,i} + \sum_{i=1}^{n-1} \left(A_i \cdot \delta_{\mu,i} \cdot \prod_{j=i+1}^{n} \delta_{e,j} \right) \right\}, \tag{3.4}$$

$$Q_e = e \times \phi_e \times \left\{ A_{\text{sur}} \cdot \Delta_{\text{e,Al}} \cdot \prod_{i=1}^{n} \delta_{e,i} + \sum_{i=1}^{n-1} \left(A_i \cdot \delta_{\mu,i} \cdot \prod_{j=i+1}^{n} \delta_{e,j} \right) \right\}, \tag{3.5}$$

e is the elementary electric charge, A_{sur} and A_i are the area [cm^2] of the aluminum cathode and dynodes respectively, and ϕ_μ and ϕ_e are the muon flux and δ-ray flux [/cm^2]. The first term corresponds to secondary emission at the aluminum cathode, and the second term corresponds to the secondary emission and subsequent amplification at each dynode i.

As of Run 12 and Run 13, there are 7 EMTs installed behind the center row of the SI array, as well as 2 EMTs mounted on the wall of the muon monitor chamber. They are being tested in-situ during beam operation for radiation tolerance, linearity, and 1D fitting of the muon profile.

During the summer maintenance in 2024, a cross shape(+) will be installed in the Mumon pit behind the SI array in the central column and central row. Additionally, a second EMT will be placed behind the centermost position to check for inconsistencies between the EMT sensors at the same position in the flux. Following this period, 2D fitting of the muon profile will be done using a "star"(*) configuration of 25 EMT sensors, again mounted behind the SI array. This configuration was chosen as a result of the study detailed in chapter 8.

3.5 Analysis and Profile Reconstruction

The muon profile is measured by the two sets of 7x7 sensor arrays as described above. The accumulated charge is read out and binned into a 2D position histogram of 7×7 bins, spanning -87.5 cm to +87.5 cm (175 cm in width) in both x and y, with the center of each of the histogram boxes being the position of the center of the sensor. This histogram is fitted using a 2D gaussian distribution described by the equation below.

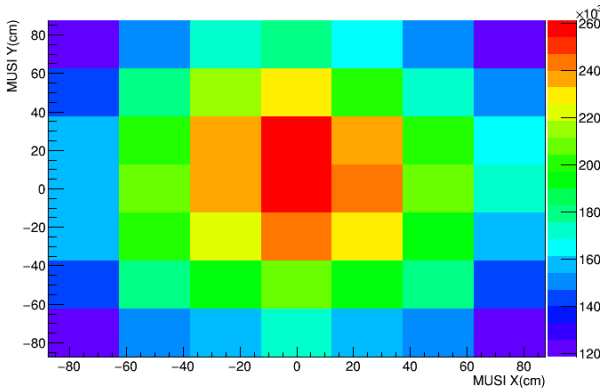

Figure 3.8: Muon monitor Si profile during a physics Run in Run 13. Color represents integrated charge from each sensor.

$$f(x,y) = C \times Exp\left[-\left(\frac{(x-x_0)^2}{2\sigma_x^2} + \frac{(y-y_0)^2}{2\sigma_y^2}\right)\right] \tag{3.6}$$

Where x_0 and y_0 are the x and y centers, and σ_x and σ_y are the x and y widths while C is the height of the gaussian. Using the x and y centers, the muon beam direction can be reconstructed. Since the distance from the target is 118m, a 0.1 mrad muon beam angle is approximately a 1.18 cm shift in the mumon center. The muon monitor resolution of the reconstructed profile is better than 0.03 mrad [16]. An example of the reconstructed muon profile from the SI array during 320 kA operation in Run 13 is shown in fig. 3.8, and the waveform seen by an SI sensor is shown in 3.7.

3.6 Systematic Errors

To estimate the systematic errors on the fit results of the mumon profile, various MC tests were carried out[16]. These are:

1. Uncertainty in the structure of upstream materials,
2. δ-ray contamination in the muon beam,
3. uncertainty in the relative calibration of the sensors,
4. alignment error of the muon monitor,
5. effect of the tilted beamline.

3.6.1 Profile Distortion

The assumption vital to reconstructing the muon beam profile is that the integrated charge can be described well with a 2-dimensional gaussian distribution. Materials upstream of the muon monitor can affect the distribution. Additionally, secondary particles generated from nearby materials, namely in the form of low energy δ-rays, can further distort the profile.

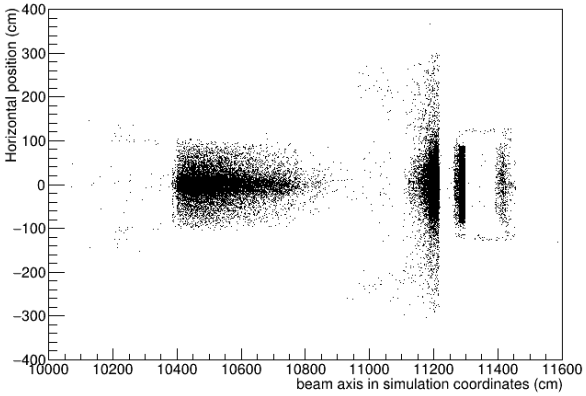

Figure 3.9: Particle creation position in JNUBEAM simulation. Each black vertex represents the creation position of 1 particle hit in the mumon SI plane. The concrete block at the end of the beam dump, and gamma ray backscattering from the mumon structure can be seen.

The beam dump sits directly upstream of the mumon pit, and it consists of a graphite core, followed by a variety of iron plates, with a large concrete block, as shown in fig. 2.9. There exists uncertainties on the density and thickness of the materials present in the beam dump. Deviations in these materials can create non-uniform path lengths of muons in the beam dump and can affect the resulting profile. These values were varied out to their 1σ limits derived from the tolerances in construction, which are taken to be twice the 3σ limits. In JNUBEAM these 1σ limits were used as inputs for the beam dump materials in the simulation. Overall, an error of 0.38cm was assigned to the systematic error of the profile center.

The width of the muon beam profile is generally 100-110cm when the beam is operated at 250kA, and ∼80-90cm at 320kA, which means the 150cm width of the muon monitor covers about ∼50% of the actual muon beam profile. In order to check for deviations at the edge of the muon beam profile, the IC chamber was moved by ±25cm to measure the edge, then the fit was done in each of these offset regions to to take the tail of the profile into account. If the profile is a perfect gaussian, the fitted result should be the same in all of these locations. The shift in the fit center between these 8 locations resulted in a difference of 1.25cm in the horizontal direction and 1.12cm in the vertical direction which are taken to be the systematic error from this effect. Additionally, during beam operation, a discrepancy of profile center is seen between IC and SI arrays, with 0.55cm in the horizontal direction and 1.77cm in the vertical direction. This is considered to be because of the nearby structures in the mumon enclosure. The structure most likely to cause this is the moving stage for the reference SI sensor used for calibration located just behind the SI array. During calibration while the stage is moving, there was a -1.4cm shift observed in the profile vertical center. The systematic error is taken to be 1.25cm for the different IC array positions, and 1.77cm for the difference between SI and IC are taken as the systematic errors of the profile distortion. These are added conservatively since the exact causes of the difference between SI and IC center are not distinguishable.

The gains of the sensors are calibrated with a precision of 0.4% for the ionization chambers and 0.1% for the silicon PIN sensors. The uncertainty is propagated to the error in the fitted muon profile to be 0.08cm in the horizontal and 0.30cm in the vertical direction.

In total the systematic error from the profile distortion is estimated to be 2.20cm in the horizontal direction and 2.22cm in the vertical direction.

Error Source	Δx (cm)	Δy (cm)	$\Delta\theta_x$ (mrad)	$\Delta\theta_y$ (mrad)
Profile Distortion	2.20	2.22	0.187	0.188
Tilted Beam	N/A	0.22	N/A	0.019
Alignment	0.63	0.65	0.054	0.055
Total	2.3	2.3	0.19	0.20

Table 3.1: Table of the systematic errors on the muon monitor beam profile center measurement.

3.6.2 Alignment Error of the Muon Monitor

The alignment accuracy between the target and the muon monitor is taken into account for the systematic error on the muon beam direction. The error mainly stems from the error on the relative positions of the reference points between the target and mumon pit that were used for the alignment. This is determined to be 0.61 cm for the horizontal position and the 0.65 cm for the vertical position. Alignment error of the muon monitor is 0.1 cm and the alignment error of the target is <1 mm. The total alignment error of the muon monitor relative to the target is 0.63 cm horizontal and 0.65 cm vertical.

3.6.3 Effect of tilted beamline

The beamline is tilted by 3.637 degrees vertically while the level of the beam dump is even with the ground. This results in an asymmetric path in the muons travelling through the beam dump to the muon monitor. This results in a difference of 1.35 cm profile shift in the vertical direction which was estimated using a MC simulation where the center of the proton beam is set to the center of the target and parallel to the beam axis. This correction is applied to the muon monitor and the MC statistical error of 0.22 cm is assigned as the systematic error of this correction.

3.6.4 Total Systematic Errors on the Mumon Profile

Table 3.1 summarizes the total systematic errors estimated on the muon beam profile. As mentioned in sec. 3.6.1, some of these errors may originate from the same origin, but they are treated conservatively with a quadratic sum of errors for a total systematic error on the beam direction of $\sqrt{0.19^2 + 0.20^2} = 0.28$ mrad.

Chapter 4

Analysis of the Muon Profile

Understanding the properties of the muon flux observed at MUMON is important to understanding the properties of the beam in the secondary beamline. To accomplish this, a Monte Carlo simulation using Geant3, called JNUBEAM, of the secondary beamline and the muon monitor was used.

4.1 Overview of Simulation Methods

JNUBEAM is a particle simulation software for the secondary beamline of the T2K experiment based on GEANT3[17]. The geometry of the secondary beamline is replicated in the simulation, and additionally simulates the effects of horn magnetic fields.

Due to a disagreement between the GEANT3 model for 30 GeV proton hadronic interactions and those measured in the NA61/SHINE[18] experiment at CERN, FLUKA 4-2.1[19][20] is used to simulate the interactions within the baffle and target. The FLUKA simulation only includes the region immediately surrounding the baffle and target. Once a particle exits this region, the information of its position, momentum, and the chain of interactions recorded by FLUKA is imported into JNUBEAM, which simulates the remaining part of the beamline. JNUBEAM uses GCALOR to simulate hadron interactions within the beamline. For oscillation analysis, these hadronic interactions are further tuned to the NA61/SHINE data[11] to obtain the expected neutrino flux.

For the purposes of the muon monitor simulation, only particles that pass through the Mumon detector planes are saved. This plane is represented by the volume $175\times175\times0.05$ cm^3 located at both the SI array and the IC array positions in the beamline. The simulations analyzed in this thesis only utilize the SI array since it is used as the primary sensor in mumon.

4.1.1 FLUKA Simulation

The simulation uses protons with a momentum of 30.9328 GeV/c are generated at the entrance to the baffle with beam position, beam angle, beam width and Twiss parameters defined by the user. In the case of the muon monitor simulation, Twiss parameters α_x=0.00, α_y=-0.12, emit$_x$=4.55π mm mrad, and emit$_y$=3.75π mm mrad measured in Run 11 were used. The effect on the simulation results from changing the Twiss parameters based on different Runs is generally small, and this is discussed in Sec. 5.2.

Twiss parameters are used to describe the properties of particles of a beam in phase space. This is described by an ellipse (fig. 4.1) described by the equation:

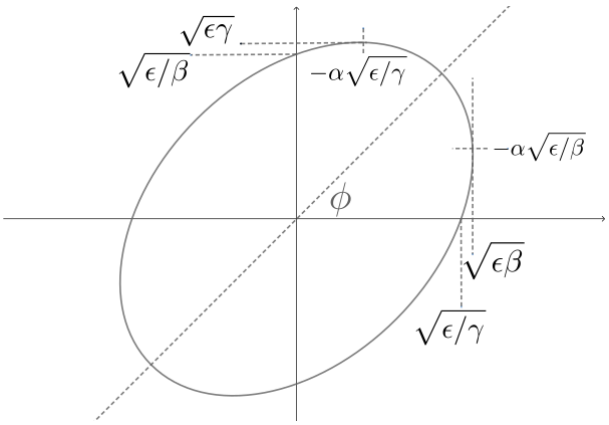

Figure 4.1: Ellipse formed from Twiss parameters shown in a phase space diagram

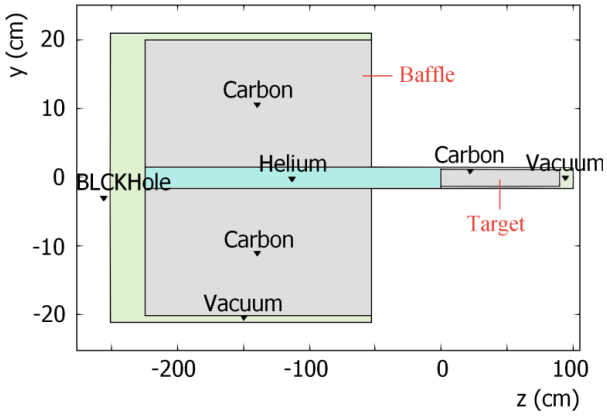

Figure 4.2: Fluka geometry y-z cross section

$$\gamma x^2 + 2\alpha x x' + \beta x'^2 = \epsilon \tag{4.1}$$

where x and x' are the position and velocity of the particle along a chosen axis, γ, α, and β are the Twiss parameters describing the ellipse and ϵ is the emittance of the beam, or in other words, the phase space area of the beam. This can be further parameterized such that

$$\alpha^2 = \beta\gamma - 1 \tag{4.2}$$

so for FLUKA inputs, only emittance and α are required for both x and y.

The baffle in the FLUKA geometry is represented as a graphite rectangular block that is $29 \times 40 \times 171.145$ cm^3. A cylindrical hole filled with helium is created in the baffle which is 3 cm in diameter. A drawing of the fluka geometry is shown in fig. 4.2

Only the graphite core of the target is simulated in FLUKA, represented by a graphite cylinder that is 2.6 cm in diameter and 90 cm in length. The rest of the target is simulated in JNUBEAM. The remaining space between the target and baffle is filled with helium gas, as it is in the target station. Once a particle exits this simulated region, its information is stored and then used by JNUBEAM. Electrons and photons below 1 GeV energy are cut to reduce file size.

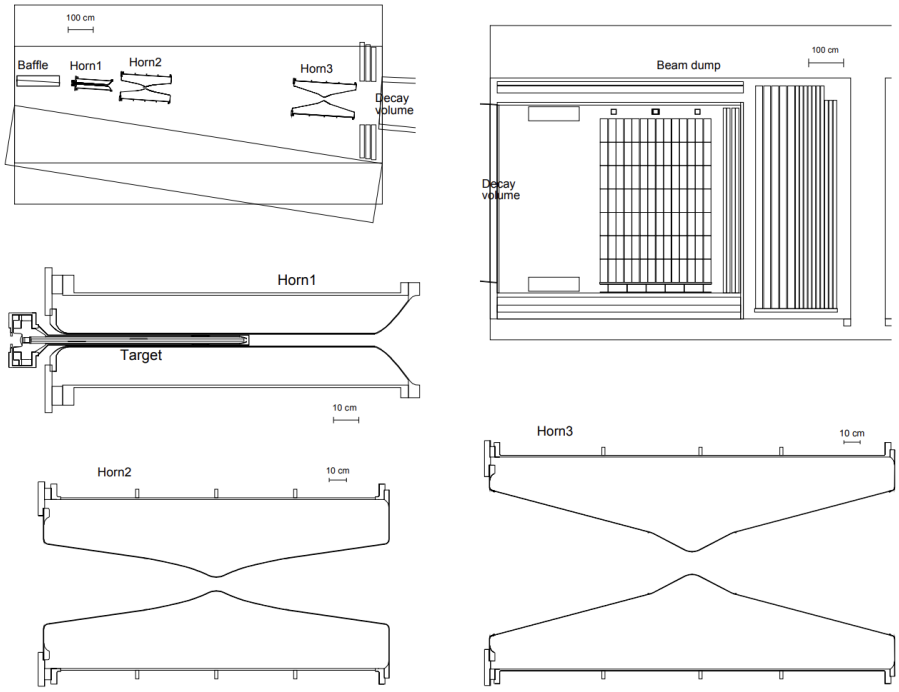

Figure 4.3: Jnubeam geometry shown for target station (top left), beam dump (top right), and cross sections of the horns/target (lower).

4.1.2 Particle Tracking in JNUBEAM

Particles are imported to JNUBEAM using the information stored by the FLUKA simulation. For the purposes of the muon monitor simulations, a more precise tracking threshold is defined as 0.05 GeV for hadrons, 5 MeV for Muons, and 0.5 GeV for electrons and gamma rays. In and after beam dump, a cut of 0.01 MeV is used instead. Drawings of important jnubeam geometry is shown in fig. 4.3.

The horn magnetic field in JNUBEAM is simulated between the inner and outer conductors according to Ampere's Law. With the assumption that the horn current flows uniformly in the conductors, the magnetic field at a distance r from the detector is:

$$B(r) = \frac{\mu_0 I}{2\pi r} \frac{r^2 - a^2}{b^2 - a^2} \tag{4.3}$$

where I is the current, a is the inner radius and b is the outer radius of the inner conductor, and μ_0 is the magnetic permeability.

For the purposes of muon monitor simulations an exact current of 250.0 kA and 320.0 kA is applied rather than the measured values. The muon monitor output is sensitive to the horn current, so using the same horn current values for the different simulations is required for reproducibility.

Since the vast majority of particles pass through the internals of the horns, interactions with the cooling water can create effects in the beam. So in addition to the static geometry of the baffle, target, horns, beam dump, and muon monitor cage, the cooling water for the horns is simulated by JNUBEAM. This includes the striplines, jets, and water internal to the horns. For

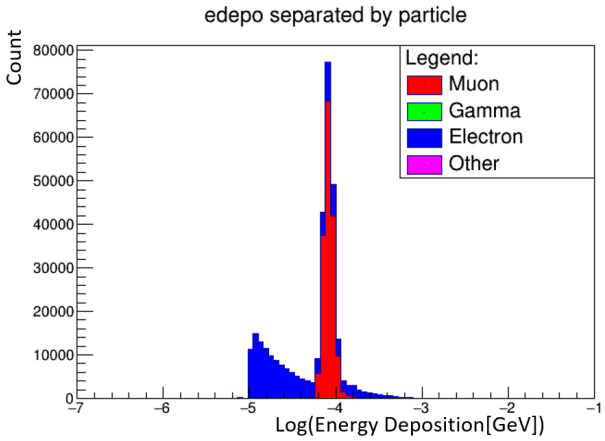

Figure 4.4: Energy Deposition in the mumon SI plane separated by particle. Muons have a sharp peak due to their constant energy deposition, while edepo from electrons is generally much lower. Gamma was also included, the relevant count is much smaller than that of electrons and muons.

the purposes of the muon monitor simulation, the water in horn 1, and the striplines in horn 2 & 3 were simulated.

It is important to note that many low energy electrons that ordinarily affect the muon monitor's output are below the energy cutoff and are not simulated in JNUBEAM. Additionally, not all of the geometry in the mumon pit, notably the many coolant pipes for the beam dump are not simulated. This as well as the moving stage for the reference silicon are known to have minor effects on the mumon profile that are not accounted for in the simulation.

4.2 Particle Momentum and Energy Deposition in the Muon Monitor

To get an estimation of charge deposition in the mumon sensors in the simulation, the energy deposition variable in Geant3 was used. As seen in fig. 4.4, gamma rays contribute very little to the overall energy deposited in the mumon plane. As a result, all gamma ray particles are cut from the fits on the simulated muon monitor flux.

Nearly all electrons in the muon plane are knock-off δ-rays from muon collisions with materials in the muon monitor chamber/detection plane and walls. Due to this, the electron profile in the muon monitor is mostly the same as that of the muons. The δ-ray electrons are treated as secondary particles of the muon within the same track, and have the same parent particles as the muon that created them.

Fig. 4.5 shows the momentum separated by particle. The high energy sector is dominated by muon flux, with very few high energy electrons. lower energies are dominated by electrons and gamma rays. The sharp cutoff in the electrons is due to the cutoff momentum for electrons in JNUBEAM at 0.1 MeV.

Fig. 4.6 Shows the energy deposition dependence on particle momentum. Electrons roughly follow a power law of $E_{\text{depo}} \propto p_e^2$ until $\sim$1 MeV, where there is a more scattered distribution with the highest count at 0.1 MeV energy deposited. Most gamma rays follow a roughly linear dependence, but do not contribute very much to the overall distribution as seen in fig. 4.4. The low energy muons contribute slightly more to the energy deposition, but the vast majority

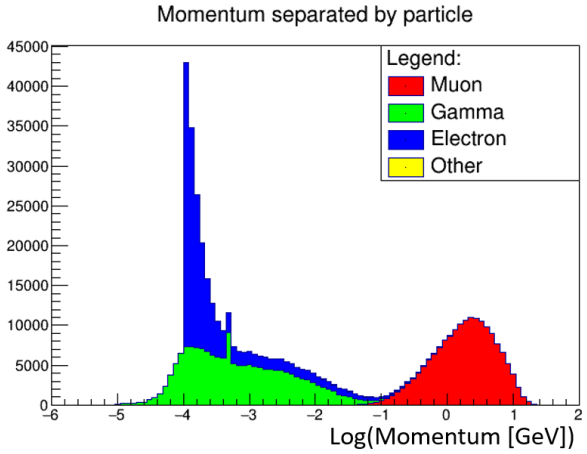

Figure 4.5: Momentum in the mumon plane separated by particle. A peak at the pair production energy is seen in the gamma ray distribution. The electron count increases as momentum decreases until the cutoff momentum in JNUBEAM. High momentums are dominated by muons with a peak near 3GeV.

follow a constant peak near 0.1 $\frac{\text{MeV}}{\text{Muon}}$. Electrons with momentum less than 0.1 MeV are not simulated as discussed above, which contributes to possible systematic uncertainties present in the simulation compared with the actual muon monitor. The total energy deposited in each bin in fig. 4.4 is equal to the bin's count multiplied with the bin's energy. As seen in fig. 4.5 the count of low energy electrons begins increasing drastically at lower energies, but they also are likely to continue following the power law of $E_{\text{depo}} \propto p_e^2$. As such, the contribution of these unsimulated low energy electrons is expected to be roughly similar to the simulated electrons.

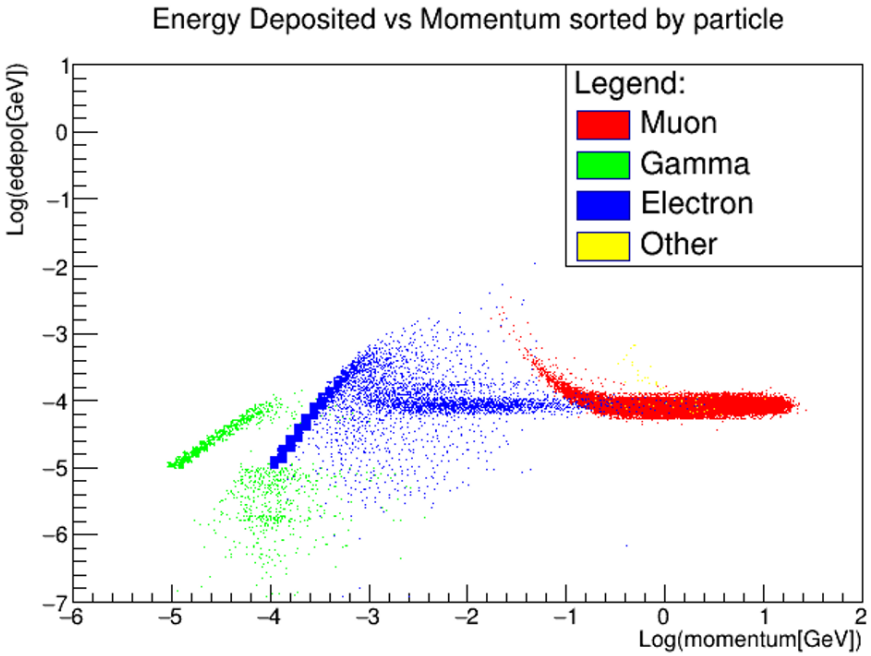

Figure 4.6: Log-Log 2D histogram separated by particle type. Gamma is generally much lower in terms of energy deposition, but has a linear dependence in the dominant region. Most electrons follow a proportionality of $E_{depo} \propto p^2$ up until ∼1MeV, where it becomes roughly constant. Muons have a higher Edepo tail at low momentum before it settles into the sharp peak we see at ∼0.1MeV/μ. The few other final state particles are mostly high momentum neutrons with an energy deposited of ∼0.1MeV.

Chapter 5

Parent Particle Origin Analysis

By separating the muon flux into components based on where the parent particle interacted in the beamline, it provides some insight into the dynamics of the proton beam inside the secondary beamline. The parent particles of the muon monitor final state particles are ∼88% pions, with the remaining fraction being mostly Kaons. This is consistent with the tertiary parent being a proton from the beam impacting with various components in the beamline. By separating the particles along the beam axis position, contributions to the muon flux from the proton beam impacting secondary beamline components can be extracted.

The ratio of parent particle types is consistent between target origin and beam dump origin parent particles as seen in table 5.1. Subsequently, it can be concluded that the impact of the proton beam on the beam dump is the origin of the majority of beam dump parent particles. The main difference is the fraction of kaons, which likely is due to many of the target origin kaons decaying further upstream than the pions, leading to a smaller number of the resulting daughter particles contributing to the resulting mumon profile.

As seen in fig. 5.1, the most dominant contributions to the muon profile come from the target, making up a wider gaussian component, with beam dump origin particles making up a thinner gaussian sitting on top of the wider component. This second component corresponds to the proton beam impacting the beam dump. In addition to pions and charged Kaons, there are also some minor contributions from neutrons(∼3%), protons(∼0.2%), and neutral Kaons (∼0.5%), along with smaller contributions from deuterons and alpha particles in the flux from the beam dump. The final state muon monitor particles are also affected slightly, with target origin parent particles, there is virtually only gamma, electron, and muons in the final state, while the flux from the beam dump has roughly the same proportions of these three dominant components as the target origin flux, but also includes ∼2.1% of the simulated sample being neutrons, along with negligible contributions from pions, kaons, protons, and other baryonic remnants.

The energy peak of the surviving muon flux is also shifted slightly towards lower energies compared to the target origin parent particles as seen in fig. 5.2. Since the energy deposition of muons is roughly constant at the relevant energies (fig. 4.6), it is unlikely that this affects the muon monitor's output in a meaningful way.

Other than just target origin and beam dump origin flux, the minor contributions of note are the horns, the baffle, and contributions along the decay volume. Horn 1 follows a similar profile to the target gaussian, as might be expected due to the position along the beamline. Horns 2&3 have a very small contribution at all beam positions (completely negligible in horn current on

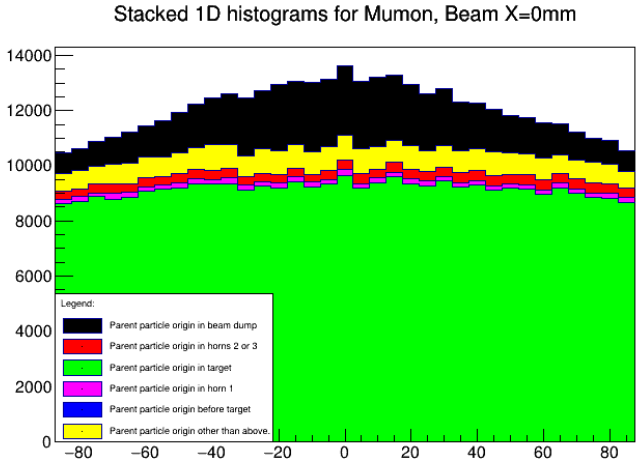

Figure 5.1: Stacked histogram of the measured mumon profile with 0kA horn current in simulation separated by parent particle creation position. The most important features are the thin beam dump origin gaussian sitting on the much wider target origin gaussian.

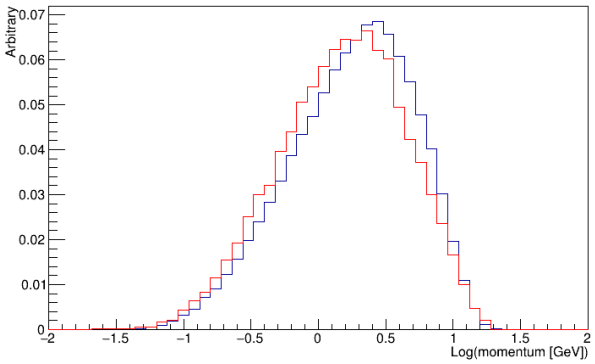

Figure 5.2: Muon momentum from target origin parent particles(blue) and beam dump origin parent particles(red). Both distributions are normalized.

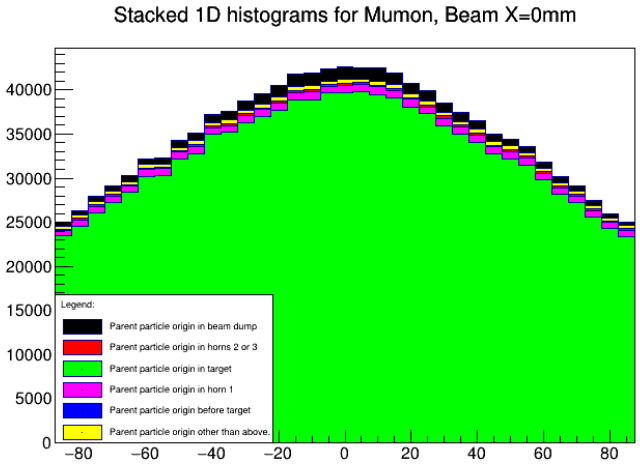

Figure 5.3: Stacked histogram of the measured mumon profile with 320kA horn current in simulation separated by parent particle creasion position. With the focusing effects of the horns, the gaussian resulting from the target origin parent particles is focused and the relative size of the beam dump origin thin gaussian is much smaller compared to the 0kA case.

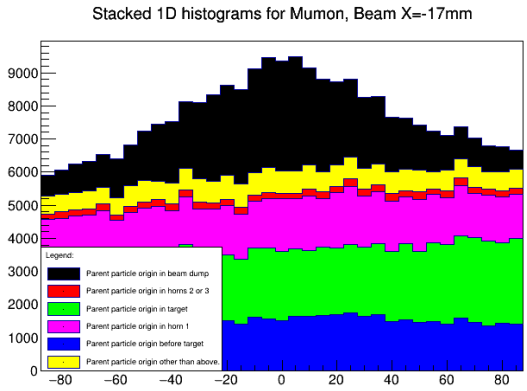

Figure 5.4: Stacked histogram of the mumon profile in JNUBEAM with 0kA at beam position of X=-17mm. A large contribution of horn 1 and baffle parent particles is observed

case), but also contributes to the wider gaussian profile. At large beam position offsets, when the beam begins hitting the baffle, this part becomes a dominant background to the target and horn 1 contributions (fig. 5.4). When the focusing horns are on (fig. 5.3, the parent particles resulting from the beam dump make up a small, constant background for the muon monitor measurement. For normal operation, this contribution is small enough to be ignored.

5.1 Analysis of Double Gaussian Beam Profile

If it is possible to extract the proton beam direction from the muon monitor using the beam dump origin flux, it could put additional constraints on the uncertainty of the neutrino flux arising from the proton beam direction. Additionally, it may explain the possible disagreement between INGRID measurements of the neutrino beam profile and muon monitor measurements of the muon beam profile.

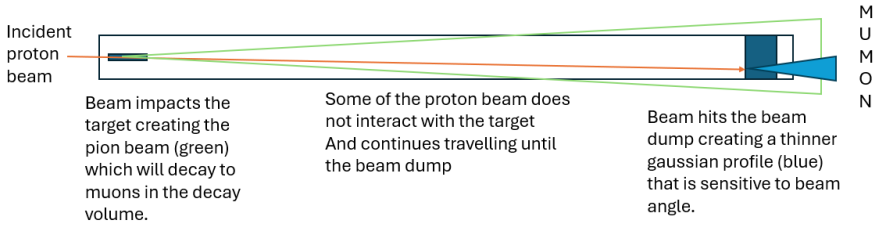

Figure 5.5: Mockup of the path of the residual proton beam to the beam dump.

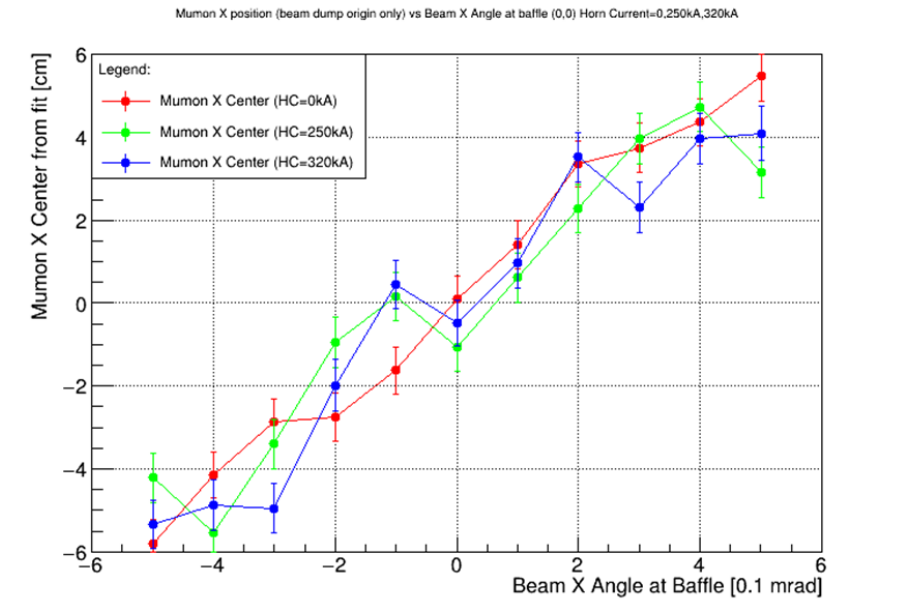

Figure 5.6: The angular dependence of the mumon profile with beam dump origin parent particles in simulation. Error bars only represent parameter error from the gaussian fit.

To separate the two components, the muon profiles are fit to a 2D double Gaussian (eqn. 5.1), with the parameters pretuned such that one Gaussian is 1/3 the size of the other in the 0 kA case.

$$\text{DGaus} = A \times Exp\left[-\left(\frac{(x-x_1)^2}{2\sigma_{x_1}^2} + \frac{(y-y_1)^2}{2\sigma_{y_1}^2}\right)\right] + B \times Exp\left[-\left(\frac{(x-x_2)^2}{2\sigma_{x_2}^2} + \frac{(y-y_2)^2}{2\sigma_{y_2}^2}\right)\right] \tag{5.1}$$

As seen in fig. 5.6, it was found that there is a horn current independent linear relationship between the center of the gaussian profile resulting from the beam dump origin parent particles and the beam angle in the simulation. The decay volume is 96m long, so for a proton beam angle of 0.1 mrad, the center of the gaussian resulting from the proton beam impacting the beam dump is 96 m $\times \tan(0.1\text{mrad}) = 0.96$ cm$\approx$1 cm offset in mumon, which is consistent to the level of offset seen in the simulation shown in fig. 5.6.

Figure 5.7 shows the stacked histograms made using the parent particle creation position in the simulation and the results of the two dimensional double gaussian fit for the 0 kA case. The fit was sufficient at separating the two components, consistently fitting the larger gaussian

Particle type	Beam dump origin	Target origin
π	79.3%	88.32%
K	16.66%	9.77%
neutron	3.2%	0%
other	0.84%	1.91%

Table 5.1: Parent particle type separated by parent particle creation position in JNUBEAM simulation.

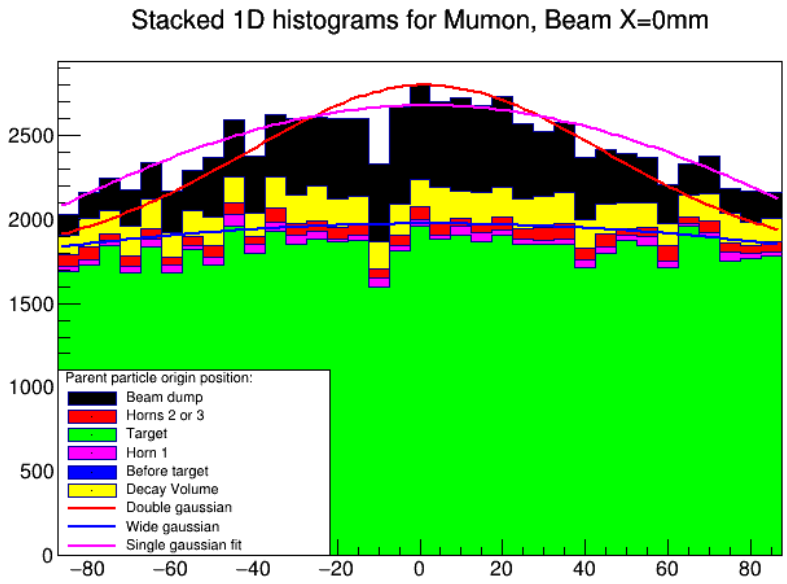

Figure 5.7: Stacked histogram with the x projection of the fits shown for nominal beam position and angle at a horn current of 0kA. The wide gaussian component is in blue, and the whole double gaussian is red. The single gaussian fit is shown in magenta.

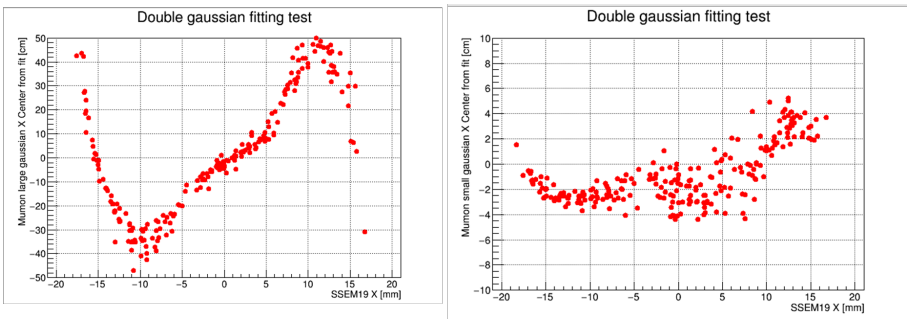

Figure 5.8: Run 13 position scan at 0kA fitted with the double gaussian. The wide gaussian center resulting from the target, horn 1, and baffle parent particles (left), and thin gaussian center resulting from the beam hitting the beam dump (right)

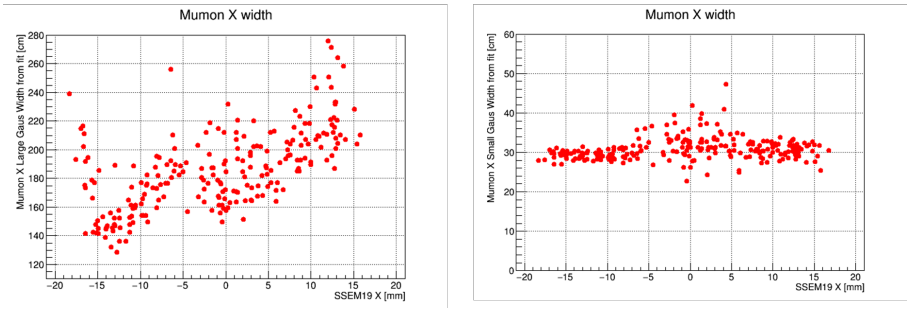

Figure 5.9: Run 13 position scan at 0kA fitted with the double gaussian. The wide gaussian width resulting from the target, horn 1, and baffle parent particles (left), and thin gaussian width resulting from the beam hitting the beam dump (right)

to the target parent particles, while fitting the thinner gaussian to the beam dump parent particles. The fit generally underestimates the actual width of the thin gaussian by around 15 cm, resulting in some disagreement in the fit towards the edge of the profile in the muon monitor.

In the 320 kA and 250 kA case, the fit was not successful due to the much lower ratio of the beam dump origin gaussian compared to the target origin gaussian. This means a spill by spill determination of the proton beam angle using a double gaussian fit of the physics Run mumon data is not possible, however, for the 0 kA horn current data present in the beam study data, this determination can be made. Due to only 49 sensors sparcely spaced and ten parameters involved in the fit, there are large errors on the fitted means of the beam dump gaussian from the fitting algorithm corresponding to a systematic error of $\sim \pm 8$ cm or $\sim \pm 0.7$ mrad.

In fig. 5.8 and fig. 5.9 the position scans (more info in Chapter 6) in Run 13 were fitted to eqn. 5.1. A clear separation is seen in the width between the wide and thin gaussian components, and the values are similar to that expected from simulation. As a result, it can be concluded that the fit is able to separate the two components in the low intensity 0 kA position scan successfully, and the beam dump origin gaussian center's correlation to beam position is similar to that expected from simulation(fig. 5.10).

The proton beam angle scan is a good test of the response of the beam dump gaussian since it should have a dependence on the proton beam angle of $\sim 1 \frac{\text{cm}}{\text{mrad}}$. Fig. 5.11 shows the resulting beam dump origin gaussian in the x angle scan. When fitted with a line, it has a slope of 11.6 ± 3.4 $\frac{\text{cm}}{\text{mrad}}$, and a Y-intercept of 0.8 ± 1.0 cm which is consistent to the expected response.

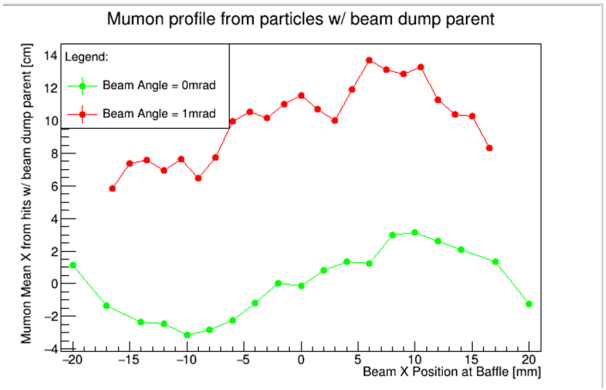

Figure 5.10: Simulated beam dump origin parent particle separated gaussian fit center compared with beam center position at the baffle. A large angle of 1mrad is applied to one simulation set to determine the effect of a large angle on the beam dump origin gaussian in a position scan scenario.

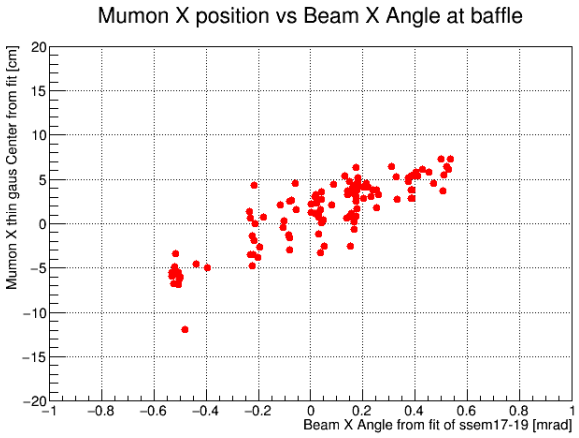

Figure 5.11: X angle scan in Run 13 at 0kA fitted with the double gaussian. Only the thin gaussian center resulting from the beam impacting the beam dump is plotted.

As mentioned before, the fit is not successful on 250 kA and 320 kA data since the beam dump gaussian is much smaller than the target gaussian compared to the 0 kA case. The double gaussian fit was successful at extracting the beam dump gaussian in the 0kA case, and extracts the expected beam angle response as seen in fig. 5.11. The point by point uncertainty of the fit parameters is large, namely an uncertainty of $\sim \pm 8$ cm or a corresponding $\sim \pm 0.7$ mrad proton beam angle, which means a point by point determination of the proton beam angle is unreliable.

Chapter 6

Beam Studies Using the Muon Monitor

6.1 Beam position Scan

As a part of the beam tuning process, after a long shutdown of the accelerator, a beam position scan is carried out to ensure normal operation of the accelerator and sensors in the secondary beamline. This is done by moving the beam between roughly -20 mm to +20 mm in both x and y (defined as the axes perpendicular to the beam direction z), with as close to no beam angle as reasonably possible and the horn current off. Datapoints close to 0,0 are then repeated with horn current on to attempt to find the center of the target by finding the point at which the muon monitor's response does not change between horn current on and off, also called the crossing point. The expectation of the muon monitor response is determined from simulations, the results are shown in fig. 6.1.

By observing the correlation between beam position and the response from the OTR and Muon Monitor detectors, we can obtain an understanding of the resulting neutrino beam direction's correlation with proton beam position, which is used to tune the beam for taking continuous data.

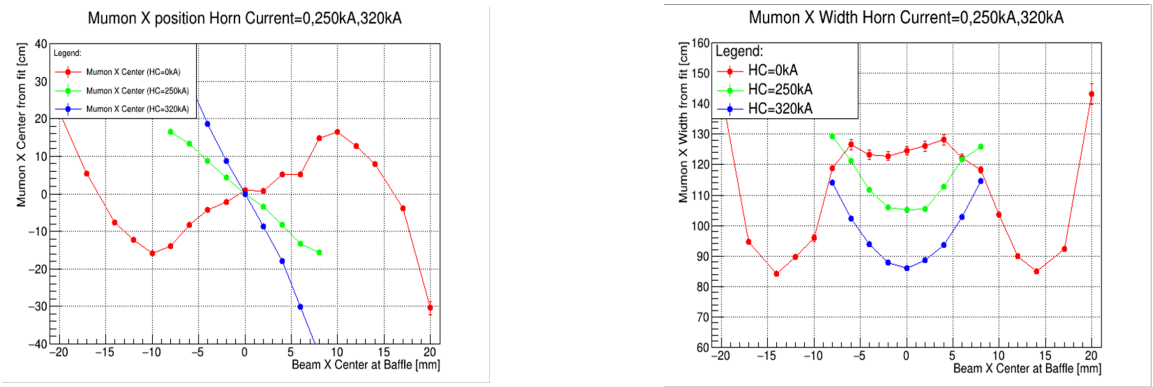

Figure 6.1: Simulated horizontal proton beam position scan Mumon center(left) and Mumon width (right) with perfect alignment of secondary beamline components. The beam width was 3 mm at the baffle entrance.

In addition to beam tuning, the data from the OTR and muon monitor detectors can be used to check for beam component alignment, with the muon monitor in particular being sensitive to the baffle and target position and angle. This is checked using Monte Carlo simulations using test component positions covered in Sec. 7.

6.1.1 Methodology and Purpose of the Beam Position Scan

This thesis is primarily concerned with the beam position scan studies in Runs 12 and 13 (2023-2024). The magnet settings were changed between each set of 11 spills with 2 bunches in each spill. Each spill is plotted as one datapoint. The Run 12 position scan was carried out using 35 magnet settings with between -20 mm and +20 mm for X and 26 magnet settings between -25 mm and 17 mm in for Y. The magnet settings near the target center were reused for horn current on scans. Similarly Run 13 had a position scan conducted using 27 magnet settings between -19 mm and +19 mm for X and 28 magnet settings betweeen -20 mm and 15 mm for Y. Again, horn current on data was taken using the same magnet settings for points near the target center. Due to time constraints, 250 kA horn current data was limited to 3 magnet settings of 11 spills each.

The beam position was measured using SSEM19, the last beam monitor before the baffle, and the muon monitor's 2D Gaussian fit results were used to represent the muon profile. For positions where the beam does not impact the baffle (between -10mm to +10mm), the OTR monitor can be used in a 3 point fit along with SSEM18 and SSEM19 to estimate the beam angle. For the X axis only, we can also incorporate SSEM17 into the fit since the magnet between SSEM17 and SSEM18 is a Y-axis dipole magnet, and should not affect the x axis of the beam.

6.1.2 Beam Angle Systematic Effects

Beam angle additionally has an effect on the resulting muon profile, and can influence the results of the beam position scan. Since the bending magnets must be manually updated for each point, it is difficult to remove the bias of a beam angle completely, thus some bias from angle must be considered. The angle can be calculated in during beam studies using a linear fit between SSEM17, 18, and 19 for X, since the bending dipole between SSEM17 and SSEM18 is a vertical bending magnet and should only affect the Y angle of the beam. For Y, SSEM18 and SSEM19 are used as well as the OTR monitor located just downstream of the baffle. There is an offset between SSEM19 and OTR expected to be -4.5 mm. This is taken into account as a correction, and a linear fit is done to determine the angle using the slope of this fit. Using OTR for the fit unfortunately only works well when the beam is near the center, since when the beam hits the baffle, this cuts off part of the profile seen in OTR and biases the fit, and eventually, no fit can be achieved.

To test the effects of a constant beam angle on the results of a position scan, a simulation of the position scan was carried out using a constant large beam angle of 1 mrad applied to all test beam positions. The simulation results are shown in fig. 6.2 and fig. 6.3 and show a clear shift in the position scan plot and a large asymmetry in the width scan plot. Understanding the effect of beam angle is important when considering the overall asymmetry observed in the position scans and attempting to ascertain the beamline alignment of components considering this set of simulations. In the case of a constant beam angle, or a dependency of the beam angle on the beam position during the scan, a bias is introduced as a result. As mentioned before, although a three point fit of the beam angle is possible in X for all beam positions, in Y, the

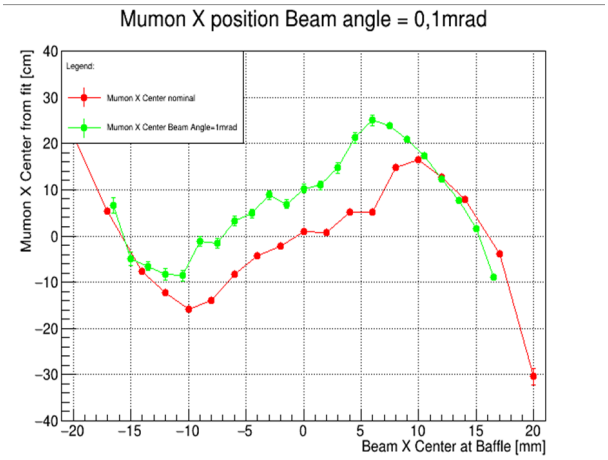

Figure 6.2: Simulated position scan with a constant large beam angle of +1 mrad compared to nominal.

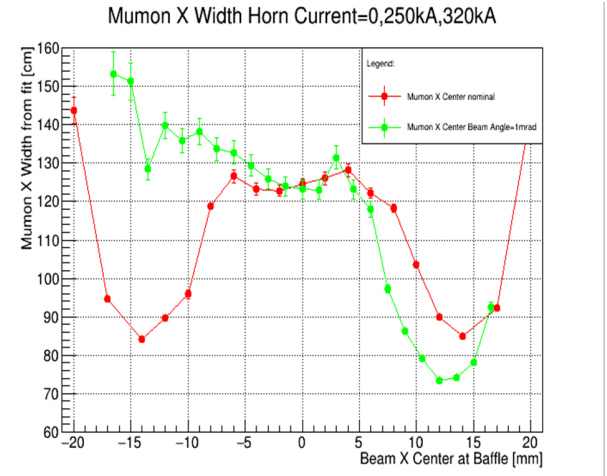

Figure 6.3: Simulated position scan Mumon X width with a constant large angle of +1 mrad compared to nominal.

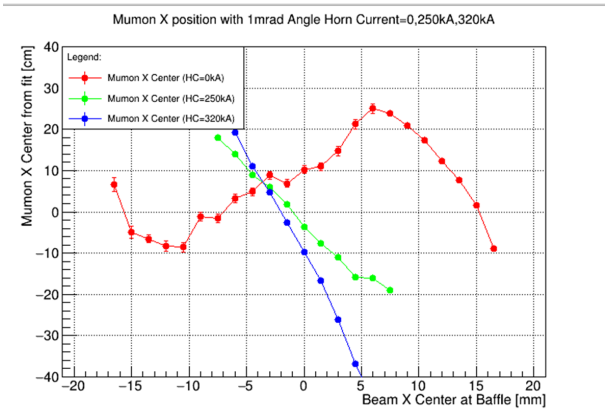

Figure 6.4: Position scan simulation with large angle of +1 mrad applied with the horn current on.

edges of the position scan, which are also the areas where the width asymmetry occurs that is sensitive to the misalignment of the target and baffle, thus, the more unreliable two point fit of the beam angle must be used to estimate the beam angle in these regions. More information on the effect of the beam angle on the position scan is discussed in section 5.

A large offset is seen in the position scan results opposite the direction of the beam angle. For small angles this shift is expected to be the shift of the beam center in the target plane, for the simulation, equal to $\sim$2.2 $\frac{\text{mm}}{\text{mrad}}$, proportional to the distance between the baffle and target. As seen by the shift of the maxima and minima for the large angle, as the beam angle becomes large, the magnitude of the shift becomes more dramatic. Additionally, towards the edges of the target and baffle, the effect of beam angle is not well studied. Width asymmetry is also created as the result of constant beam angle, as seen in fig. 6.3. A simple understanding of this is the effective size of the gap between the baffle and the target. For an angle of +1 mrad as seen here, if the beam center is at the edge of the baffle, it moves by $\sim$2.2 mm by the time it reaches the target, effectively removing the 2 mm gap between the baffle and the target.

The crossing point shift due to the beam angle is clearly seen in fig. 6.4, and the shift from the beam angle is the propagated position of the beam center in the target plane. There is no splitting in the intersections of the three lines due to beam angle.

The beamline coordinates used in the neutrino beamline and beamline monitors, including mumon, is rectangular with the Z axis aligned with the direction of the beam. Y is the vertical direction, and X is the horizontal direction. If you face in the direction of the beamline, in order to be a right handed coordinate system, the X axis would point to your left. The tilted beam axis of the secondary beamline is generally not applied as a transformation to the coordinates in order to preserve the Y axis as pointing towards the surface.

6.1.3 Features of the position scan correlation plots

The beam position scan correlation plots contain information pertaining to how the beam is scanned over the baffle and target, creating the shape of the correlation plot that is seen in fig.6.5 and fig. 6.6.

The main factor in the shape of the observed response in the muon monitor is the space between the edge of the target and the baffle. Near a beam position of zero, the beam is

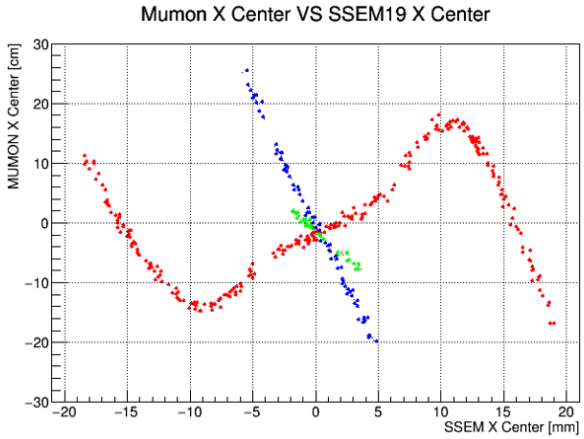

Figure 6.5: Run 13 X position scan comparing Mumon SI center to beam center in SSEM19. Horn currents are separated by color, red is 0 kA, green is 250 kA, and blue is 320 kA. Due to time constraints involved with the beam study time, only 3x11 data points were taken for horn current 250kA case.

perfectly on target, and should be aligned to 0 cm in the muon monitor center as well. As the beam moves away from zero, the optics of the target send the resulting beam away at an angle, reaching a peak as the beam reaches the edge of the target at around ±10 mm in beam position. Part of the beam then begins to miss the target and impact geometry further downstream, specifically in the beam dump, resulting in a drop in the observed width in the muon monitor. As the beam is moved further, the beam will also begin impacting the baffle (edge of the baffle is at ±15mm), creating a minimum in observed width in the muon monitor. As the beam hits the baffle, overall yield drops, while width increases, and the surviving particles that make it to the muon monitor are skewed to the opposite side.

The center of the beam position scan is important to understanding the normal operating conditions of the T2K beam. In particular, the intersection of the horn current on responses and horn current off response should correspond to the center of the target, which is the goal of beam tuning. Near the center there is a roughly linear response with the horn current off, which corresponds to the pion beam leaving the target being put out at a small angle (0.1mrad with 118m to mumon results in a center shift of 1.18cm of the muon beam). In the horn current on case, the focusing effect produces a much better linearity than the horn current off case. This is understood to be the result of the non-gaussian shape present in the horn current off state (discussed in greater detail in section 4&5).

Run 12 position scan results are shown in fig. 6.9. The outlier points seen are due to large beam angle during tuning, as seen in the angle calculated in fig. 6.10 by taking the linear fit of SSEM 17, 18, and 19 X centers.

To obtain the crossing point, or the point in the position scan where all three horn currents intersect, a linear fit was carried out on each of the horn currents. Due to the nonlinearities, the horn current off position scan was cut between -5 mm and 5 mm in SSEM19.

These results are calculated and reported in Table. 6.1, 6.2, and 6.3. There is a small shift from 0,0 seen in the position scan, contrary to what is expected in the nominal case. Since the

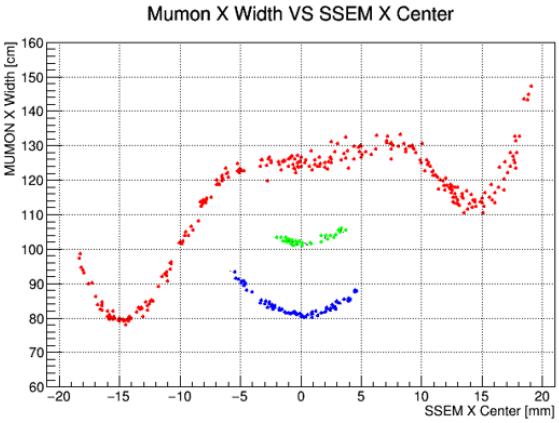

Figure 6.6: Run 13 Mumon SI width in the position scan compared with the beam center at SSEM19. Red is 0 kA, green is 250 kA, and blue is 320 kA.

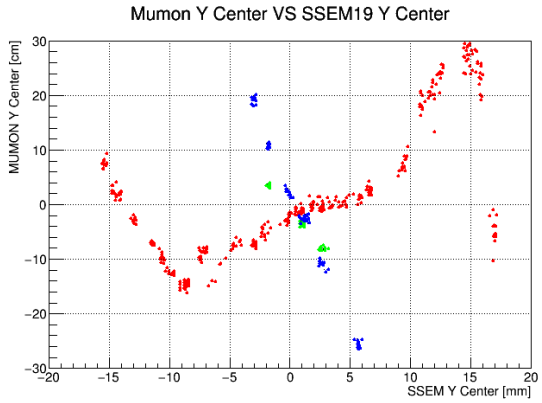

Figure 6.7: Run 13 Mumon SI Y center in the position scan compared with the beam Y center at SSEM19. Red is 0 kA, green is 250 kA, and blue is 320 kA.

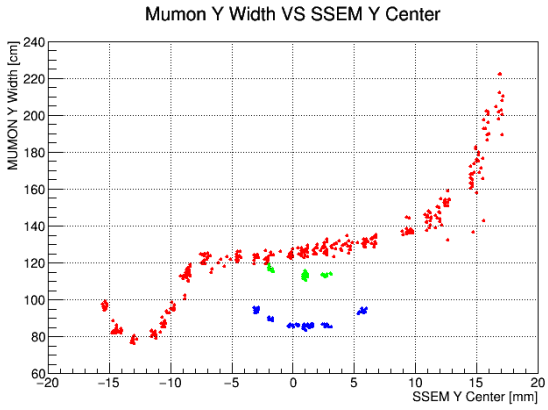

Figure 6.8: Run 13 Mumon SI Y Width in the position scan compared with the beam Y center at SSEM19. Red is 0 kA, green is 250 kA, and blue is 320 kA.

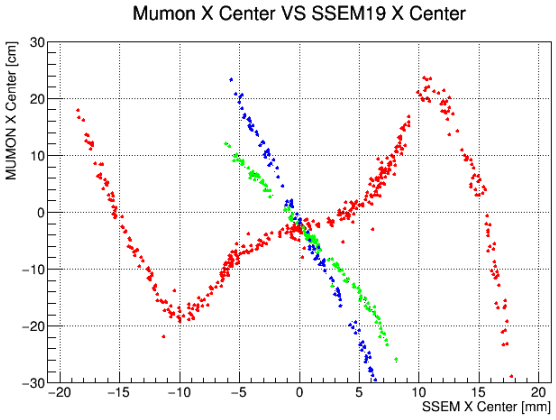

Figure 6.9: Run 12 mumon SI vs SSEM X center in X position scan. Red is 0 kA, green is 250 kA, and blue is 320 kA.

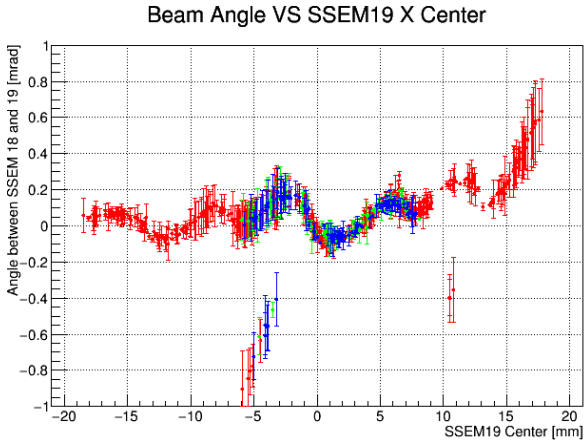

Figure 6.10: Run 12 X position scan beam angle calculated from SSEM17-19. Red is 0 kA, green is 250 kA, and blue is 320 kA.

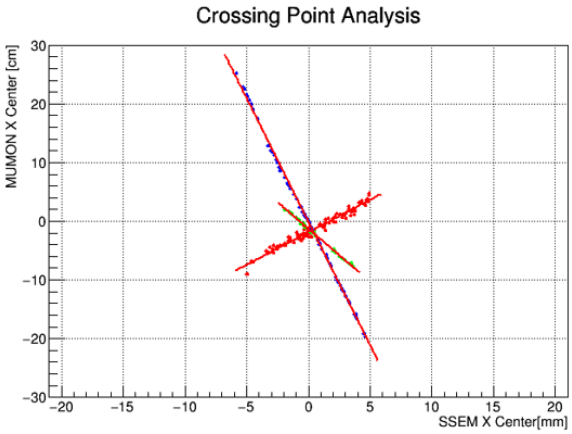

Figure 6.11: Fitting of the three horn currents in Run 13. In the case of 0kA horn current, it was cut between -5mm and 5mm to avoid nonlinearities. Red is 0 kA, green is 250 kA, and blue is 320 kA.

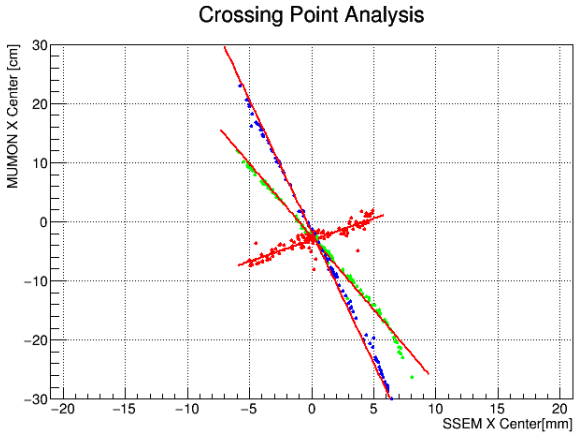

Figure 6.12: Fitting of the three horn currents in Run 12. In the case of 0kA horn current, it was cut between -5 mm and 5 mm to avoid nonlinearities. there is some deviation of 250kA horn current near the edges. Red is 0 kA, green is 250 kA, and blue is 320 kA.

Intersection	SSEM19 X center(mm)	Mumon X center(cm)
0kA & 320kA	0.33±0.01	-1.50±0.06
0kA & 250kA	0.20±0.02	-1.65±0.06
250kA & 320kA	0.49±0.02	-2.16±0.03

Table 6.1: Intersection of the 3 lines from crossing point analysis in Run 13 x position scan. As seen in fig. 6.11, there is a small shift from zero.

same magnet settings are used between the different horn current settings, if there is a beam angle present, this will introduce a systematic shift in all 3 horn currents, which would result in the observed crossing point being offset in this way.

In order to determine the angle present during the X position scan, a three point fit can be done using SSEM17, SSEM18, and SSEM19. Since the dipole magnet between SSEM17 and SSEM18 is a vertical bending dipole, the effect on the horizontal direction should be minimal, and thus a 3 point fit can be done in this way. OTR can also be used to determine the beam angle, however, since the OTR camera must be moved to capture all of the X position scan, and when the beam hits the baffle, OTR's position measurement is difficult to use after the camera is moved. As a result, OTR was only included in the fit for points betweeen -5mm and 5mm, since this is where the camera is in the nominal position, and there is no cutoff from the baffle. The results are shown in fig. 6.15. Near the horn current crossing point at zero, there is a positive beam angle of $\sim +0.1$ mrad. To produce the observed shift in the crossing point, a negative beam angle is required. Therefore beam angle can be ruled out as the cause for the observed shift in the crossing point in X.

Intersection	SSEM19 X center(mm)	Mumon X center(cm)
0kA & 320kA	0.27±0.04	-2.90±0.10
0kA & 250kA	0.17±0.04	-2.96±0.10
250kA & 320kA	0.42±0.10	-3.57±0.05

Table 6.2: Intersection of the 3 lines from crossing point analysis in Run 12 x position scan. As seen in fig. 6.12, there is a small shift from zero.

Intersection	SSEM19 Y center(mm)	Mumon Y center(cm)
0kA & 320kA	0.88±0.03	-1.74±0.10
0kA & 250kA	0.44±0.03	-2.10±0.11
250kA & 320kA	1.48±0.06	-4.73±0.03

Table 6.3: Intersection of the 3 lines from Y axis crossing point analysis in Run 13 y position scan. As seen in fig. 6.13, there is a small shift from zero.

Intersection	SSEM19 Y center(mm)	Mumon Y center(cm)
0kA & 320kA	1.12±0.05	-3.68±0.15
0kA & 250kA	0.81±0.05	-3.86±0.15
250kA & 320kA	2.01±0.22	-7.69±0.11

Table 6.4: Intersection of the 3 lines from Y axis crossing point analysis in Run 12 y position scan. As seen in fig. 6.14, there is a small shift from zero.

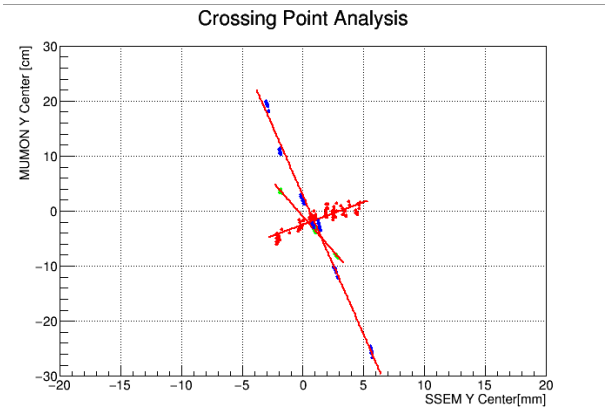

Figure 6.13: Fitting of the three horn current responses in Y. In the case of 0kA horn current, it is cut between -2.5mm and 5mm to ensure linearity. Red is 0 kA, green is 250 kA, and blue is 320 kA.

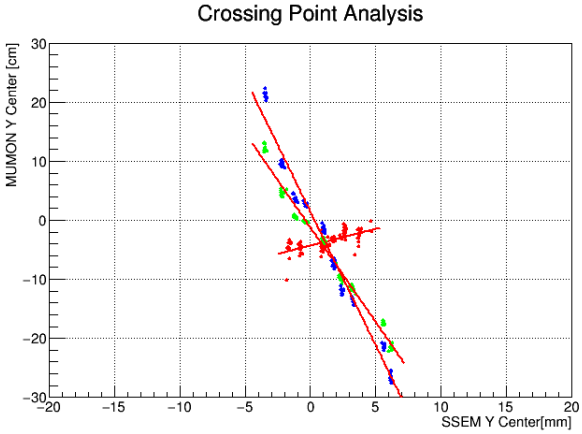

Figure 6.14: Linear fit of the three horn currents in the Y position scan in Run 12. The 0 kA data was cut between -2.5 mm and +5 mm to preserve linearity. Red is 0 kA, green is 250 kA, and blue is 320 kA.

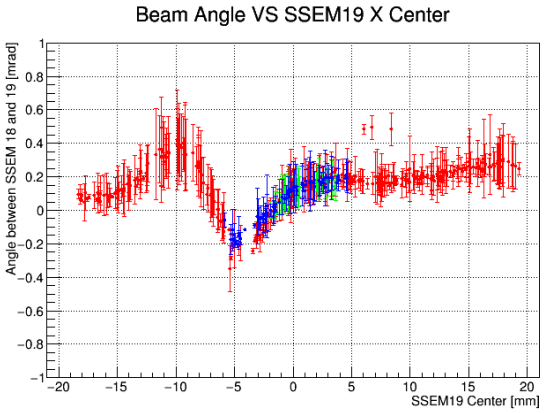

Figure 6.15: Fitted beam angle present during the Run 13 X position scan plotted in relation to SSEM19 X center. Error bars are only from the error on the fit. Red is 0 kA, green is 250 kA, and blue is 320 kA.

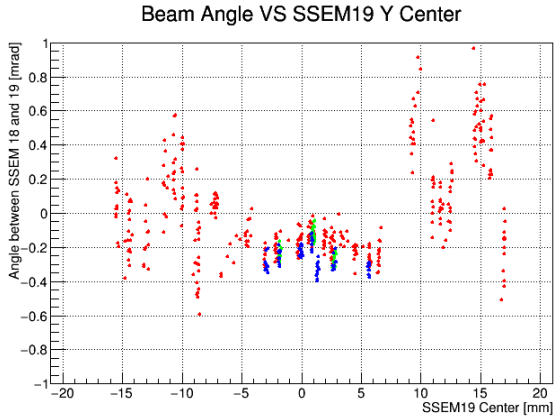

Figure 6.16: Fitted beam angle present during the Run 13 Y position scan plotted in relation to SSEM19 Y center. Error bars from fit are omitted to improve visibility, but are generally $\sim \pm 0.2$ mrad for points where OTR is usable between [-8,8], and a crude determination of the two point fit error from ssem centers is $\sim \pm 0.5$ mrad. Red is 0 kA, green is 250 kA, and blue is 320 kA.

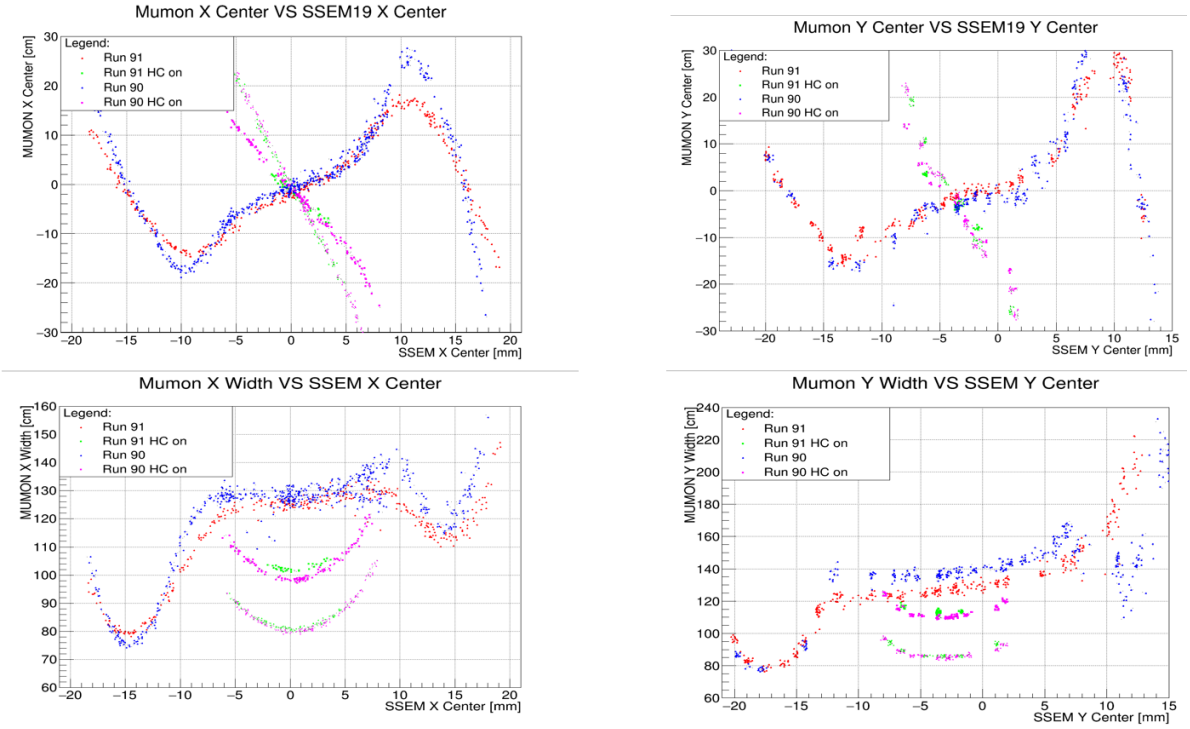

Figure 6.17: A comparison of Run 12 and 13 position scans. Blue is Run 12 with magenta as the horn current on, red is Run 13 with green as the horn current on. The Y position of SSEM19 sensor was not corrected for, so the center is shifted by -4.5mm.

For the Y position scan, the OTR camera does not need to be moved, so the range for the OTR included fit using SSEM18, SSEM19, and OTR is chosen to be [-8,8]. Outside this region, a two point determination of the angle is used with the difference between SSEM19 and SSEM18, this is known to be imprecise. The results are shown in fig. 6.16. Near zero, where the crossing point is located, an angle of ∼-0.2 mrad is observed. This is consistent with the expected direction of beam angle induced offset of the crossing point seen in the Y position scan (fig. 6.13 & table 6.3).

6.1.4 Differences between Position scans in Run 12 and Run 13

There are some differences observed between the position scans for Run 12 and 13 that were observed. Although the target station was opened during the summer maintenance period between Run 12 and 13, none of the beamline components were replaced or moved. It is important to understand the resulting differences to observe cases where beamline component alignment may have changed.

In addition to systematic differences discussed in the methodology of the position scan, such as a beam angle present during the scan, there are also some differences in the proton beam parameters that varies between Runs. To test the effect of changing the twiss parameters, a simulation of the position scan was done using the average twiss parameters from Run 11 and Run 13, using the geometry measured in the target station survey between Run 12 and 13. The reason Run 11 was chosen is because this study was also used to check the systematic differences in beam parameters used in the simulation set, which was generally Run 11. The beam width

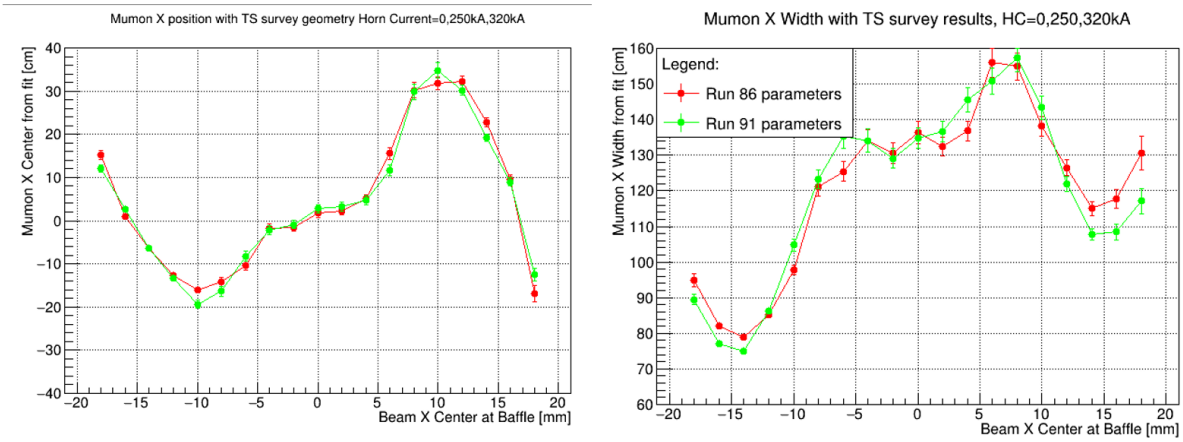

Figure 6.18: Differences in position scan simulation using target station survey geometry between T2K Run 11 (Main Ring Run 86) twiss parameters and T2K Run 13 (Main Ring Run 91) twiss parameters.

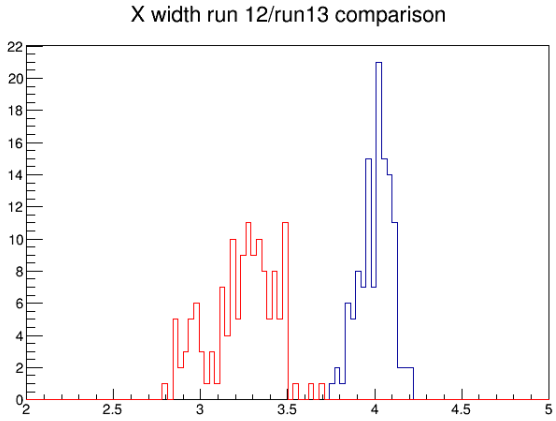

Figure 6.19: Beam width(mm) at SSEM19 during the X position scan in Run 12(red) and Run 13(blue). A similar trend was observed for the Y position scan.

was set to 3 mm for these simulations.

As seen in fig. 6.18, there is generally little difference in the position scan results changing the twiss parameters. There are some small differences observed in the width minima at +15 mm and -15 mm, with the Run 13 twiss parameters having lower minima by a few centimeters. This difference is important to keep in mind, however it cannot explain the differences between Run 12 and Run 13 position scans.

In addition to the Twiss parameters, a difference in the beam width during the position scan was observed between the position scan carried out in Run 12 and Run 13. The histograms of the beam width during each Run's position scan are shown in fig. 6.19. In Run 12, the width has a peak of ∼3.3mm and in Run 13, it has a peak width of ∼4mm. In order to determine the effect of this difference in beam width, a simulation was carried out with one set to 3 mm beam width and another set to 4 mm. It should be noted that the beam is created in the simulation at the entrance of the baffle, ∼1.2 m downstream of SSEM19. The beam width increases by the time it reaches the target, as a result, the effective width of the beam from the baffle is less

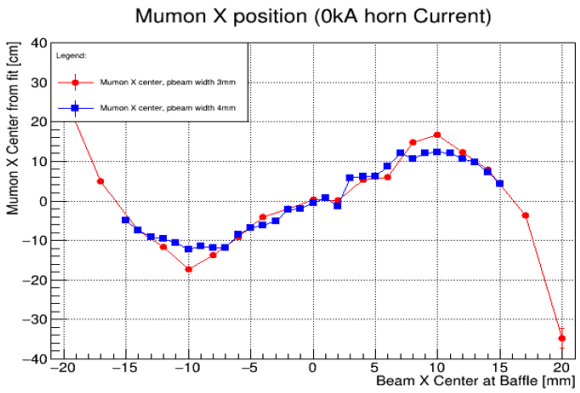

Figure 6.20: X position scan with nominal geometry and beam width set to 3mm (red) and 4mm (blue) respectively. The 4mm simulation dataset is spaced at 1mm and covers [-15mm,15mm], while the 3mm simulation dataset is spaced at 2mm between [-14mm,14mm], with ±17 and ±20 simulated to cover the edges.

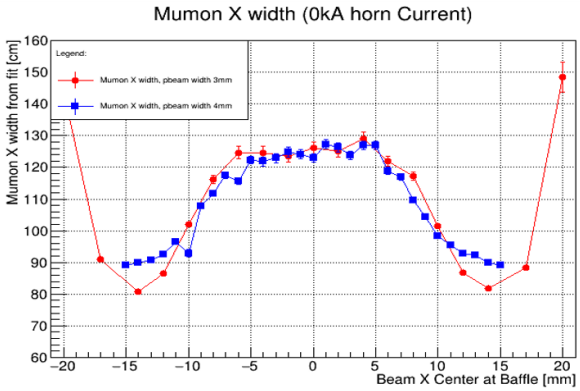

Figure 6.21: Simulated x width scan with nominal geometry and beam width set to 3mm (red) and 4mm (blue) respectively. The 4mm simulation dataset is spaced at 1mm and covers [-15mm,15mm], while the 3mm simulation dataset is spaced at 2mm between [-14mm,14mm], with ±17 and ±20 simulated to cover the edges.

than the effective width from SSEM19.

The effects of beam width can be well observed in fig. 6.20 and 6.21. At a wider beam width, the correlation plot between mumon center and SSEM19 is observed to have lower peaks at ±10 mm compared to the 3 mm beam width. Additionally, the minima in the mumon width correlation plot are also less deep. This phenomenon of higher beam width effectively "flattening" the mumon response to the geometry present in the width scan is accepted to explain the differences in the position scan results between Run 12 and 13.

In the Y position scan, the width at large +Y in Run 13 did not show the signature dip present as expected in the region between the baffle and target. Increasing the beam width as discussed above does not necessarily explain the difference in this region. Instead, it is considered likely that a large beam angle was presesnt to create this asymmetry. In Fig. 6.16, a determination of the beam angle is shown for the Y position scan, in the high Y region, this is done only with SSEM18 and SSEM19. Subsequently, the error on this determined beam angle is quite

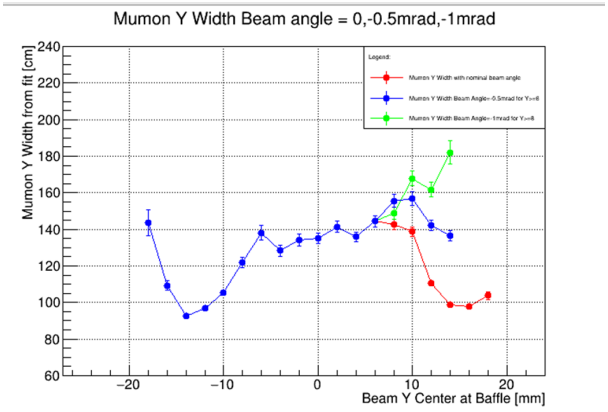

Figure 6.22: Simulated Y position scan Mumon width with angles of -0.5 mrad (blue) and -1 mrad (green) were simulated for 4 points between 8mm-14mm.

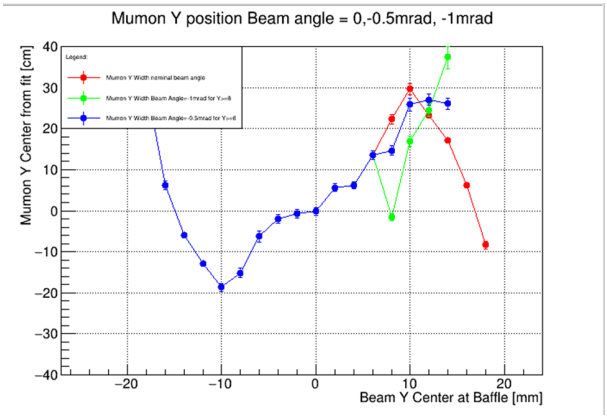

Figure 6.23: Simulated Y position scan Mumon center with angles of -0.5 mrad(blue) and -1 mrad (green) were simulated for 4 points beteween 8mm-14mm.

large, since the calculation of the beam angle only results from the difference between these two sensors. Unlike the X position scan, a good determination of the beam angle cannot be made outside the regions where OTR can be used for the three point fit. In order to test for a possible beam angle in this region, several simulations were run using the target station survey beamline geometry measured in the period between Run 12 & 13 using various possible beam angles for points at large +Y. The simulation results are shown in fig. 6.22 and fig. 6.23. It is shown that an angle of -1 mrad is able to create the lack of dip seen in the Y position scan. In fig. 6.23, there is a clear shift in the peak of the position scan towards a larger +Y beam center. It should be noted that although during simulation there is a large shift between the three possible angles, since the beam during the beam position scan is tuned for each datapoint manually, large jumps are rejected, and the angle is not constant between points like the simulation is, due to the magnet settings being changed between each set of points. As a result, it is more likely that the shift in the angle is more gradual than the sudden jump seen in the simulation.

If there is a shift in the position scan peak matching the simulation (fig. 6.23) present between the position scan done in Run 12 and Run 13, this large beam angle can be taken to explain the high +Y difference between the Run 12 and Run 13 Y position scans rather than a shift in the beamline geometry. In order to find the peak of the position scan, a quadratic fit is done over the region near the peak and the beam center position at the maximum of the fitted

function is extracted. In this way, the Run 12 maximum is found to be at 13.1 mm and the Run 13 maximum is found to be at 14.2 mm in SSEM19. This is a difference of ∼+1mm and is equivalent to a difference of ∼ -0.5mrad in the simulation. While this does not conclusively solve this discrepancy between the Run 12 and Run 13 position scans, it does indicate there has been a shift in the position scans at high +Y due to a negative beam angle.

6.2 Beam Angle Scan

A beam angle scan was carried out in Y during Run 12, and in X during Run 13. Similar to the beam position scan, the beam angle scan involves introducing a beam angle and observing the effects on the downstream sensors in OTR and MUMON. For the Mumon group, the purpose of the beam angle scan is to find the effects of the beam angle on the MUMON measurements and to verify beam tuning results.

The beam angle scan data allows for the separation of the effect from proton beam angle and proton beam position on the muon profile measured by the muon monitor. With the assumption that the beam angle effect and beam position on the target are independent effects, a general model is

$$\mathrm{MUSI}_{\mathrm{x,center}} = f(x_{\mathrm{target}}) + f(\theta_{x,\mathrm{beam}}) \tag{6.1}$$

x and y are expected to be similar. For a simple model, near the target center, it is expected that both beam position and beam angle follow an independent linear relationship to the muon profile center. In this case, the model becomes:

$$\mathrm{MUSI}_{\mathrm{x,center}} = m_{\mathrm{beampos}} \cdot x_{\mathrm{target}} + m_{\mathrm{beam\ angle}} \cdot \theta_{x,\mathrm{beam}} + b_{\mathrm{offset}} \tag{6.2}$$

If the muon monitor response is well understood, then the position scan can be used to find misalignments of beam monitors and secondary beamline component alignments using the beam position scan.

6.2.1 X Angle Scan

The angle during the beam angle scan can be calculated by using a linear fit between the positions of SSEM18, SSEM19, and OTR. Additionally, in X, since the magnet between SSEM17 and SSEM18 is a vertical dipole magnet, it is possible to include SSEM17 in the fit as well. In Run 13, since the OTR foil could not be changed to the low intensity foil, this SSEM only fit was used to obtain the angle for the X angle scan.

In a similar way to the position scan, a crossing point can be found between the three horn current settings. Similarly to the position scan, there should exist a point where changing the horn current setting has no effect on the response in mumon. This ideally exists at 0mrad, since if the beam is properly centered on the target, and there is no beam angle, horn current should have no net shift to the beam center.

The crossing points can be calculated from the fitted lines using Equation 5.1. The values are reported in Table 6.5. Similar to the X position scan, there is a deviation of the crossing point from zero. Since the beam position cannot be perfectly set during the angle scan, small deviations from 0,0 in target space can occur, skewing the results slightly.

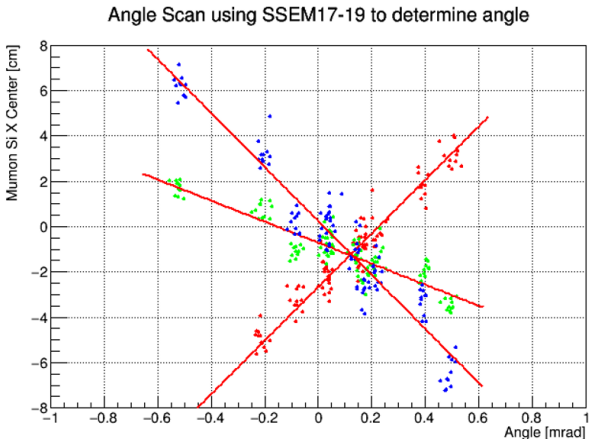

Figure 6.24: The X angle scan from Run 13. Each of the horn currents are fitted with a line, and the crossing point is identified. Red is 0 kA, green is 250 kA, and blue is 320 kA.

Intersection	Beam angle (mrad)	Mumon X center (cm)
0kA & 320kA	0.12±0.02	-1.2±0.2
0kA & 250kA	0.12±0.02	-1.3±0.2
250kA & 320kA	0.13±0.06	-1.32±0.02

Table 6.5: Table of crossing point values for Run 13 X angle scan calculated from linear fits of the 3 horn current settings. The errors are the linear fit errors propagated through Eq. 5.1

To attempt to mitigate the possible effect of offcenter beam position during the angle scan, it is necessary to propagate the beam forward from the last measured position at SSEM19 to attempt to ascertain the position on the target. If the angle is propagated from SSEM19 X module, which sits 3175.656mm upstream of the target, 1mrad angle corresponds to 3.18mm on the target. By using the fitted beam angle, a position in target space can be derived by the equation below.

$$\text{Beam}_{x,\text{target}} = \text{SSEM19}_x + \theta_x \cdot 3.18 \frac{\text{mm}}{\text{mrad}} \tag{6.3}$$

Near the center of the target, beam angle and beam position are both linear, so a linear correction can be applied to the angle scan data based on the position on the target. This can be applied as a correction using position scan simulation data that is set to a perfectly 0 mrad angle beam (fig. 6.26). Then, a linear fit is done on each of the three horn currents near zero, where they are roughly linear to determine the expected response from the beam position, then subtract this from the mumon center in the angle scan to get the corrected position. Errors from both the fitted angle and simulation statistics are propagated to obtain the systematic error on the correction. The correction is applied by the equation:

$$\text{MUSI}_{x,i,\text{corrected}} = \text{MUSI}_{x,i} - (m_j \cdot \text{Beam}_{\text{x,target}} + \text{b}_\text{j}) \tag{6.4}$$

where each datapoint i is corrected by the linear equation for horn current j defined by the parameters m_j and b_j found from the position scan simulation fit. j represents one of the three horn current settings, such that $j = 0, 250, 320$ kA.

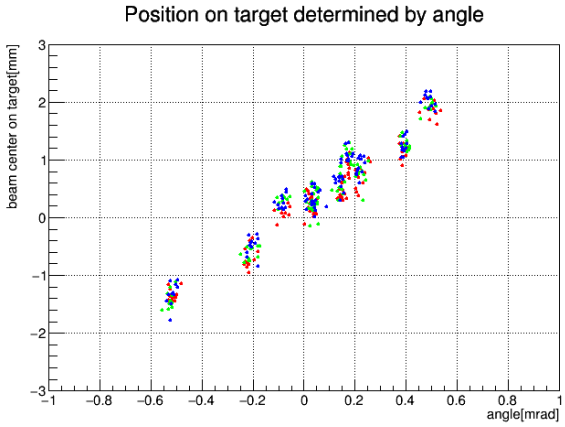

Figure 6.25: Position on the target propagated using the angle. Error bars are not included here for clarity, but there is a point by point fitting error of $\sim \pm 0.05$-0.15mrad angle error and a corresponding $\sim \pm 0.15$-0.45mm error in target space position. Red is 0 kA, green is 250 kA, and blue is 320 kA.

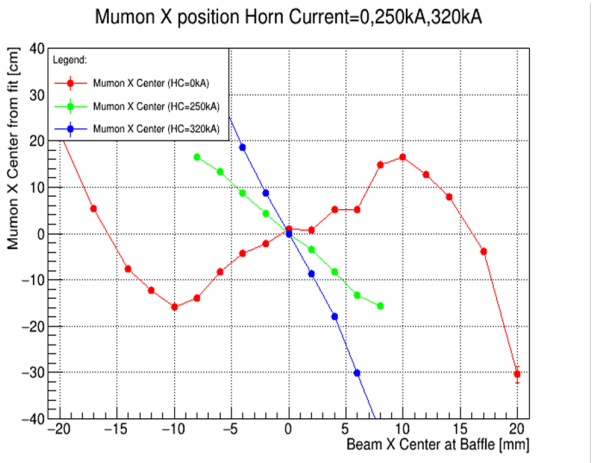

Figure 6.26: Beam position scan done with nominal beam parameters. The fitting region to obtain the equations is between -5 mm and 5 mm.

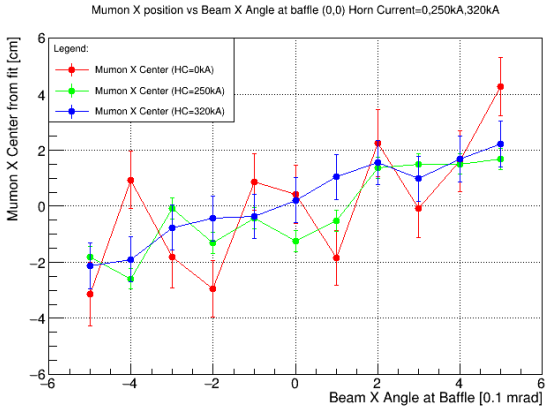

Figure 6.27: Nominal geometry beam angle scan with nominal geometry correction applied. Error bars are from mumon fitting uncertainty and correction uncertainty propagated together.

In the case of ideal beamline geometry, (see fig. 6.27), when the correction is applied, there is a clear horn current independent, linear relation seen between beam angle and Mumon X center. However, in the case of nonideal geometry, there may be asymmetries introduced to the beam angle scan. To attempt to replicate the geometry present during the X angle scan in Run 13, target scan survey data was used to carry out a simulated position scan using the measured values of the secondary beamline alignment in the target station. Then, the regions near zero beam position (between ± 5) were fitted to a line and used for corrections.

When the correction is applied to the beam angle scan, there is a clear separation of horn currents as a result. Interestingly, the 250kA horn current line is very close to that of the position corrected simulation. This offset between the paths can be taken to be the effect of the geometry on the Mumon response to beam angle. If this shift observed here reflects that of the position scan, we can calculate an equation for the expected Mumon SI X center as a function of SSEM19 x center and fitted beam angle by using the aforementioned simulated position scan linear fit equation in conjunction with the obtained angular relationship.

$$\mathrm{MUSI}_x = m_{\mathrm{sim}}(x_{\mathrm{SSEM19}} + \theta_{\mathrm{beam}} \times 3.18\frac{\mathrm{mm}}{\mathrm{mrad}}) + m_1\theta_{\mathrm{beam}} + b_1 \tag{6.5}$$

Where m_{sim} is the linear fit of the position scan simulation of the survey geometry with no beam angle, θ_{beam} is the beam angle in mrad, and m_1 and b_1 are the fitted linear response to beam angle. The angle is transformed into an position offset in target space by applying the factor of 3.18mm/mrad. Then, the intersection of two of these lines can be found to attempt to find the expected crossing point of the position scan, given the angle, which was analyzed earlier in Fig. 6.15 to be $\sim$0.1mrad near zero.

$$X_{\mathrm{cross(1,2),SSEM}} = \frac{b_2 - b_1 + \theta_{\mathrm{beam}}(3.18\frac{\mathrm{mm}}{\mathrm{mrad}}(m_{\mathrm{sim},2} - m_{\mathrm{sim},1}) + m_2 - m_1)}{m_{\mathrm{sim},1} - m_{\mathrm{sim},2}} \tag{6.6}$$

Where $X_{\mathrm{cross(1,2),SSEM}}$ represents the crossing point in the position scan of horn current 1 and horn current 2 in SSEM19 space. b_1 and b_2 are the angle scan fitted line's y intercept, which can be interpreted as the offset from the ideal geometrical case, representing either an offset from the beam monitors or from components in the secondary beamline. θ_{beam} is propagated into a position on the target. Additionally, the difference in angle dependence measured in the angle scan (m_1 and m_2) are taken into account. It should be noted, that in the case of ideal geometry as

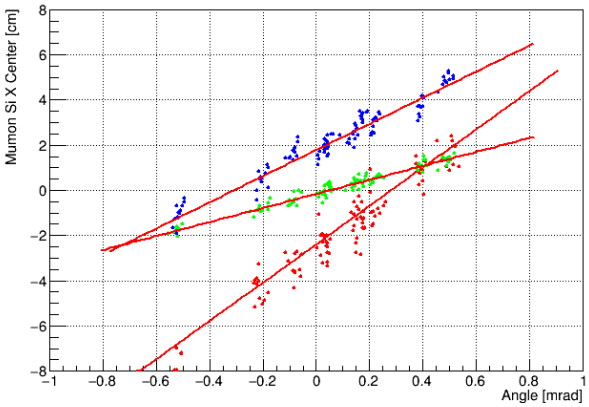

Figure 6.28: Position corrected beam angle scan, Run 13, each of the horn currents(red=0 kA, green=250 kA, blue=320 kA) was fitted to a line. Unlike ideal case seen in fig. 6.27, there is an offset between the three horn current lines seen in the angle scan.

seen in fig. 6.27 that $b_2 - b_1$ and $m_2 - m_1$ would vanish since there is no horn current dependence. In that case, the expected crossing point reduces to $X_{\text{cross(1,2),SSEM}} = -\theta_{\text{beam}} \times 3.18 \frac{\text{mm}}{\text{mrad}}$ or in other words, just the center of the target offset in the SSEM19 space from the angle. Again the difference of the simulated position scan slopes are divided similarly to Eq. 5.1.

If we choose 0kA and 320kA, as well as the values taken from this angle scan and survey geometry simulated position scan are taken into consideration, the equation becomes:

$$\begin{aligned} X_{\text{cross(1,2),SSEM}} &= \frac{4.17 + 0.1[\text{mrad}](3.18 \frac{\text{mm}}{\text{mrad}}(-6.46) - 2.7)}{6.46} \\ X_{\text{cross(1,2),SSEM}} &= 0.29\text{mm} \pm 0.35 \\ \text{MUSI}_{x,\text{cross}} &= -1.01\text{cm} \pm 0.91 \end{aligned} \tag{6.7}$$

The estimation of the uncertainties from the fits and beam angle are propagated through with the assumption that the parameters are independent. This is not necessarily true, especially since the beam angle was used in nearly every step of the fits, invariably there are correlations of these parameters to the chosen beam angle, particularly that of the intercepts given that a simple translation in the beam angle axis would result in the intercepts varying greatly. Nearly all of the uncertainty is due to the beam angle, namely since the equation depends a lot on the beam position in the target plane, which due to the relatively large baseline of 3.18m between SSEM19 and the target means that there is a larger error by a factor of $\sim$50$\times$ compared to the next highest contributor. Similarly, when the error is propagated through the equation for the MUSI crossing point, the error contribution of the angle is $\sim$10$\times$ larger than the next highest contribution.

While this method of estimation does not make any strong conclusions as to the exact crossing point (to constrain the quandrant to 2σ would require about twice as much precision on the measurement of angle), the predicted location of the crossing point is similar to that is observed in Run 13 position scan. While this method does not serve to explain the shift in the crossing point that was observed, it does demonstrate that an asymmetry in horn current dependence can create a shift in the crossing point, the possible origins of this dependence are investigated in Section 6.

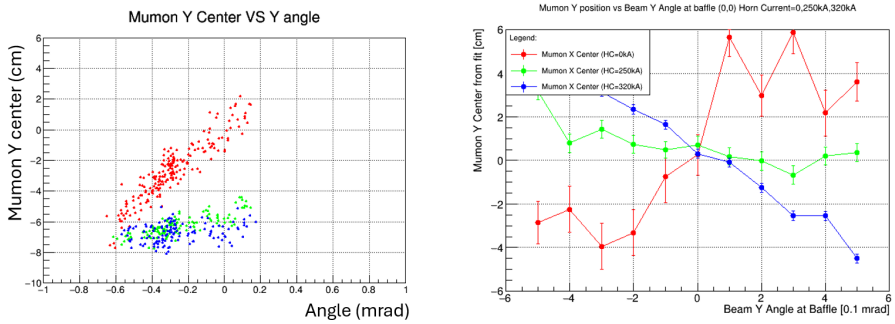

Figure 6.29: Run 12 Y angle scan(left) compared with nominal geometry simulated beam angle scan. Datapoint error bars are omitted for clarity, but are generally $\sim \pm 0.2$mrad error only considering the beam fit error. Red is 0 kA, green is 250 kA, and blue is 320 kA.

6.2.2 Y Angle Scan

During Run 12, a Y angle scan was also carried out. The Y angle scan is important since there are more systematic dependencies on the Y angle, since the beam axis is tilted 3.637 degrees downward such that it points towards SK(2.5 degrees off axis) through the Earth's curvature. Additionally, the structures seen in the Y position scans indicate that there is possible angle dependence that an angle scan may help illuminate.

To calculate the Y angle, a linear fit between SSEM18, SSEM19, and OTR is considered, and the angle is extracted from the slope of this fit. There is an expected offset of 4.5mm between the SSEM18 and SSEM19 center compared with the OTR center. This is corrected for in this result. Fig. 6.29 reports the results of the beam angle scan compared with a simulated angle scan using nominal geometry in FLUKA and JNUBEAM. It is clear that there is some systematic bias present in the beam angle scan that is skewing the results. The Horn current on case is expected to change the slope significantly compared to each other, and additionally, the crossing point determined is extremely skewed compared to the expected crossing point of zero.

As discussed in section 5.2.1, the beam angle scan is affected by the position of the beam in the target plane, as is seen during the position scan. To obtain the position in the target plane, the beam was propagated forwards from SSEM19 with the 4.5mm correction applied such that -4.5mm in the SSEM19 plane corresponds to 0mm in the target plane if there is no beam angle. The distance from the SSEM19 Y plane to the target is 3201.209mm, this corresponds to a factor of $3.201 \frac{\text{mm}}{\text{mrad}}$ Fig. 6.30 shows the beam angle scan in the target plane position. There is a clear offset in Y position compared to zero that would create an offset in the Y angle scan. similar to that seen above.

Similarly to the process with the x angle scan, a position correction can be applied to attempt to remove the effects of the position bias by subtracting the expected muon monitor Y center for that position derived from the position scan. A linear fit of the three horn currents near zero in the nominal geometry position scan was carried out, and the parameters were used to attempt to correct for the position bias. A simulation using nominal beamline geometry was done to provide a reference where angle and position on the target are well known. This is shown in fig. 6.31. There is a difference in the response of the three horn currents seen in the simulated muon monitor. Specifically, at 320kA, there should be very small dependence on beam angle due to the focusing horns effects successfully focusing the beam to be parallel to the beam axis.

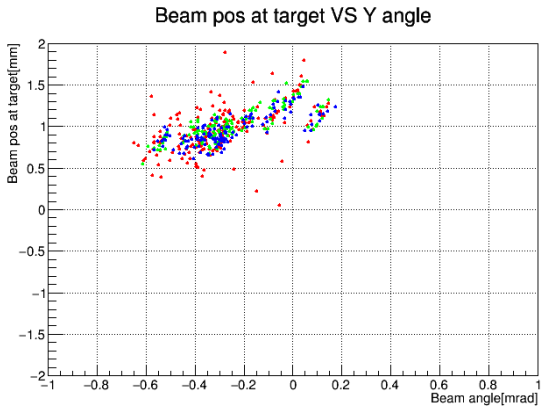

Figure 6.30: Y angle scan with the beam propagated from SSEM19 into the target plane. Red is 0 kA, green is 250 kA, and blue is 320 kA. The error bars are omitted for clarity. The uncertainties on the beam angle from the fit are $\sim \pm 0.2$mrad, and this translates to $\sim \pm 0.64$mm in target space. 0kA (red) appears to be more scattered since beam tuning during the run created outliers; there should be no significant horn current dependence on the reconstructed positions.

For other horn currents, there is a dependence in the muon monitor on the beam angle.

The results of the correction are shown in fig. 6.32. As expected from the simulated angle scan correction, 0kA and 250kA horn currents follow similar slopes that generally trend to the origin. The 320kA line also trends to the origin, but does not follow the expected lack of beam angle dependence seen in the simulated angle scan correction. Since the equation for the correction for a point i at 320kA is:

$$\mathrm{MUSI}_{y,i,\mathrm{corrected}} = \mathrm{MUSI}_{y,i} - \left(m_{320\mathrm{kA}} \times (Y_{\mathrm{SSEM19}} + 4.5\mathrm{mm} + \theta_{y,i} * 3.201 \frac{\mathrm{mm}}{\mathrm{mrad}}) + b_{320\mathrm{kA}}\right) \tag{6.8}$$

$m_{320\mathrm{kA}}$ is the slope of the fitted simulated position scan at 320kA, and $b_{320\mathrm{kA}}$ is the y-intercept. The offset of +4.5mm is applied. Since the above equation introduces an explicit dependence on beam angle ($m_{320\mathrm{kA}}$ is negative as seen in fig. 6.7), and in the initial data there was little dependence on beam angle, by introducing the correction, this applied a slope to the data that was not consistent with that of the simulated angle scan with the correction applied. This is likely due to differences between the simulated angle scan and the actual angle scan that introduced an angular dependence at 320kA or removed it in the simulation. This may be due to secondary beamline geometry, namely horn alignment, which may focus the beam in an asymmetric way depending on the beam angle.

In conclusion, the Run 12 beam angle scan was done with an offset position of $\sim$+1mm in the target plane, which caused the strange asymmetry of the scan compared to the expectation from simulation. This motivates a new beam angle scan to be done in the near future with better alignment to the target center. When Run 12 began, since SSEM19 was replaced in the shutdown between Run 11 and Run 12, the exact offset of SSEM19 Y compared to OTR and the target was not known exactly, and due to a fire at a J-PARC site magnet power supply, Run 12 was cut short, so it was not well studied until Run 13, where it was confirmed to be offset by -4.5mm. Due to this, the offset was not well known until after the beam angle

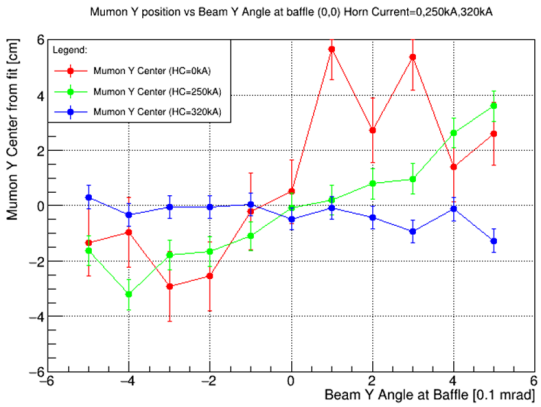

Figure 6.31: The nominal geometry beam angle scan with target position correction applied. Error bars from mumon fitting uncertainty and correction uncertainty are propagated together. Differences from the x angle scan with the same type of correction should be noted (fig. 6.27). A difference of horn currents is observed, with very small slopes for 320kA, with similar slopes observed for 0kA and 250kA, although the low statistics of the simulation make it difficult to make exact predictions for the slope, especially in the 0kA case.

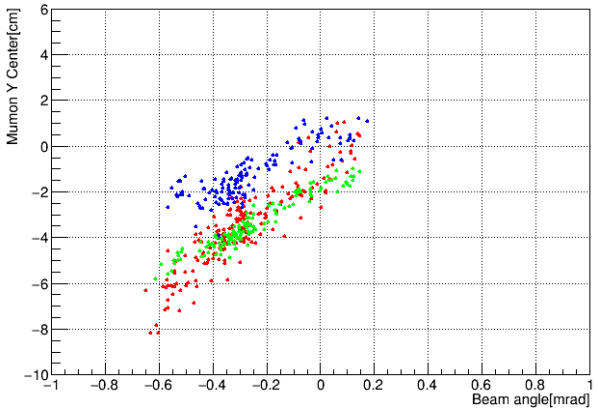

Figure 6.32: Run 12 anglescan with the target plane position corrected using simulated position scan data. Red is 0 kA, green is 250 kA, and blue is 320 kA. The error bars are omitted for clarity. The uncertainties on the beam angle are as before $\sim \pm 0.2$mrad. The beam angle uncertainty and target space position uncertainty are propagated with the errors of the fits on the simulated position scan. The total error on each point's corrected mumon Y center is $\sim \pm 1$cm.

scan was concluded. Although the beam angle scan is needed to check discrepancies present in the beam position scan and give insight into beam dynamics for the purpose of beam tuning, the measurement of the beam angle with at least 3 sensors (SSEM18, SSEM19, and OTR) is required. As of this writing, the OTR foil cannot be rotated to a foil usable for the low intensity beam used for the beam studies, and until OTR is fixed, a new beam angle scan cannot be carried out due to the requirement of a three point determination of beam angle.

Chapter 7

Analysis of Beamline component Alignment using Muon Monitor and Monte Carlo Simulations

7.1 Model Beam Position Scan Data Using FLUKA/JNUBEAM

To create a model for the beam position scan, the geometry at various x,y points of beam position was simulated and then a correlation plot of thrown beam position with the fitted Gaussian parameters of the resulting particles in the muon monitor plane can be obtained.

For the majority of the simulations, beam positions ranging between -18mm and 18mm were chosen with a spacing of 2mm, using a beam width of 3mm in both x and y, with Twiss parameters of α_x=0.00, α_y=-0.12, emit_x=4.5π mm mrad, and emit_y=3.75π mm mrad measured in Run 11 were used with a total of $300\times2\times10^5$ simulated protons for a total of 6×10^7 protons per simulation point. Although the choice of a beam width of 3mm is significantly less than that observed in the position scans in Run 12 & 13, a smaller beam width makes it easier to observe changes in certain features in the position scan, since the effective sampling region of the components is smaller.

The resulting FLUKA simulation outputs were used to seed JNUBEAM simulations of the rest of the secondary beamline, giving output information of the particles that intersect with the muon monitor plane. The resulting particle count is binned by their interaction position into 7×7 bins each with an area of $25 \times 25\text{cm}^2$. As seen in section 4.2, gamma rays have much less energy deposition in the mumon plane compared to muons and electrons, so they are cut from this fit. The remaining particles are about half and half electrons and muons, and are weighted equally in this fit. The resulting histogram is then fitted by a 2D gaussian and the parameters of this fit are used for the correlation plot between the Mumon center/width and the beam position at the entrance of the baffle.

It should be noted that there are some differences with using the seeded beam position in FLUKA since the proton creation position is at the entrance of the baffle, while in the position scans taken in Run 12 and Run 13, SSEM19 is used to estimate the beam position at the target. Since the baffle is ∼1.2 m downstream of SSEM19, the same measured beam width at SSEM19 and at the baffle results in a greater beam width at the target for the same width measured at SSEM19 compared with the baffle. Beam angle also yields slightly different results since the different baselines means the position difference compared with the beam center position in

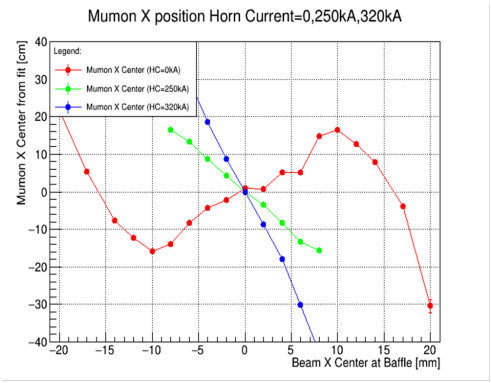

Figure 7.1: Simulated X position scan Mumon center.

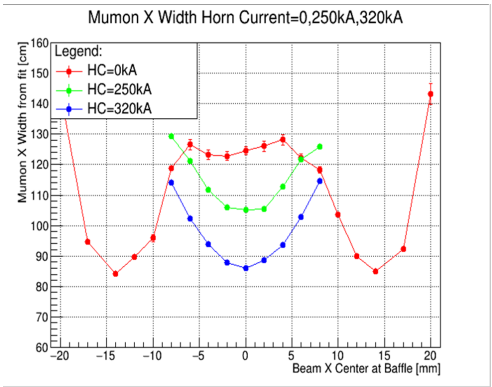

Figure 7.2: Simulated X position scan Mumon width

the target plane will be greater for measurements with SSEM19. Additionally, high intensity physics Run parameters were used for the emittance, but the emmittance in the main ring beam is known to increase with the protons per bunch, so the expected emittance of the beam during the low intensity beam position scan is likely significantly lower than the parameter used in the simulation. The changes between parameters do not affect the mumon response very much (see fig. 6.18), but it does add some systematic effects to the simulations that should be considered.

As mentioned in section 4, there is also an energy cutoff in JNUBEAM that cuts off low energy electrons that would ordinarily affect the muon monitor profile that are not simulated. Additionally, some structures in the muon monitor pit and the beam dump cooling system are not included in the JNUBEAM simulation, and may affect the muon monitor profile slightly. The systematic uncertainties on the muon monitor are shown in section 3.6.

Figures 7.1 and 7.2 show the simulated position scans using 3mm beam width at the baffle and nominal geometry. Points between [-14,14] were spaced at 2 mm, and then ±17 mm and ±20 mm were also simulated to cover the whole space of the position scan. Horn current on was simulated using the same FLUKA files for points between [-8,8] with a spacing of 2 mm. The horn current applied is exactly 250.0kA for the 250kA case and 320.0kA for the 320kA case. Clear symmetry is observed in the width for nominal geometry, and the peaks in mumon center are perfectly anti-symmetric. Additionally, the crossing point of the three horn currents is perfectly centered, and the minima of the horn current on width is at 0mm beam center. This serves as the basis for the expectation of the muon monitor behavior for nominal geometry that will be used to evaluate changes based on the changes in the simulated geometry.

Most of the studies shown below were done using Mumon X position scans, although in the simulation these should be able to be applied to the Y alignment as well, since in the simulation X and Y are almost completely symmetric in the simulation, with only minor differences observed. The effect of the tilted beamline is discussed in section 3.6.3, and is considered to be the main asymmetry present between X and Y.

7.2 Baffle Alignment

Since the baffle is located just upstream of the target in the target station, it is expected that changes to the baffle geometry would affect the symmetry of the proton beam position scan since different portions of the proton beam would be collimated by the baffle depending on the

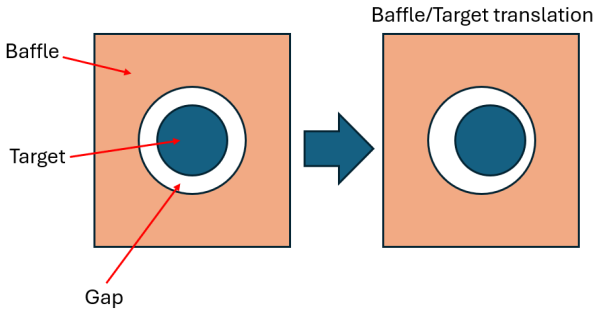

Figure 7.3: A drawing of the asymmetry created by translating either the baffle or the target.

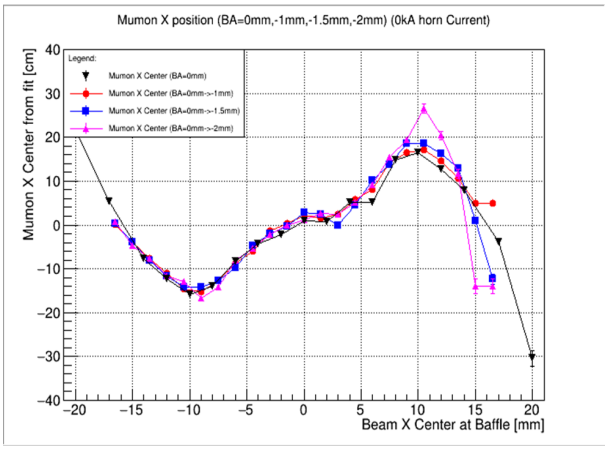

Figure 7.4: Simulated baffle translation horizontal position scan Mumon X center.

beam position. Since the muon monitor is sensitive to the tertiary muons resulting from the proton beam, by understanding the muon monitor behavior for different baffle alignments, it is possible to estimate the asymmetries in the baffle geometry using the position scan results.

7.2.1 Baffle Translation

As can be seen in Fig. 7.1 and 7.2, for the nominal geometry in the beamline, the resulting correlation plots are symmetric about zero. However, in the gathered data in Runs 12 and 13 (fig. 6.9 and fig. 6.6), a significant asymmetry is observed in the muon monitor width correlation plots. In previous works it was shown that an asymmetry like this can be generated as a result of the translation of the baffle.

By translating the baffle, the gap between the target and baffle (nominally 2 mm on each side) is extended on one side, while closed on the other. A drawing of this is shown in fig. 7.3 Since the dips result from this gap between the target and baffle, changing the size of these gaps asymmetrically would create a asymmetric shift in the height of these dips.

To simulate a baffle translation, the fluka geometry was modified and the baffle hole and baffle were both moved by -1 mm, -1.5 mm, and -2 mm in three separate sets of position scan simulations. These were simulated for beam centers between [-16.5 mm,16.5 mm] spaced every 1.5 mm for a total of 23 points. The beam width was set to 3mm at the baffle.

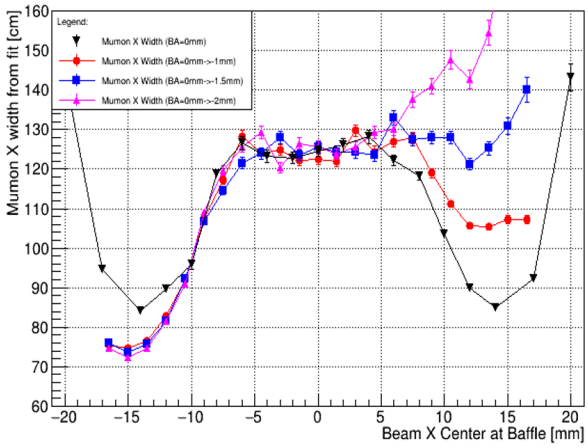

Figure 7.5: Simulated baffle translation horizontal position scan width. Error bars are only from errors on the fitted parameters.

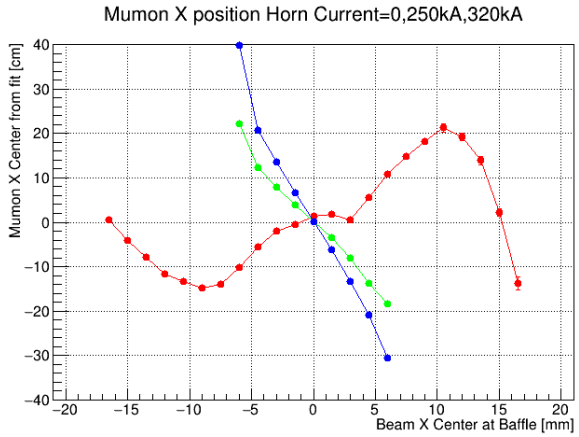

Figure 7.6: -1.5mm baffle translation with horn current on in JNUBEAM to find crossing point. Red is 0kA horn current, green is 250kA horn current, and blue is 320kA horn current.

Fig. 7.5 shows the effect of baffle translation on the width asymmetry in the simulated position scan. For all tested translations, the width at the dip at -15 mm is less than the width of the nominal geometry. Near +15 mm beam center, the height of the dip is sensitive to the amount of baffle translation, becoming larger than the width near the center of the target at translations greater than ∼1.5 mm. If the Run 13 position scan(fig. 6.6 asymmetry is thought to be only due to the translation of the baffle, the level of translation appears to be between -1 mm and -1.5 mm. However, it should be noted that baffle translation is not the only method to produce asymmetries seen in the data, and other component misalignments should also be considered. In principle, the asymmetry is likely to be the result of several effects rather than just one.

For horn current on, points between [-6,6] are resimulated in JNUBEAM with horn current on. Equal horn current is applied in all 3 focusing horns of exactly 250.0kA and 320.0kA respectively. It should be noted that the same FLUKA files are used for each point with horn current on, but JNUBEAM is resimulated with the horn current applied. This means that there may be biases in the FLUKA files that are propagated for all three horn currents. As seen in fig. 7.6, translating the baffle -1.5 mm does not change the crossing point significantly. There

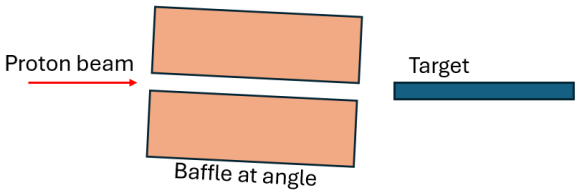

Figure 7.7: Exaggerated drawing to demonstrate geometry of baffle angle.

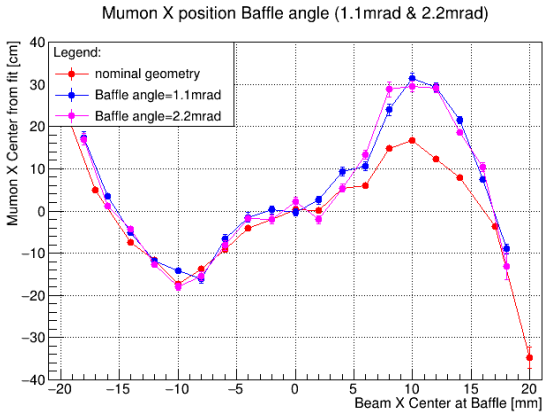

Figure 7.8: Position scan Mumon center for baffle angle alignment test.

is some asymmetry present for points at -4 mm and -6 mm that indicates that there may be baffle effects present as the beam moves across the target.

7.2.2 Baffle Angle

In addition to the translation of the baffle, a baffle angle can also contribute to the asymmetry observed in the beam position scan. In FLUKA, the geometry of the baffle is defined as rectangular and cannot be rotated without completely redefining the shape completely. However, the baffle hole can be rotated, which should be the dominant effect on the beam regardless. An exaggerated drawing of the baffle angle is shown in fig. 7.7. To test the effect of the baffle angle on the position scan, the near side of the baffle hole and the far side of the baffle hole were moved in relation to one another such that there is no net translation of the baffle, and only the angle effect is seen. The effect of baffle angle was tested in two scenarios, one is -0.1 mm near side and +0.1 mm far side, corresponding to a 0.11 mrad angle, and the other is -0.2 mm near side and +0.2 mm far side corresponding to a 0.22 mrad angle. These were simulated for beam positions between [-18 mm, +18 mm] with a spacing of 2mm for a total of 19 points.

Fig. 7.8 and 7.9 show the effects of baffle angle on the position scan. The exact origins of why there is such a large effect from the baffle angle are not well known, but is likely due to an asymmetric cutoff of particles in the beam. Since the baffle is tilted at a positive angle of 0.11 or 0.22 mrad, the protons with $+\frac{dx}{dz}$ are allowed in greater number, while protons with $-\frac{dx}{dz}$ are suppressed on the other side. Since the gap between the baffle and the target is not changed significantly, the width at the dip near -15 mm is the same as the nominal geometry. In the Run 13 position scan data (fig. 6.6), the Mumon X width has a minimum of $\sim 80cm$ for 0kA horn current, which is similar to that expected in the simulation. Although the exact value of these minima are subject to change with relation to proton beam parameters, this is

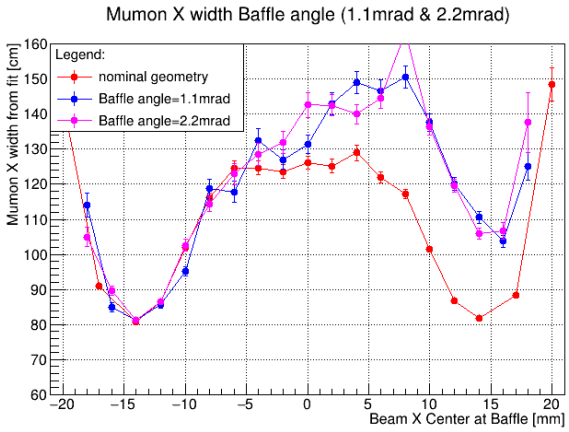

Figure 7.9: Position scan Mumon width for baffle angle alignment test.

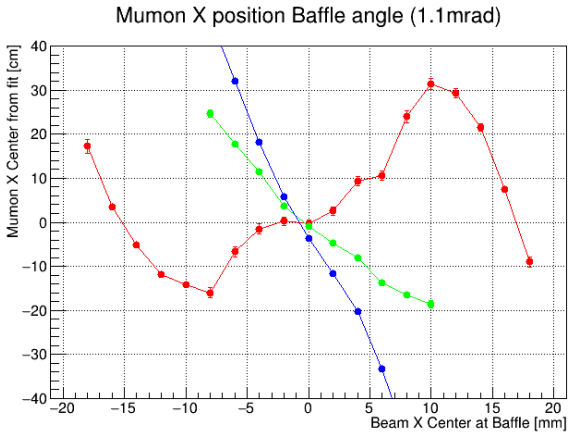

Figure 7.10: Position scan simulated for +0.11 mrad baffle angle with horn current on. 0kA horn current is red, 250kA is green, and 320kA is blue.

an indicator that there may not be a large translation of the baffle, but rather a baffle angle.

A clear sign of the baffle angle that is not present in other changes in beamline geometry is the asymmetric width peak in the region near the edge of the target before the large dip down in +x. It should be noted that again the magnitude of this asymmetry depends on the beam width, so with the higher beam width present in the data from the position scans, an asymmetry as large as seen in the simulation with a comparatively small beam width of 3mm at the baffle is unlikely. However, in fig. 6.6, there is a clear asymmetry in this region similar to that expected from a baffle angle.

As for the mumon center shift from baffle angle, a clear asymmetry is seen in fig. 7.8, with the maxima at +x increasing by $\sim$ 15cm.

Fig. 7.10 and fig. 7.11 show the position scan with horn current on effects. There is a clear shift of the crossing point towards -x and minima of the horn current on widths seen. The offset due to the baffle angle is fairly constant between a difference of 0.11 mrad and 0.22 mrad, so it is inferred that the crossing point offset plateaus in a proportionality similar to that of an error function or some similar plateauing function like arctangent.

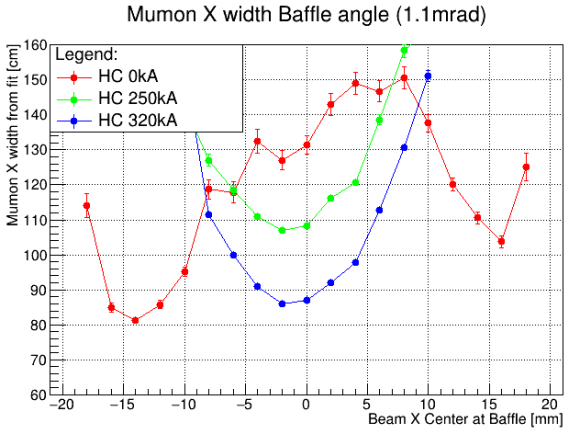

Figure 7.11: Width scan simulated for +0.11mrad baffle angle with horn current on. 0kA horn current is red, 250kA is green, and 320kA is blue.

The amount of misalignment required for the baffle angle to exhibit this kind of effect is much smaller than that of baffle translation, with an offset of 0.1 mm to the near side and far side in opposite directions yielding an asymmetry in the position scan similar to a full 1 mm translation. As such, it is more likely that baffle angle is the cause of asymmetries than baffle translation since the sensitivity to this effect is much larger.

7.3 Target Alignment

Target alignment is important to understand as well, since it can provide similar effects to the baffle on the asymmetries seen in the position scan. Additionally, possible target misalignment is important to understand, since the target geometry directly affects the neutrino beam direction. Since the asymmetry generated by baffle translation results from the gap between the target and baffle changing, consequentially, a similar asymmetry may be created by translating the target, although consequentially, the crossing point of the horn currents would be affected by an offcenter target as well, while the crossing point for baffle translation is shown to not be affected. This provides a method for disentangling the different effects present during this study.

7.3.1 Target Translation

To simulate target translation, the geometry of FLUKA and JNUBEAM must be modified to include the moved target such that any shifts are reflected in both simulations to avoid double interacting with the target. Simulations were done at -1 mm and +1 mm target translation to observe the effects.

Fig. 7.12 shows the width asymmetry for a target translation. Target translation results in a trivial shift of the width minima equal to the that of the translation. In this case, -1mm target translation yields a shift of the width minima of the horn current on case in the opposite direction of the translation equal to +1mm. This is similar to the effect from baffle angle on the crossing point and these effects cannot be easily disentangled. The width minima of the 0kA scan are asymmetric, similar to the baffle translation case, since the gap between the baffle and target is changed by the target translation (see fig. 7.3). The beam position at the width minima is not changed by the target translation.

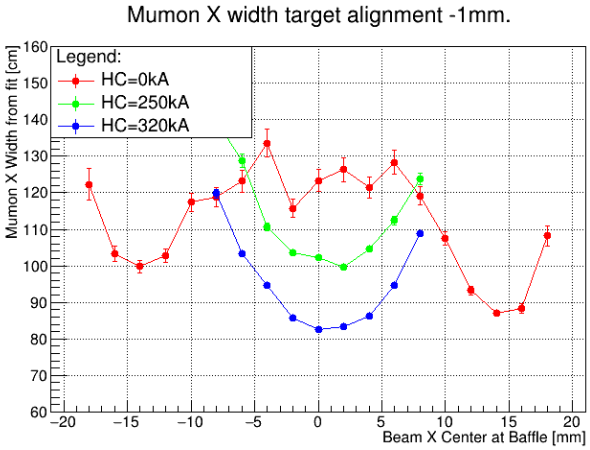

Figure 7.12: Mumon width during X position scan for target translation of -1mm.

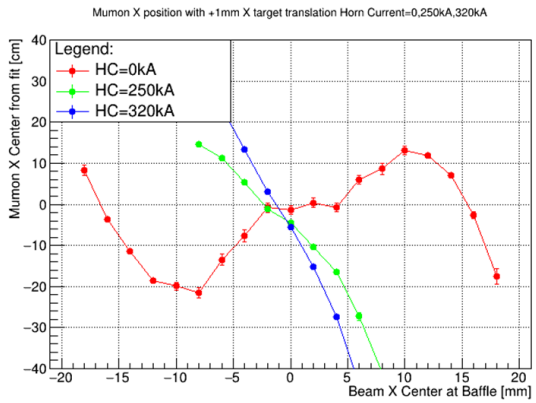

Figure 7.13: Target translation of +1mm position scan with the three horn currents simulated.

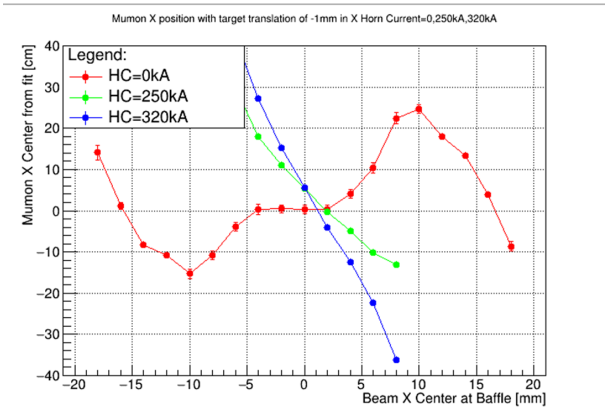

Figure 7.14: Target translation of -1mm position scan with the three horn currents simulated.

Fig. 7.13 and fig. 7.14 show the position scan plots with the target translated +1 mm and -1 mm respectively. The most noticable shift compared to nominal geometry is near the center, where there is a clear deviation between the horn current on and off cases, shifting the crossing point in the opposite direction of the translation. In addition, the flatter region near the center of the position scan is clearly shifted towards one side or the other. This region of the graph is not very reliable however, since the slope here depends on beam width and may be affected by other factors such as baffle angle or target angle. The horn current on case, and most drastically the 250kA case exhibits curvature in the opposite direction of the translation direction.

A splitting is observed between the intersection between the 320 kA and 250 kA lines compared with the intersection of the 320 kA line with the 0 kA line. This can be used to separate the effects of the target translation and baffle angle, since this feature was not seen in the baffle alignment studies. This feature likely arises from the target axis not aligning with the axes of the three focusing horns.

7.3.2 Target Angle

The target angle is tricky to simulate in FLUKA and JNUBEAM. Due to the limitations of the FLUKA geometry, both faces of the cylindrical target will be completely flat relative to the beam. For the angles of 1mrad simulated this effect is expected to be relatively small, but there may be some differences based on the angle of incidence considering a relatively small proton beam angle of 0.1 mrad has a measurable effect. Other than this discrepancy, the bulk of the target is rotated by the desired angle in both FLUKA and JNUBEAM and the position scans were simulated with $300\times2\times10^5$ protons for beam positions between [-18 mm,18 mm] with a spacing of 2 mm.

The target angle is known to be within ±1.3 mrad for X and ±0.2 mrad in Y in relation to the beam axis [21]. In the case of X at least, there is reason to consider the effect of 1 mrad level effects on the target alignment for the position scan.

The results of the simulation using +1 mrad and -1 mrad for the target angle are shown in fig. 7.15 and 7.16 respectively. The crossing point is shifted for the horn current on case similarly to the target translation, but with a comparatively smaller effect. A width asymmetry is created with target angle as well (fig. 7.17), but is comparatively smaller than the effect from baffle misalignments. The maxima and minima in the position scan graph are not changed much by the target angle, and are expected to be ±10 mm in beam position.

7.3.3 Component alignments not included in this study

Not all alignment of components in the beamline were simulated, and some may affect the position scan using the muon monitor. In section 3.6, the systematic error due to the profile distortion from alignment of the beam dump was discussed [16]. This represents a portion of the total systematic error of ±0.38cm for the mumon center. While the exact asymmetric effects based on the position scan were not checked in this study, this general effect is taken to be the effect of the misalignment of the beam dump.

Horn alignment was not checked in this position scan study, but the effect of the horn alignment on the Mumon center has been studied previous in the Mumon group in the case of 0kA, 250kA, and 320kA. There is little indication that the alignment of the horns affects the position of mumon center very much, but the exact effects on the position scan are not well known. As

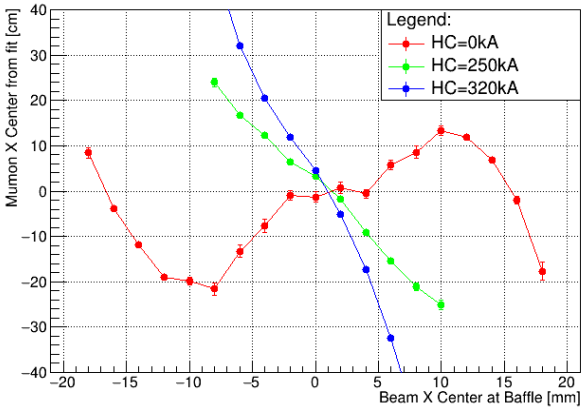

Figure 7.15: Simulated position scan with a target angle of +1 mrad.

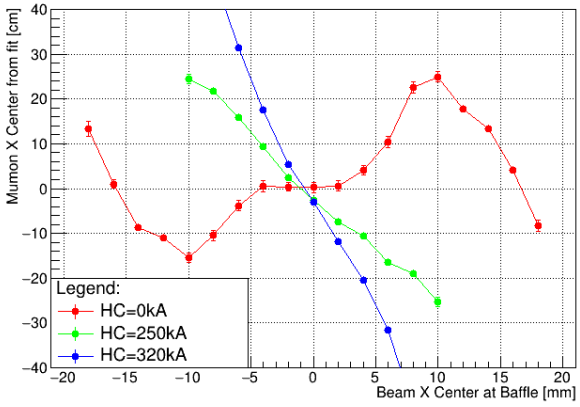

Figure 7.16: Simulated position scan with a target angle of -1 mrad.

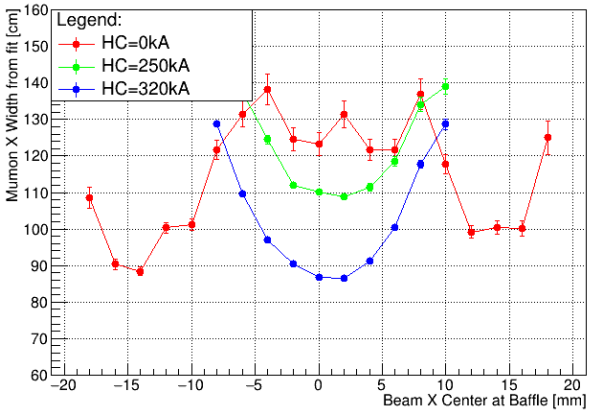

Figure 7.17: Simulated position scan Mumon width with a target angle of +1 mrad.

discussed in the target alignment section, the crossing point splitting is thought to arise from a misalignment of the target axis and the three horn axes, which of the horns affects the muon monitor response is not known, although it is expected to be horn 3, since it is the last in the beamline. The horn alignment is known to be within ±1 mm in Y and ±0.3mm in X [21], and horn angle is known to within ±0.2 mrad.

7.4 Effects from Beam Parameters

7.4.1 Beam Width

Beam width affects the overall shape of the position scan correlation plots significantly. The beam width parameter represents the gaussian width of the beam. As the beam is scanned across the baffle and target, the areas that the beam samples are different depending on the beam width. Since the shape of the position scan correlation plot depends on which components the beam impacts (as discussed in sec. 4.2 and 6.2), the higher width the beam is, it "smooths" the shape of the plot, blending together the features, while a lower beam width tends to provide greater detail. A comparison between 3mm and 4mm beam width can be seen in fig. 6.19

Beam width when the beam reaches the target depends on many factors of the accelerator, from the main ring, to the final focusing section, and varies between Runs as the result of changes to equipment settings. The simulations done in this thesis primarily use 3mm beam width, with some using 4mm. Beam width does affect the resolution of the features in the position scan plot that result from beamline component alignment

7.4.2 Twiss Parameters

As shown in fig. 6.18, there is some minor dependence of the position scan measurement in Mumon on the twiss parameters used in the simulation. For the most part, this is negligible compared to other effects discussed here. The main effect of the twiss parameters is that the emittance changes the height of the minima in the 0kA width measurement for the beam position scan.

7.5 Simulation Based Model for Beamline Component Alignment Estimation

In order to determine the beamline alignment from analysis of the position scan, features of the position scan that are unique to each type of misalignment should be considered to attempt to avoid degenerate effects. In addition, the effects of beam parameters such as proton beam width, twiss parameters, and proton beam angle should be considered for the beam position scans in order to mitigate the effects. In addition, the systematic errors on mumon should be taken into account, with a total of ∼2.3 cm error on the mumon center in both X and Y. This error is large commpared to the muon monitor resolution (∼<3mm), so choices of measurements that do not depend on the absolute value of the muon monitor are preferred.

The position scan simulations using alignments of the target and baffle are compiled in fig. 7.18 for ease of reference.

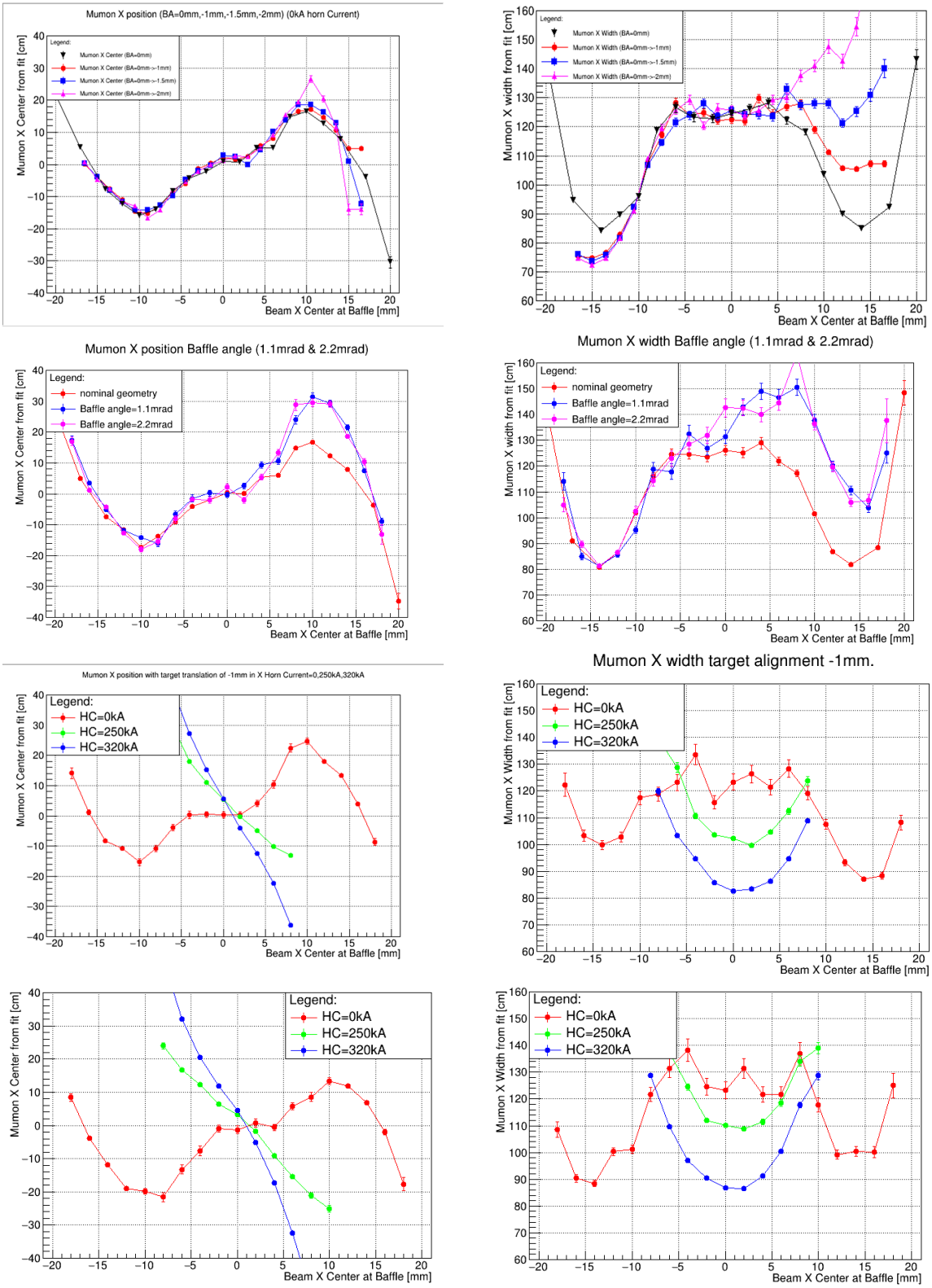

Figure 7.18: Simulated position scans of baffle translation (top), baffle angle (2nd from top), -1 mm target translation (3rd from top), and +1 mrad target angle (bottom).

Baffle translation is difficult to separate from other effects since the main effect observed is the asymmetry created in the width minima, which is similar to the asymmetries seen in baffle angle, and target translation/angle, and determination of the exact widths at these minima are affected by beam width/emittance, and angular effects. One unique aspect of baffle translation is that the minima in the same direction of the translation is less than that seen in the nominal geometry, since the gap between the baffle and target is wider. However, since the nominal geometry case is not known in the data, this is also not a reliable method to determine baffle translation. As such, the only estimation that can be made for baffle translation is if all other effects are ignored, the asymmetry seen in the data is similar to a translation between -1 mm and -1.5 mm.

Baffle angle direction can be estimated using the asymmetry seen in the width in the region near the target center. A determination of the exact baffle angle is difficult since effects such as the crossing point shift and heights of minima/maxima have contributions from different component alignments. The minima of the horn current on widths can provide an estimation of the baffle angle, however, this is a similar effect to that seen in the target translation and target angle as well, so it is difficult to separate the effects only using this method.

Using these determinations, equations describing the expected shift of these position scan features can be determined. The fundamental assumption is that each of the effects are independent of one another, which is not necessarily true, however, due to the volume of simulations required to check all possible combinations of component alignment, this was not studied in detail.

The crossing point shift is affected by both the baffle angle and target angle. The effect of the baffle angle on the crossing point and horn current on width minima was constant ∼-1 mm for both 1.1 mrad, and 2.2 mrad, so the effect is inferred to plateau around those values. Since there were no simulations done of angles smaller than 1.1 mrad, the exact behavior near 0 baffle angle is not known. An error function was chosen due to the gaussian shape of the beam.

As discussed in sec. 7.3.1, the shift of the horn 250 kA and 320 kA current intersection from the intersection with the 0kA horn current line is a feature unique to the target translation and target angle, so an estimation of the target translation can be found from the difference between these two lines. A simple linear function is chosen for the size of this difference. Similarly a linear function is chosen to represent the effect of the target angle. The beam position at the intersection of the horn current on settings is equal to the target translation. The shift due to the beam angle in the ideal case is just the propagated position in the target plane. The obtained modes are:

$$\begin{aligned} &\text{Beam pos}_{x,\text{cross}} = -\text{Erf}(\phi_{\text{baffle}}) - \Delta_{\text{target}} + \phi_{\text{target}} \cdot \kappa - \theta_x \cdot d \\ &\Delta\text{Mumon}_{x,\text{cross,HC on}} = -\Delta_{\text{target}} \cdot \alpha + \phi_{\text{target}} \cdot \beta \end{aligned} \qquad \left\{ \begin{array}{c} \kappa = 0.77 \frac{\text{mm}}{\text{mrad}} \\ d = 2.24 \frac{\text{mm}}{\text{mrad}} \\ \alpha = 5.8 \frac{\text{cm}}{\text{mm}} \\ \beta = 0.74 \frac{\text{cm}}{\text{mrad}} \end{array} \right\} \quad (7.1)$$

Beam $\text{pos}_{x,\text{cross}}$ is the beam position at the upstream end of the baffle at the crossing point. $\text{Erf}(\phi_{\text{baffle}})$ is the error function of the baffle angle in mrad. Δ_{target} is the target translation and ϕ_{target} is the target angle. The factor κ was found to be 0.77 $\frac{\text{mm}}{\text{mrad}}$ from the minima of the 320 kA horn current width in the target angle simulations. There is a systematic error from the fit of ± 0.02 $\frac{\text{mm}}{\text{mrad}}$. There is some difference in the effect of the SSEM crossing point based on horn current in the case off the target angle (250 kA crossing point is ∼double the effect of

320 kA) due to 320 kA providing a stronger focusing effect, but since there is more data in the position scans for 320 kA horn current, the 320kA simulation was used to calculate the expected crossing point. As before θ_x is the beam angle with a factor to propagate the beam center to the target ($d = 2.24\frac{\text{mm}}{\text{mrad}}$ in simulation). $\Delta\text{Mumon}_{x,\text{cross,HC on}}$ is defined as the difference between the intersection of 320 kA and 250 kA compared to the average of the intersections of the horn current on lines with the 0 kA line. The factor of α =$5.8\frac{\text{cm}}{\text{mm}}$ is from the linear fit of the 3 target translation simulation points with the no translation crossing point fixed to 0. The systematic error from this fit is $\pm 0.32\frac{\text{cm}}{\text{mm}}$. ϕ_{target} is the target angle in mrad. Similarly, the factor of β =$0.74\frac{\text{cm}}{\text{mrad}}$ is from a 3 point linear fit of the simulated crossing points similar to that described for the target translation. The error on this fitted parameter is $\pm 0.084\frac{\text{cm}}{\text{mrad}}$.

Using the crossing points reported in Tables 6.2, 6.1, 6.3, and 6.4, the horn current crossing point shift, and thus the cumulative effect of target translation and target angle can be calculated for both Run 12 and Run 13. The difference between the measured muon monitor center values at the intersection of the 250 kA and 320 kA lines with the average mumon center at the intersection of the 250kA and 320kA lines with the 0kA line (see figs. 6.12 6.14, 6.11, 6.13). For the horizontal axis, a difference of -0.59 cm in Run 13 and -0.61 cm in Run 12 was observed. For the vertical axis, in Run 13, a difference of -2.81 cm and -3.92 cm in Run 12 was observed.

By inspection, both Run 12 and Run 13 for both horizontal and vertical directions have an asymmetric width near the target center indicating a positive baffle angle. For X in Run 12, an average angle of -0.03 mrad was observed, and for Run 13, an average angle of +0.1 mrad was observed. For Run 13 in Y, an average angle of -0.15 mrad was observed. The SSEM value for the crossing points of the intersection of the 0kA line with the 320kA line was used for the determination of alignment.

If the target translation found from the horn current splitting is used as an input to the beam position at the crossing point, there is either a negative baffle angle, which is opposite to the effect seen in the asymmetric width near the target center and the expected asymmetry of the width minima for 0 kA horn current, or a large target angle which is greater than the measured tolerances[21] depending on prior assumptions of parameters. If the baffle angle effect is instead fixed, then the target translation is opposite and greater than that expected from the horn current splitting. This implies that there is either another effect besides beam angle and the alignment of the baffle and target. This may be explained by horn alignment, since the focal point of the horns would change slightly if they were offset, however, as discussed previously, this was not tested for the position scan in simulation. Additionally, an offset of $\sim$0.3 mm between the SSEMs and target station may also explain this disagreement.

Since determinations using the beam position were deemed unreliable, only target translation was concretely estimated, since its effect on the shift of the horn currents results in a comparatively large effect on the Mumon crossing point. An error on the translation related to the target angle taken to its limits of $\pm$1.3 mrad for x and $\pm$0.2 mrad for y [21] was applied. These target angles correspond to a splitting of the mumon crossing points of $\pm$0.96 cm for X and $\pm$0.15 cm for Y. Since the splitting in X is smaller than the possible shift created by the target angle, the error is dominated by the target angle effect. For Y, the error is instead split between contributions from determination of the crossing points, target angle, and the modelling of the target translation effect.

Thus the target translation can be calculated with the assumption of 0 target angle with the appropriate error applied. The results of these calculations are shown in tables 7.1 and 7.2. Since the effect is small, and the uncertainty on the target angle is large for x, whether the horn current splitting is due to target translation or target angle cannot be discerned. In Y,

Run	$\Delta_{x,\text{baffle}}$	$\phi_{x,\text{baffle}}$	$\Delta_{x,\text{target}}$	$\phi_{x,\text{target}}$
Run 12	Unknown	Positive	0.11±0.17 mm	$<$ |1.3 mrad|
Run 13	Unknown	Positive	0.10±0.17 mm	$<$ |1.3 mrad|

Table 7.1: Table of the calculated values for beamline component horizontal alignment using averages from Run 12 and Run 13.

Run	$\Delta_{y,\text{baffle}}$	$\phi_{y,\text{baffle}}$	$\Delta_{y,\text{target}}$	$\phi_{y,\text{target}}$
Run 12	Unknown	Positive	0.68±0.07 mm	$<$ |0.2 mrad|
Run 13	Unknown	Positive	0.48±0.04 mm	$<$ |0.2 mrad|

Table 7.2: Table of the calculated values for beamline component vertical alignment using averages from Run 12 and Run 13.

the splitting is more substantial, and the expected angle of the target is small, so an offset of the target and horn axis is expected.

7.5.1 Agreement with Target Station Survey Results

In the summer maintenance period between Run 12 and Run 13, the helium vessel in the target station was opened for work and maintenance. During this period an alignment survey was done on the geometry in the helium vessel, including alignment of the baffle and horn 1. The results are shown in fig. 7.19. The survey mostly considers internal alignment within the helium vessel due to the wall between the primary beamline and the helium vessel. Since the actual beam center line is obscured by the beam window and target station walls, a determination of the center line is found using a line offset from the beamline to establish the alignment between the primary beamline and the helium vessel. The measured baffle translation was -0.4mm and a baffle angle of +1.1mrad in X and +0.65mm translation and an angle of +0.275mrad. The target alignment was not measured, however it is known to be centered with the horn 1 axis to a precision of ±0.1 mm on the front face of the horn[21]. This implies the translation of the target and horn 1 to be equal to that of the near side of horn 1. In this case, +0.2 mm in the horizontal direction, and +0.5 mm in the vertical direction (averaged both horizontal sides). Since the horn current splitting used to estimate target translation results from an offset between the horn axes and the target, more position scan simulations need to be done in order to ascertain which horn alignment has the dominant effect on the muon monitor profile. The calculated results for the target translation do appear to match the target station survey, however, until the effects of each of the horn's alignment can be properly separated, only tentative agreement of can be claimed. As for the baffle angle, the inferred direction agrees with the measured angle in the target station survey.

A simulation was done with the survey results for the baffle alignment to attempt to find the expected position scan results given this measurement of the baffle position. The results can be found in fig. 7.20. The baffle angle contributes to the asymmetric width near the target center. It can be seen that the width minima of the horn current on case are shifted towards $-x$. The target alignment was not applied for this simulation.

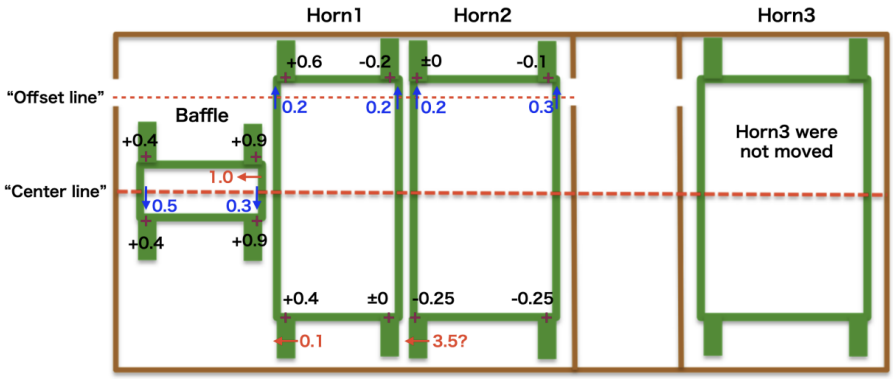

Figure 7.19: Alignment values measured in the helium vessel survey. Alignment was measured by the alignment of the markers located at each '+'. Units are in mm. To maintain a right handed coordinate system with the z-axis along the beamline (→), the x-axis is chosen to be 'up' on this diagram, and the y-axis is chosen to be out of the page. The precision of these measurements is 50μm[2]

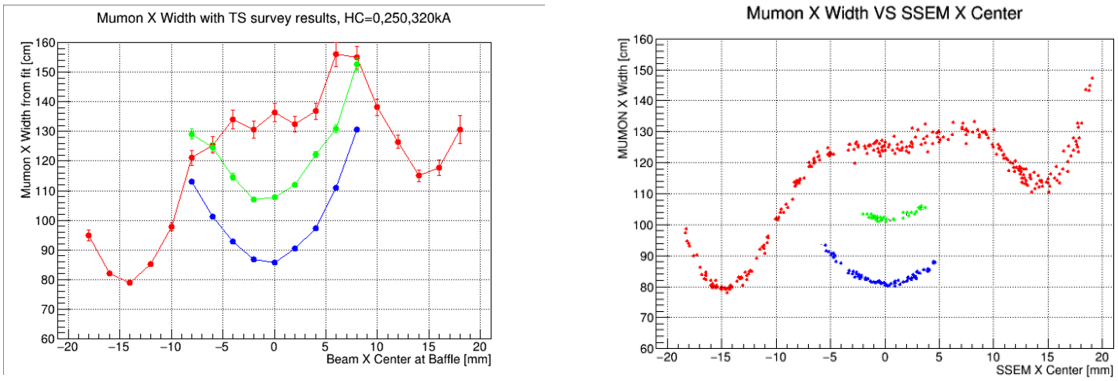

Figure 7.20: Simulated X position scan using helium vessel survey data as inputs for the baffle geometry and 3 mm beam width (left) compared with the run 13 position scan (right). The main difference in the shape is thought to be due to beam width during the position scan being greater during the position scan than in simulation (fig. 6.19)

Chapter 8

Muon Monitor Sensor Layout Fitting Tests

8.1 EMT Layout fitting evaluation

As discussed in sec. 3.4, the EMT sensor is being tested as a replacement to the Si sensor for the higher beam power of the Hyper-K era. Due to the cost of the EMT sensor, using 49 sensors such as in the current layout of the Si sensor would prove costly, so a test of different sensor configurations was conducted to ascertain the effects of reducing the sensor count on the 2D gaussian fitting results. Additionally, due to a limited number of 118 channels in the muon monitor data acquisition, in the intermediary era before 1.3MW beam, it is important to continue using Si and IC sensors while EMTs are still being tested. A mockup of the different test configurations is shown in fig. 8.1

To find the effects, the different configurations were tested with muon monitor SI array data from Run 13 in a variety of conditions, including a beam position scan (detailed explanation is in chapter 5) where the beam is scanned across the target at low intensity ($O(10^{12})$ protons per bunch) with a 2 bunch structure. This results in large variations in the fit of the mumon sensor, as well as nongaussian effects that have effects on the results from the current 49 sensor fit (discussed in more detail in chapter 4). The position scan is done with the focusing horns off, a horn current of 250kA, and a horn current of 320kA. This represents a large variation stress test of the different configurations of the test EMT configurations. Additionally, a normal physics Run from Run 13 was included to represent normal Running conditions of the muon monitor.

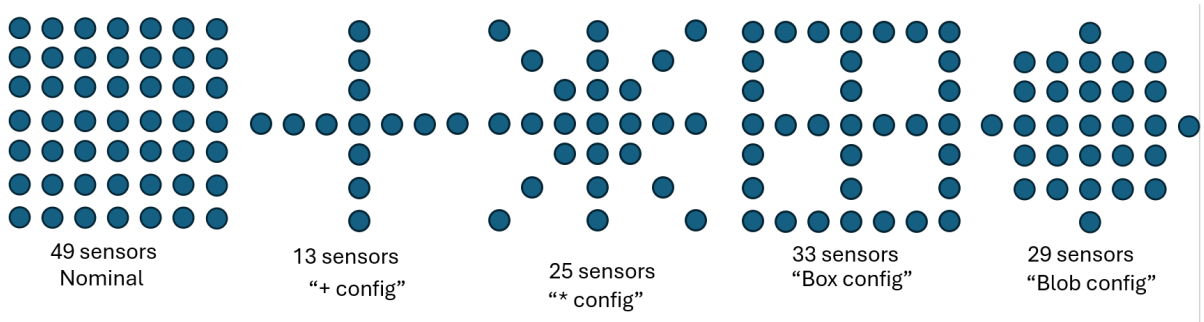

Figure 8.1: The test configurations for the EMT fitting scenarios.

Run type	plus config	star config	box config	blob config
Position scan (0kA)	3.35	0.62	0.62	2.56
Position scan (250kA)	1.76	0.22	1.04	0.37
Position scan (320kA)	2.03	0.22	0.98	0.70
Normal physics Run	1.83	0.16	0.53	0.08

Table 8.1: Average difference(cm) from 49 sensor configuration of the fitted muon profile center for different test configurations

Run type	plus config	star config	box config	blob config
Position scan (0kA)	22.86	3.55	2.98	21.06
Position scan (250kA)	6.69	1.31	0.41	6.46
Position scan (320kA)	6.36	1.47	0.45	5.96
Normal physics Run	5.79	1.22	0.41	5.37

Table 8.2: Average difference(cm) from 49 sensor configuration of the fitted muon profile width for different test configurations

To test the different configurations, histograms were filled with the Si sensor's integrated charge from all bunches of the beam and fitted while excluding certain bins from the fit to match the configuration of choice. The resulting fit parameters were extracted and the variation compared with the 49 sensor configuration were tested.

The results of the various tests can be found in Table 8.1. It can be seen across all tests that the "plus configuration" performs particularly badly, as might be expected of fitting a 2D gaussian with this level of sampling. For the test with the focusing horns off, the box configuration performed well, likely due to the wider muon beam that occurs without the focusing effect, while during Runs with the focusing horns on, it performs worse due to the lack of sampling near the center of the muon profile. Conversely, the "blob" configuration performs badly in the test without the focusing horns, and significantly underestimates the width of the muon profile compared to the 49 sensor fit. This configuration works better in scenarios with the focusing horns on, since it has good sampling near the center of the fit, although it still underestimates the width of the profile. The "star" configuration performs well under the most scenarios, having only small variations compared to the current 49 sensor fit, as well as having a low sensor number of 25. As the result of this test, the "star" configuration was chosen to be the EMT configuration for the next upgrade of the muon monitor after the "plus" configuration, which will be installed during the 2024 summer maintenance and used for 1D fitting in both the X and Y axis.

8.1.1 Effect of IC dead sensor on fit results

As of Run 13, one of the corner sensors of the ionization chamber sensor was found to be extremely noisy, so the data acquisition software was modified to cut the channel from the fit to reduce the effects of the noisy channel on the monitor. While this channel is dead and the cause is being investigated, it is important to understand the effect of cutting the sensor from the fit. Although Si is generally used as the primary sensor for the muon monitor, in the event that the Si sensor has a failure, IC will instead be used as the primary sensor for the muon monitor.

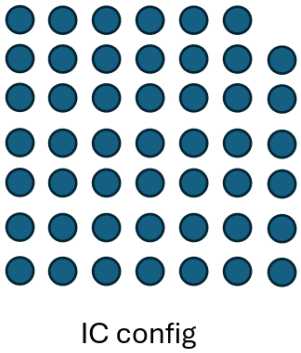

Figure 8.2: IC with the dead sensor removed from the fit.

Run type	IC (center)	IC "star"(center)	IC (sigma)	IC "star"(sigma)
Position Scan (0kA)	0.49	0.89	1.69	5.19
Position Scan (250kA)	0.14	0.13	0.40	1.99
Position Scan (320kA)	0.14	0.28	0.35	1.70
Normal physics Run	0.11	0.05	0.24	1.55

Table 8.3: Average difference (cm) from 49 sensor fit of the IC dead sensor tests.

To test the effect on the fit, the same process used to evaluate the EMT configurations in the previous section was used. The fit configuration used was 48 sensors with just 1 corner sensor removed from the fit, as pictured in fig. 8.2. This configuration was used to fit the Si sensors across 4 tests, the x-axis position scan at 0kA, 250kA, and 320kA horn current, as well as a normal physics Run from Run 13. Additionally, as the data acquisition channels from IC will be used in the EMT upgrade to facilitate the adding of 18 more EMTs, if the cause of the noisy channel cannot be fixed, the IC sensor will also be ran in a "star" configuration with 1 corner sensor missing. This was also tested to see the possible effect in this era. The results found are listed in Table 8.3.

The effect of missing sensor creates a systematic deviation in the fit, resulting in an average deviation of $\sim$0.11cm difference in the fitted center parameter compared with the 49 sensor fit. This is not a dominant error for the IC sensor (see sec. 3.6), but should be considered as an additional systematic error to the fitted parameters, especially in the event IC is used as the primary sensor. As seen in fig. 8.3 and fig. 8.4, there is a bias towards the opposite corner than the removed sensor.

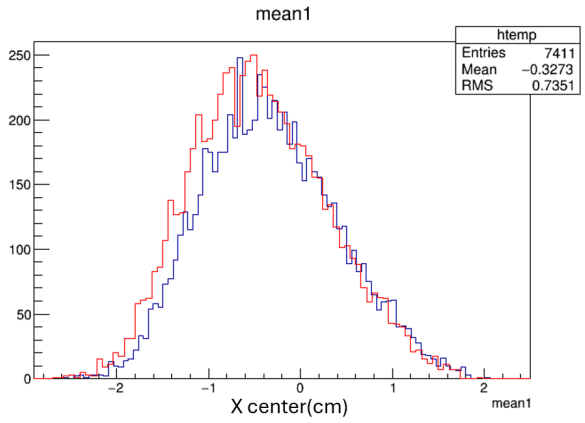

Figure 8.3: IC dead sensor fitted X center (red) compared with the nominal 49 sensor fit (blue) for a high intensity physics Run. There is a small bias towards negative X seen in the IC dead sensor fit.

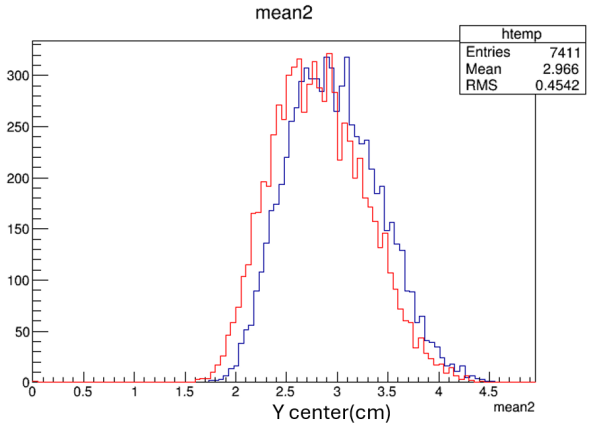

Figure 8.4: IC dead sensor fitted Y center (red) compared with the nominal 49 sensor fit (blue) for a high intensity physics Run. There is a small bias towards negative Y seen in the IC dead sensor fit.

Chapter 9

Conclusion

The T2K experiment is still a statistically limited experiment, and it is planned to take increased data as the beam power increases in the next few years, up to a planned beam power of 1.3 MW, with the recent achievement of 750 kW and the near detector upgrade finished for Run 13. As of the 2023 results using data up to Run 11, there is a $\sim 2\sigma$ significance for CP violation with a preference for δ_{CP}=-$\frac{\pi}{2}$, corresponding to a maximally CP violating neutrino sector.

In order to accept a high intensity proton beam, measurement of the neutrino flux direction is highly important. Furthermore, a spill by spill measurement of the secondary flux direction is indispensible. The muon monitor is used to measure the muons created alongside muon neutrinos in pion decay. The SI and IC arrays have provided a measurement of the muon beam direction within the desired precision of 0.3 mrad. As the beam power increases to 1.3 MW, the radiation damage becomes too high in the SI array to continue using it as the primary sensor. As such, the electron multiplier tube (EMT) is the best candidate sensor to replace it, with 7 sensors currently installed in a row centered vertically in the muon monitor behind the SI-array. In summer 2024, this will be upgraded to a + shape for 1D fitting of both the horizontal and vertical profiles of the muon monitor. Since the beam is known to have a 2D gaussian profile, it is desired to upgrade this sensor to 2D fitting in order to properly sample the muon profile. Several configurations were tested, and the most cost efficient sensor configuration was found to be 25 sensors in a "star" configuration.

Simulations were carried out to understand the muon flux in the muon monitor. The assumed gaussian profile was found to actually be a double gaussian or a gaussian+gaussian shape, particularly in the 0 kA horn current case where the focusing horns are turned off. This structure results from where the proton beam impacts in the secondary beamline, with the main components being from the target and from the beam dump. This structure and the dependence on proton beam angle was successfully extracted both in simulation and actual data for 0 kA horn current, but was unable to extract the profile when the focusing horns were turned on to 250 kA and 320 kA since these match more closely to the expected single gaussian shape.

In order to accurately align the proton beam to the center of the target, proton beam position and angle scans were carried out in Run 12 and Run 13, where the intersections of the horn current off and horn current on responses in the muon monitor were used to align the beam with the center of the target. It was concluded that the differences between the position scans in Run 12 and Run 13 were due to differences in proton beam angle and proton beam width.

Deviations from the simulated position scan with ideal component alignment were seen, so various simulations were carried out testing baffle and target alignment using FLUKA and

JNUBEAM. The baffle translation and target translation could be calculated for the position scans in Run 12 and Run 13, and the direction of the baffle angle could be determined. These results showed agreement with the helium vessel survey carried out in summer, 2023, although the expected crossing point determined only using the baffle and target alignments could not explain the shift in the crossing point seen in the position scan, implying that there may be effects from components whose misalignment effects were not simulated, such as the focusing horns, or a misalignment between the helium vessel and the SSEMs of an order of 0.3 mm.

Bibliography

[1] Y Ashida, M Friend, A K Ichikawa, T Ishida, H Kubo, K G Nakamura, K Sakashita, and W Uno. A new electron-multiplier-tube-based beam monitor for muon monitoring at the T2K experiment. *Progress of Theoretical and Experimental Physics*, 2018(10):103H01, 10 2018.

[2] K. Abe et al. The t2k experiment. *Nuclear Instruments and Methods in Physics Research Section A: Accelerators, Spectrometers, Detectors and Associated Equipment*, 659(1):106–135, 2011.

[3] C. L. Cowan, F. Reines, F. B. Harrison, H. W. Kruse, and A. D. McGuire. Detection of the free neutrino: a confirmation. *Science*, 124(3212):103–104, 1956.

[4] G. Danby, J-M. Gaillard, K. Goulianos, L. M. Lederman, N. Mistry, M. Schwartz, and J. Steinberger. Observation of high-energy neutrino reactions and the existence of two kinds of neutrinos. *Phys. Rev. Lett.*, 9:36–44, Jul 1962.

[5] K. Kodama et al. Observation of tau neutrino interactions. *Physics Letters B*, 504(3):218–224, April 2001.

[6] Raymond Davis, Don S. Harmer, and Kenneth C. Hoffman. Search for neutrinos from the sun. *Phys. Rev. Lett.*, 20:1205–1209, May 1968.

[7] Y. Fukuda et al. Evidence for oscillation of atmospheric neutrinos. *Physical Review Letters*, 81(8):1562–1567, August 1998.

[8] R. L. Workman and Others. Review of Particle Physics. *PTEP*, 2022:083C01, 2022.

[9] M. H. Ahn et al. Measurement of neutrino oscillation by the k2k experiment. *Physical Review D*, 74(7), October 2006.

[10] K. Abe et al. Observation of electron neutrino appearance in a muon neutrino beam. *Phys. Rev. Lett.*, 112:061802, Feb 2014.

[11] K. Abe et al. Measurements of neutrino oscillation parameters from the t2k experiment using 3.6×10^{21} protons on target. *The European Physical Journal C*, 83(9), September 2023.

[12] K. Abe et al. T2k nd280 upgrade – technical design report, 2020.

[13] K. Matsuoka, A.K. Ichikawa, H. Kubo, K. Maeda, T. Maruyama, C. Matsumura, A. Murakami, T. Nakaya, K. Nishikawa, T. Ozaki, K. Sakashita, K. Suzuki, S.Y. Suzuki, K. Tashiro, K. Yamamoto, and M. Yokoyama. Design and performance of the muon monitor for the t2k neutrino oscillation experiment. *Nuclear Instruments and Methods in Physics Research Section A: Accelerators, Spectrometers, Detectors and Associated Equipment*, 624(3):591–600, 2010.

[14] H.J. Ziock, J.G. Boissevain, K. Holzscheiter, J.S. Kapustinsky, A.P.T. Palounek, W.E. Sondheim, E. Barberis, N. Cartiglia, J. Leslie, D. Pitzl, W.A. Rowe, H.F.-W. Sadrozinski, A. Seiden, E. Spencer, M. Wilder, J.A. Ellison, J.K. Fleming, S. Jerger, D. Joyce, C. Lietzke, E. Reed, S.J. Wimpenny, P. Ferguson, M.A. Frautschi, J.A.J. Matthews, and D. Skinner. Temperature dependence of radiation damage and its annealing in silicon detectors. *IEEE Transactions on Nuclear Science*, 40(4):344 – 348, 1993. Cited by: 34.

[15] A. Van Ginneken. Nonionizing Energy Deposition in Silicon for Radiation Damage Studies. 10 1989.

[16] K. Suzuki, S. Aoki, A. Ariga, T. Ariga, F. Bay, C. Bronner, A. Ereditato, M. Friend, M. Hartz, T. Hiraki, A.K. Ichikawa, T. Ishida, T. Ishii, F. Juget, T. Kikawa, T. Kobayashi, H. Kubo, K. Matsuoka, T. Maruyama, A. Minamino, A. Murakami, T. Nakadaira, T. Nakaya, K. Nakayoshi, M. Otani, Y. Oyama, N. Patel, C. Pistillo, K. Sakashita, T. Sekiguchi, S.Y. Suzuki, S. Tada, Y. Yamada, K. Yamamoto, and M. Yokoyama. Measurement of the muon beam direction and muon flux for the T2K neutrino experiment. *Progress of Theoretical and Experimental Physics*, 2015(5):053C01, 05 2015.

[17] René Brun, F Bruyant, Federico Carminati, Simone Giani, M Maire, A McPherson, G Patrick, and L Urban. *GEANT: detector description and simulation tool; March 1994.* CERN Program Library. CERN, Geneva, 1993. Long Writeup W5013.

[18] N. Abgrall et al. Report from the NA61/SHINE experiment at the CERN SPS. Technical report, CERN, Geneva, 2010.

[19] C. Ahdida et al. New capabilities of the fluka multi-purpose code. *Frontiers in Physics*, 9, 2022.

[20] Giuseppe Battistoni et al. Overview of the FLUKA code. *Annals Nucl. Energy*, 82:10–18, 2015.

[21] K. Abe et al. T2k neutrino flux prediction. *Physical Review D*, 87(1), January 2013.